UHASSELT
KNOWLEDGE IN ACTION

2022| Faculty of Sciences

Doctoral dissertation submitted to obtain the degree of
Doctor of Sciences: Physics, to be defended by

Jaroslav Hruby

DOCTORAL DISSERTATION

Diamond NV colour centre spin resonance magnetometers: from fundamentals to advanced operation principles

Promoter: Prof. Dr Milos Nesladek | UHasselt

UHASSELT
KNOWLEDGE IN ACTION

www.uhasselt.be
Hasselt University
Martelarenlaan 42 | BE-3500 Hasselt

2022 | Faculty of Sciences

UHASSELT

KNOWLEDGE IN ACTION

Doctoral dissertation submitted to obtain the degree of
Doctor of Sciences: Physics, to be defended by

Jaroslav Hruby

DOCTORAL DISSERTATION

Diamond NV colour centre spin resonance magnetometers: from fundamentals to advanced operation principles

IMO-IMOMEC
UHASSELT imec

Promoter: Prof. Dr Milos Nesladek | UHasselt

D/2022/2451/76


fwo

Acknowledgements

Dedicated to Archi and Balty,
my four-pawed friends.

"Working hard for something we do not care about is called stress.
Working hard for something we love is called passion."
- Simon Sinek,

When you know your WHY, you are better equipped and more confident to choose the path that aligns with what you believe. The result is finding greater fulfillment in the work you do. And while doing so, you meet great companions. Some of them are there the entire time, some of them appear briefly... but all of them leave you enriched.

Following lines, I would like to dedicate to all of those who have been part of my PhD journey and beyond.

First and foremost, hereby I take the chance to thank my promoter prof. dr. Milos Nesladek. When we first met back in 2013, I was considering travelling for Erasmus. Based on our meeting I chose UHasselt. I got involved with a project that ultimately led to the publication in Nature Communications under his supervision. This achievement opened the door to starting my PhD within Quantum Science and Technology research group. I am endlessly grateful for all the opportunities and your support and endorsement across all the years and the projects we were working on together. And I am looking forward for more!

Next, I want to express my gratitude to all my fellow colleagues within Quantum Science and Technology research group (current and the past). Emilie, thanks for always being there and your burning determination and perseverance is inspiring. Michal, thanks for the empowering and creative cooperation from the beginning and continuing... Jeroen, thanks for your inspiring and positive energy and your insights, Pepa thanks for going large part of the journey together already since FBMI, Michael thanks for thinking out of the box! Zdenek, Abhishek, Reza, Souvik, Darya, Alevtina, thanks a lot for the critical thinking and being great colleagues!

Besides, I would like to thank all of my colleagues at imo-imomec. Thank you for being here and creating the supportive and positive environment. Without you imo would not be what it is, and thanks to you working here is fun and joy. I appreciate that your doors are always open so that I can come to you anytime with anything.

Johnny, thank you for always finding the solution, listening, and together with Christel and Hilde, thank you for keeping us all safe and maintaining things in order. If you weren't there the imo would be consumed by entropy. Jan, Lieven, and Erik, thank you for your guidance early on, and for everything I have learned from you. Jeroen, Ellen, Lieve thank you for your help in slaying some bureaucratical dragons here and there… on a regular basis…

Engineering is not an occupation, it's the lifestyle! Thanks to all the fellow engineers Ronald, Thijs, Gilles, Seppe, Phillipe, Michaël, Frederik, Wim… Your advice, sharing components, tools and jokes, Nespresso clubbing, and many other things made possible to progress faster and further, with more energy and laughter.

Huge thanks also to Massimo, my mentor at imec, I can always rely on your support, guidance and resolving all my questions. Thanks to you finding the right processing steps in III-V area was seamless. Nicolo, thank you very much for being very supportive on every level and for interesting talks when we sometimes met during the long hours in the cleanroom.

Inspiration, motivation, support, thinking out of the box, dream it, team up, go for it, do it! Those are the first few words that came to my mind when I was reflecting on what to write here, Jean. Still, these words are not nearly enough to express it fully. It was the first Aurora Expedition that started it all. And all of it has an immense value to me. I am looking forward to next adventures!

Michel, thanks a lot for being there every time I needed mental support or kick forward. All those times when we were enjoying some Falukorv during Aurora hunting season… unforgettable. As well as all the technical help you and Rik did provide me with during all those years means a lot to me! Both of you influenced me in a positive way and I learned a lot from you. Thank you! Also, a big thanX to "the G6 crew" for expanding my points of views during lunch discussions over the years. - Jeroen, Koen, Robin, Ragha, Thessa, Stefanie, Mieke, Dorien...

Johan, thanks for making every mechanical piece beautiful and crafted with care. You are not only "shaping metals", but also share your knowledge and wisdom with people that ask your help. I've learned a lot from you. Thank you and Koen for making all the crazy mechanical gizmos we ever came up with real.

OSCAR. Optical Sensors based on CARbon materials. The elaborate hobby that started back in 2014 when we were freezing in the dark cold nothingness of polar region, hunting down the Aurora Borealis. It was the visit to ESRANGE in Kiruna, to spark the inspiration. Followed by Milos, Jean and me - the founding fathers - sitting at the table warming up with Becherovka. That was the origin.

What was born later manifested as three teams. Teams made up of amazing and inspiring people that made this adventure possible. The team we formed together means to me more than I am able to express in written words. I am very glad that it was you guys, who were there...

OSCAR-BEXUS. This team started it all. Set the baseline. Pushed the limits… Tim the Leader, Mama Ilaria, Steven the Half-faced, Mechanical Rob, Dieter the Key player, and Jelle the Sorcerer's apprentice – Remember when everyone was outside, and we were putting together the SAMv3 aurora catcher to allow everyone see the aurora later on? So many stories, unforgettable experience, and tons of fun balancing the deadlines. All of you mean a lot to me. Stay SUPRA!

OSCAR-QLITE. Lots of emotions, lots of experience, distant sound of a whip. Maybe the technology wasn't there yet, but we did lay foundation together for the next step. Goele, Tom, Dylan. You mean a lot to me and the lessons we learned together determined the course for next step in this journey.

OSCAR-QUBE. Whatever came in our way, we figured out. And that there were quite some things… From the moment we opened up the email saying yes, we were all together. We were designing it together. Building it together. Testing it together. And when it was aboard a roaring rocket leaving the gravity of the Earth, we were standing there together. Boo, Yarne, Dries, Musa, Remy, Jeffrey, Sam, Sofie, Sebastiaan, Siemen A., Siemen V., Jens, Teoman, Zander, Daphne. Without you it would be what it is and what it still can become. And despite the last packet from 53:55:50:52:41 has been sent, remember: Stronger together!

Thank you to all my mentors, friends, and colleagues at ESA, SSC, DLR, and all around the space. All of you had a huge impact on shaping the OSCAR the way it is. Both directly by all the RIDs, comments, and suggestions. And indirectly by teaching me the ways. Thanks for all the students that were influenced for life by projects like REXUS/BEXUS and Orbit Your Thesis! Nigel, Piotr, Koen, Paolo, Alex, Stefan, Armelle, Veronica, Max, Joost, Piero, Dieter, Simon, Thanassis, Marco, Sven… You are amazing and inspiring people. You are the ones influencing the Young European Space sector. Keep up the great work!

I very much appreciate the scientific collaboration with Dima, Arne, and Huijie from Helmholtz Institute, JGU, Mainz. The short time spent within your welcoming group was very fruitful and I enjoyed it a lot.

I acknowledge the Research Fund Flanders (FWO), for giving me the possibility to pursue the scientific career.

Thanks to all the jury members, for spending their valuable time to read my thesis and give valuable and supportive feedback.

Taky bych chtěl poděkovat své rodině za neutuchající podporu. Mamince Valerie, Tatínkovi Jardovi, ale taky mé sestřičce Valince. Dále pak dědečkovi Jaroslavovi, i Lubomírovi. Babičkám Lidušce a Káje. Strejdovi Lubošovi a Tetě Ivance. Vaše podpora pro mě moc znamená a vždy znamenala. A i přesto, že nás dělí značná vzdálenost jsme si stále blízko. Mám vás moc rád!

Ninka, Fresh, Máslo. Three persons without whom my life would look diametrically different. You are always there; you played a role in many of key events. Supportive and reliable. Advisors and sanity checkers. I am endlessly grateful to have met you and walking the journey together. You mean a lot to me.

Although I tried to capture the most of it, the words above are only a fraction of what is really there. Thank you.

Gratefully yours,
Jarda

Hasselt, September 2022

Summary

The first part of the thesis - chapter 1 presents to the reader an introduction into the rich application potential of NV centres and contextualize their benefits. The chapter 1 also summarizes the framework of the thesis, and it spells out the specific aims of the thesis.

Chapter 2 provides a comprehensive description of the NV centre energy structure, as well as the principles of detection of magnetic resonance in diamond, utilizing both optical and photoelectric readout methods. The background knowledge, presented in Chapter 2, gives insights into more advanced approaches such as Continuous Wave (CW) vector magnetic field measurements and pulsed quantum protocols. Furthermore, it summarizes the magnetic field sensitivities of above-mentioned methods. Chapter 2 also briefly covers the material aspects of diamond and the NV centre engineering and explains lithography techniques needed for fabrication of diamond devices including readout electrodes and microwave antennas.

Chapter 3 covers the experimental setup construction used for the ODMR and PDMR measurements. Also, the diamond device fabrication, entailing lithography patterning steps on diamond is described here. It provides a summary of the samples used within this work, as well as the methodology of lithography processes and device fabrication by using both optical lithography and e-beam lithography. Finally, it covers the laboratory measurement setups, their layout and key components, as well as a short description of the software and system automation.

Next chapters ranging from chapter 4 up to chapter 7 are peer reviewed papers to which the author significantly contributed as main author or co-author.

Chapter 4 covers the MW triggering detection method that has been developed and that is utilizing the lock-in readout. This methodology was developed within this thesis and was successfully patented [29] and published [3]. The benefit of this method for PDMR is an extraction of the effective portion of the NV electron spin signal, affected by the microwave field magnetic resonance driving, and which has a positive effect on the SNR of the signal.

Chapter 5 covers the PDMR magnetic field detection sensitivity optimization and improvements by utilizing the yellow-green excitation and readout laser. Chapter 6 expands the PDMR application potential by exploiting the possibility of a microwave free readout method based on Ground State Level AntiCrossing (GSLAC) [30]. Chapter 7 covers the single pixel diamond magnetometer device developed within the student project OSCAR-QUBE, for the ISS onboard mission.

And finally, Chapter 8 is the conclusion of the work done within this thesis and its future outlooks.

Samenvatting

Het eerste deel van het proefschrift - hoofdstuk 1 - geeft de lezer een inleiding in het rijke toepassingspotentieel van NV-centra en contextualiseert hun voordelen. Hoofdstuk 1 vat ook het kader van het proefschrift samen en beschrijft de specifieke doelstellingen van het proefschrift.

Hoofdstuk 2 geeft een uitgebreide beschrijving van de energiestructuur van NV-centra, alsmede de beginselen van de detectie van magnetische resonantie in diamant, waarbij gebruik wordt gemaakt van zowel optische als foto-elektrische uitleesmethoden. De achtergrondkennis, gepresenteerd in hoofdstuk 2, geeft inzicht in meer geavanceerde benaderingen zoals Continuous Wave (CW) vector magnetische veldmetingen en gepulseerde kwantumprotocollen. Voorts wordt een overzicht gegeven van de magneetveldgevoeligheid van bovengenoemde methoden. Hoofdstuk 2 behandelt ook kort de materiële aspecten van diamant en de NV-centrumtechniek en legt de lithografietechnieken uit die nodig zijn voor de fabricage van diamantapparaten, waaronder uitleeselektroden en microgolfantennes.

Hoofdstuk 3 behandelt de experimentele opbouw van de ODMR- en PDMR-metingen. Ook de fabricage van diamantapparaten, waarbij lithografische patronen op diamant worden gemaakt, wordt hier beschreven. Het geeft een overzicht van de in dit werk gebruikte monsters, evenals de methodologie van de lithografieprocessen en de fabricage van het apparaat met behulp van zowel optische lithografie als e-beam-lithografie. Ten slotte worden de meetopstellingen in het laboratorium, de lay-out en de belangrijkste onderdelen ervan behandeld, evenals een korte beschrijving van de software en de systeemautomatisering.

De volgende hoofdstukken, van hoofdstuk 4 tot en met hoofdstuk 7, zijn peer reviewed artikelen waaraan de auteur als hoofdauteur of co-auteur een belangrijke bijdrage heeft geleverd. Hoofdstuk 4 behandelt de ontwikkelde MW-triggerdetectiemethode die gebruik maakt van de lock-in uitlezing. Deze methode is binnen dit proefschrift ontwikkeld en met succes gepatenteerd [29] en gepubliceerd [3]. Het voordeel van deze methode voor PDMR is een extractie van het effectieve deel van het NV elektronenspinsignaal, dat wordt beïnvloed door de magnetische resonantiesturing met microgolfveld, en dat een positief effect heeft op de SNR van het signaal.

Hoofdstuk 5 behandelt de optimalisering van de gevoeligheid van de PDMR-magneetvelddetectie en verbeteringen door gebruik te maken van de geelgroene excitatie- en uitleeslaser. Hoofdstuk 6 breidt het toepassingspotentieel van PDMR uit door gebruik te maken van de mogelijkheid van een microgolfvrije uitleesmethode op basis van Ground State Level AntiCrossing (GSLAC) [30]. Hoofdstuk 7 behandelt de diamantmagnetometer met één pixel, ontwikkeld binnen het studentenproject OSCAR-QUBE, voor de ISS-boordmissie.

Hoofdstuk 8 tenslotte is de conclusie van het werk dat binnen dit proefschrift is verricht en de toekomstperspectieven.

Table of Contents

ACKNOWLEDGEMENTS ..... **I**

SUMMARY ..... **V**

SAMENVATTING ..... **VII**

TABLE OF CONTENTS ..... **IX**

LIST OF SCIENTIFIC CONTRIBUTIONS ..... **XI**

PATENTS ..... **XI**

PEER-REVIEWED PAPERS ..... **XI**

CONTRIBUTIONS TO CONFERENCES ..... **XII**

AWARDS AND COMPETITIONS ..... **XIII**

LIST OF ACRONYMS ..... **XV**

1. CHAPTER 1 - PREFACE **1**

1.1. AIMS OF THE THESIS 2
1.2. APPLICATIONS OF NV CENTRES BASED MAGNETOMETRY 3
1.3. SPACE BENEFITS IN USING NV MAGNETOMETRY 5

2. CHAPTER 2 - CONCEPT AND METHODOLOGY **9**

2.1. NITROGEN-VACANCY CENTRES 9
2.2. OPTICAL DETECTION OF MAGNETIC RESONANCE (ODMR) 11
2.3. PHOTOELECTRIC DETECTION OF MAGNETIC RESONANCE (PDMR) 13
2.4. MAGNETIC FIELD VECTOR MEASUREMENTS 15
2.5. PULSED QUANTUM MEASUREMENTS 16
2.5.1. Ramsey sequence *17*
2.5.2. Hahn echo sequence *19*
2.6. SENSITIVITY OF CONTINUOUS WAVE MAGNETIC FIELD MEASUREMENTS 20
2.7. MICROWAVE-FREE NV MAGNETOMETRY WITH GROUND STATE LEVEL ANTI-CROSSING (GSLAC) 21
2.8. DIAMOND AND NV CENTRES FABRICATION 22
2.8.1. NV centres fabrication *22*
2.9. LITHOGRAPHY PROCESSING 23
2.9.1. Photoresist *23*
2.9.2. Spin coating *24*
2.9.3. Soft baking *24*
2.9.4. Image-reversal bake *25*
2.9.5. Exposure *25*
2.9.1. Development *25*
2.9.2. Metal deposition *26*
2.9.3. Lift-off *27*

3. CHAPTER 3- EXPERIMENTAL SETUP AND DEVICE FABRICATION 29

3.1. CHALLENGES OF LITHOGRAPHY PROCESS ON SMALL SAMPLES 29
3.2. SAMPLE HOLDER FABRICATION BY SILICON WAFER ETCHING 30
3.3. AUTOMATED PROCESS OF 3D PRINTED SAMPLE HOLDER FABRICATION 31
3.4. OPTICAL LITHOGRAPHY PROCESS 34
3.4.1. Optical mask design 34
3.4.2. Optical lithography methodology 35
3.4.3. Optical lithography results 36
3.5. E-BEAM LITHOGRAPHY PROCESS 37
3.5.1. E-beam mask design 37
3.5.2. E-beam methodology 38
3.5.3. E-beam results 38
3.6. LABORATORY MEASUREMENT AND SETUP DESCRIPTION 39
3.6.1. General setup layout 40
3.6.2. Setup software 42
3.6.3. Setup 1 (Spectroscopy setup) 45
3.7. REFERENCES FOR CHAPTERS 1-3 49

4. CHAPTER 4 - PULSED PHOTOELECTRIC COHERENT MANIPULATION AND DETECTION OF N-V CENTER SPINS IN DIAMOND 55

5. CHAPTER 5 - MAGNETIC FIELD SENSITIVITY OF THE PHOTOELECTRICALLY READ NITROGEN-VACANCY CENTRES IN DIAMOND 69

6. CHAPTER 6 - ELECTRICAL READOUT MICROWAVE-FREE SENSING WITH DIAMOND 81

7. CHAPTER 7 - OSCAR-QUBE: INTEGRATED DIAMOND-BASED QUANTUM MAGNETIC FIELD SENSOR FOR SPACE APPLICATIONS 95

8. CHAPTER 8 – CONCLUSION AND OUTLOOK 119

8.1. CONCLUSION 119
8.2. OUTLOOK 121

9. APPENDIX 123

9.1. SETUP COMPONENT DESCRIPTION 123
9.1.1. Setup 2 (Magnetometry setup) 123
9.1.2. Setup 3 (NMR setup) 128
9.1.3. Setup 4 (OSCAR-QUBE test bench setup) 134

List of scientific contributions

Below are listed scientific contributions, ordered from least to most recent.

Patents

(1) **Hruby, J.**, Bourgeois, E., Nesladek, M., De Ceuninck, W., 'Magnetometer Sensor With Negatively Charged Nitrogen-Vacancy Centers in Diamond', Patent US20170328965A1, Nov. 16, 2017

Peer-reviewed papers

(1) E. Bourgeois, A. Jarmola, P. Siyushev, M. Gulka, **J. Hruby**, F. Jelezko, D. Budker, and M. Nesladek, 'Photoelectric detection of electron spin resonance of nitrogen-vacancy centres in diamond', Nature Communications, vol. 6, no. 1, p. 8577, Oct. 2015, doi: 10.1038/ncomms9577.

(2) E. Bourgeois, E. Londero, K. Buczak, **J. Hruby**, M. Gulka, Y. Balasubramaniam, G. Wachter, J. Stursa, K. Dobes, F. Aumayr, M. Trupke, A. Gali, and M. Nesladek, 'Enhanced photoelectric detection of NV magnetic resonances in diamond under dual-beam excitation', Phys. Rev. B, vol. 95, no. 4, p. 041402, Jan. 2017, doi: 10.1103/PhysRevB.95.041402.

(3) M. Gulka, E. Bourgeois, **J. Hruby**, P. Siyushev, G. Wachter, F. Aumayr, P. R. Hemmer, A. Gali, F. Jelezko, M. Trupke, and M. Nesladek, 'Pulsed Photoelectric Coherent Manipulation and Detection of NV Center Spins in Diamond', Phys. Rev. Applied, vol. 7, no. 4, p. 044032, Apr. 2017, doi: 10.1103/PhysRevApplied.7.044032.

(4) D. Schreurs, S. Nagels, I. Cardinaletti, T. Vangerven, R. Cornelissen, J. Vodnik, **J. Hruby**, W. Deferme, and J. V. Manca, 'Methodology of the first combined in-flight and ex situ stability assessment of organic-based solar cells for space applications', Journal of Materials Research, vol. 33, no. 13, pp. 1841–1852, Jul. 2018, doi: 10.1557/jmr.2018.156.

(5) I. Cardinaletti, T. Vangerven, S. Nagels, R. Cornelissen, D. Schreurs, **J. Hruby**, J. Vodnik, D. Devisscher, J. Kesters, J. D'Haen, A. Franquet, V. Spampinato, T. Conard, W. Maes, W. Deferme, and J. V. Manca, 'Organic and perovskite solar cells for space applications', Solar Energy Materials and Solar Cells, vol. 182, pp. 121–127, Aug. 2018, doi: 10.1016/j.solmat.2018.03.024.

(6) P. Siyushev, M. Nesladek, E. Bourgeois, M. Gulka, **J. Hruby**, T. Yamamoto, M. Trupke, T. Teraji, J. Isoya, and F. Jelezko, 'Photoelectrical imaging and coherent spin-state readout of single nitrogen-vacancy centers in diamond', Science, vol. 363, no. 6428, pp. 728–731, Feb. 2019, doi: 10.1126/science.aav2789.

(7) E. Bourgeois, M. Gulka, D. Wirtitsch, P. Siyushev, H. Zheng, **J. Hruby**, A. Wickenbrock, D. Budker, A. Gali, M. Trupke, F. Jelezko, and M. Nesladek, 'Chapter Three - Fundaments of photoelectric readout of spin states in diamond', in Semiconductors and Semimetals, vol. 104, C. E. Nebel, I. Aharonovich, N. Mizuochi, and M. Hatano, Eds. Elsevier, 2021, pp. 105–147. doi: 10.1016/bs.semsem.2020.08.001.

(8) M. Gulka, D. Wirtitsch, V. Ivády, J. Vodnik, **J. Hruby**, G. Magchiels, E. Bourgeois, A. Gali, M. Trupke, and M. Nesladek, 'Room-temperature control and electrical readout of individual nitrogen-vacancy nuclear spins', Nature Communications, vol. 12, no. 1, p. 4421, Jul. 2021, doi: 10.1038/s41467-021-24494-x.

(9) M. Krečmarová, M. Gulka, T. Vandenryt, **J. Hrubý**, L. Fekete, P. Hubík, A. Taylor, V. Mortet, R. Thoelen, E. Bourgeois, and M. Nesládek, 'A Label-Free Diamond Microfluidic DNA Sensor Based on Active Nitrogen-Vacancy Center Charge State Control', ACS Appl. Mater. Interfaces, vol. 13, no. 16, pp. 18500–18510, Apr. 2021, doi: 10.1021/acsami.1c01118.

(10) E. Bourgeois, J. Soucek, **J. Hruby**, M. Gulka, and M. Nesladek, 'Photoelectric detection of nitrogen-vacancy centres magnetic resonances in diamond: role of charge exchanges with other opto-electrically active defects', Advanced Quantum Technologies, p. 2100153, Jan. 2022, doi: 10.1002/qute.202100153.

(11) **J. Hruby**, M. Gulka, M. Mongillo, I. P. Radu, E. Bourgeois, and M. Nesladek, 'Magnetic field sensitivity of the photoelectrically read nitrogen-vacancy centers in diamond', Appl. Phys. Lett., vol. 120, no. 16, p. 162402, Apr. 2022, doi: 10.1063/5.0079667

Accepted

(1) H. Zheng*, **J. Hruby***, E. Bourgeois, J. Soucek, P. Siyushev, F. Jelezko, A. Wickenbrock, M. Nesladek, and D. Budker, 'Electrical readout microwave-free sensing with diamond', arXiv:2201.01801 [physics, physics:quant-ph], January 2022, http://arxiv.org/abs/2201.01801 [Accepted]

Contributions to conferences

(1) **J. Hruby**, E. Bourgeois, M. Nesladek, Sensitive magnetometers based on nitrogen-vacancy centers in diamond, EE.6.3, EMRS Spring meeting 2016, Lille, France, Oral presentation

(2) **J. Hruby**, J. Vodnik, T. Vangerven, I. Cardinaleti, S. Nagels, R. Cornelissen, D. Schreurs, M. De Roeve, J. V. Manca, and M. Nesladek, 'Development of ultra-sensitive portable 3d magnetometer based on diamond NV-centers for OSCAR (BEXUS 23)', 2017, 23rd ESA Symposium on European Rocket and Balloon Programmes and Related Research, Visby, Sweden, [A-143]

(3) **J. Hruby**, G. Magchiels, T. Mladenov, D. Gybels, K. Winter, J. Vodnik, J. Prooth, M. Gulka, E. Bourgeois, M. Nesladek, 'Engineering platform for electric readout of NV spin center in diamond for magnetic field detection', 2018, 69th International Astronautical Congress, Bremen, Germany. IAC-18,28,8,3,x47157

(4) **J. Hruby**, G. Magchiels, T. Mladenov, D. Gybels, K. Winter, J. Vodnik, M. Nesladek, 'Diamond as a quantum sensor for space exploration', Put Your Thesis ON session, 2018, 12th ESA Workshop on Avionics, Data, Control and Software Systems (ADCSS2018), ESA/ESTEC

(5) **J. Hruby**, S. Achten, M. Aydogan, S. Bammens, Y. Beerden, B. Carmans, J. Gorissen, D. Hendrikx, T. Koseoglu, J. Mannaerts, R. Vandebosch, S. Vandervoort, S. Vanspauwen, and M. Nesladek, 'OSCAR-QUBE: Integrated Diamond-based Quantum Magnetic Field Sensor for Space Applications', 2021, 72nd International Astronautical Congress, Dubai, UAE, IAC-21,E2,3-GTS.4,13,x66880*

Awards and competitions

(1) OSCAR-BEXUS project – ESA awarded student project in framework of 'Rocket/Balloon EXperiment for University Students' (REXUS/BEXUS) programme for university students granting the opportunity to develop experiment to be tested onboard the stratospheric balloon flight (2015/2016)

(2) OSCAR-QLITE project – ESA awarded student project in framework of 'Rocket/Balloon EXperiment for University Students' (REXUS/BEXUS) programme for university students granting the opportunity to develop experiment to be tested onboard the stratospheric balloon flight (2018/2019)

(3) OSCAR-QUBE project – ESA awarded student project in framework of 'Orbit Your Thesis' (OYT) programme for university students project granting the opportunity to develop experiment to be tested onboard the International Space Station (2020-2022)

(4) Hans von Muldau Best Team Award (72nd International Astronautical Congress, Dubai, 2021) for paper entitled 'OSCAR-QUBE: Integrated Diamond Based Quantum Magnetic Field Sensor for Space Applications'*

List of acronyms

1U one unit

2D two dimensional

3D three dimensional

AC alternating current

ADC analogue-digital converter

ADCSS Avionics, Data, Control and Software Systems

AFM atomic force microscopy

AOM acousto-optic modulator

AOS acquisition of signal

APD avalanche photodiode

AWG arbitrary waveform generator

BEXUS Balloon Experiment for University Students

CB conduction band

CPMG Carr-Purcell-Meiboom-Gill sequence

CVD chemical vapour deposition

CW continuous wave

DC direct current

DNA deoxyribonucleic acid

EEG electroencephalography

ELGRA European Low Gravity Research Association

EMC electromagnetic compatibility

EMI electromagnetic interference

EPM European Physiology Module

ES excited state

ESA European Space Agency

ESEC European Space Security and Education Centre

ESR electron spin resonance

ESTEC European Space Research and Technology Centre

FLIR forward looking infra-red

FPGA field programmable gate arrays

FWHM full-width half-maximum

GMR giant magnetoresistance

GNSS global navigation satellite system

GPS global positioning system

GS ground state

GSLAC ground state level anticrossing

GUI graphical user interface

HPHT high-pressure high-temperature

IC integrated circuit

ICMCC ICE Cubes mission control centre

ID identification number

ISC intersystem crossing

ISS International Space Station

IV current-voltage

LEO low Earth orbit

LIA lock-in amplifier

LOS loss of signal

MCS mission control software

MCU microcontroller unit

MEG magnetoencephalography

MEMS microelectromechanical systems

MW microwave

NMR nuclear magnetic resonance

NV nitrogen vacancy

ODMR optically detected magnetic resonance

OSCAR optical sensors based on carbon materials

OYT orbit your thesis

PC photocurrent

PCB printed circuit board

PDMR photocurrent detected magnetic resonance

PFM protoflight model

PL photoluminescence

PLL phase-locked loop

POS proton Overhauser sensor

PSD power spectrum density

REXUS rocket experiment for university students

RF radio frequency

RPM rotations per minute

SD secure digital

SNR signal-to-noise-ratio

SQUID superconducting quantum interference device

TC telecommand

TM telemetry

TMAH tetramethylammonium hydroxide

TTL transistor-transistor logic

UDP user datagram protocol

UHB user homebase

UV ultraviolet

UX user experience

VPN virtual private network

ZFS zero field splitting

ZPL zero phonon line

1. Chapter 1 - Preface

Quantum technology research is a novel and fast-growing field, aiming at producing new and improved applications over time. In recent years quantum sensing has emerged, exploiting the strong reactivity of quantum systems to external disturbances [1]. The quantum system of our interest is a nitrogen vacancy (NV) diamond-based magnetometer. Its working principle relies on the NV centre, an optically active paramagnetic point-defect, known as a solid-state qubit, characterized by a long spin coherence time and well-defined optical transitions. Individual centres can be employed to reach nanoscale resolution, while NV ensembles can be used as non-invasive magnetic probes with theoretical fT/√Hz. [2] NV centre shows a range of additional highly desirable sensing characteristics: wide dynamic range (fT – T) of detection, wide bandwidth (DC – MHz), response time of around 100 ns to AC magnetic fields, robustness, radiation hardness and thermal stability.

The use of a photoelectric readout method, developed by our research group in 2015, called Photoelectric Detection of Magnetic Resonance [3] (PDMR), has been a key factor in improving the signal collection efficiency and brought the prospects of on-chip integration. The NV centres are located along four different orientations of diamond lattice which can be utilized for vector magnetometry. The optimisation of the detection performance using this technique is therefore the main content of this thesis.

For sake of demonstration of the practical application of the diamond based magnetometry, the student project OSCAR was initiated, appending on some of the scientific results presented in the thesis. Within this project a prototype of an Optically Detected and Photoelectrically Detected Magnetic Resonances (ODMR and PDMR) based magnetometer was developed as an engineering model to be used on the *International Space Station (ISS)*. The resulting device meets the requirements of space magnetometry and from September 2021 to July 2022 utilizes the large geographical coverage provided by *ISS* and *ICE Cubes facilities* to map the magnetic field of the Earth and fields onboard the station. The ten-month duration experiment, being part of the 'Orbit Your Thesis!' programme of ESA [4] will provide enough time to characterize slowly changing components of the magnetic field. By acquiring information along four different orientations of NV centres, it is possible to distinguish between the different sources contributing to this field on different temporal and spatial scales. In addition to the scientific work presented in the thesis and supported by results of the previous OSCAR projects, the OSCAR-QUBE project allowed for involving a team of interdisciplinary Bc. and MSc. students working together on wider magnetometry problematics and bringing NV magnetometry from the lab towards real-world applications. As an additional value of the concepts developed in the thesis the OSCAR-QUBE project enables participating students to contribute with innovative and creative, yet technically and scientifically sound ideas and solutions to the realisation of engineering magnetometer model and at the same time to increase their knowledge to become the next generation of experts ready to strengthen the European space and quantum research.

1.1. Aims of the thesis

The main objective of this PhD work is to study diamond NV centre spin-state detection principles and to develop and profoundly test diamond-based devices for measurements of magnetic fields. To this end, the thesis is aimed at developing an original method called the Photocurrent Detection of Magnetic Resonance (PDMR). The target result of this PhD work is to demonstrate a single pixel magnetometer chip operating using the PDMR quantum protocols, integrated with peripheral electronics. The thesis thus combines aspects of photonics, optics, advanced material engineering and quantum sensing.

The devices are constructed from diamond crystals by engineering the NV colour centres in them and further equipped with optimized electrical contacts and microwave (MW) antennas. The mechanism for reaching the highest signal/noise ratios and shot-noise limits are studied.

The functionality of the developed prototypes is demonstrated by measuring a calibrated magnetic field applied externally by e.g., Helmholtz coils. As the title of this work suggests, it will address the whole journey from fundamental working principle, towards the development of portable unit for advanced (space) applications.

The thesis achieved specifically the following points:

I. Development of robust and reproducible lithography process on diamond samples
II. Study of the ODMR and PDMR quantum operation protocols, signal-to-noise-ratio and quantum detection limits.
III. Research to optimize the sensing device layout. The optimization consists of the material selection (number of NV centres and their quantum mechanical characteristics), contact design, optimization of external electron detection including specific preamplifiers and lock-in detection and excitation fields optimization (microwave, laser).
IV. Exploration of advanced operation principles of PDMR based magnetometry.
V. Demonstration of single pixel devices and their characteristics under application of an external magnetic field and their utilization for vector magnetometry. The device is aimed at sensing of solar wind and in-situ measurements in Low Earth Orbit (LEO) of International Space Station (ISS).

1.2. Applications of NV centres based magnetometry

The NV-based magnetometry benefits and originates from a combination of a high sensitivity and wide dynamic range magnetic field detection [5], as shown in the Figure 1. Additionally, NV based sensors are also working in wide range of temperature, including room temperature. The sensing element is are single or ensemble of NV centres in crystalline lattice of a diamond, which allows for significant miniaturization of the entire sensor or of at least the sensing head.

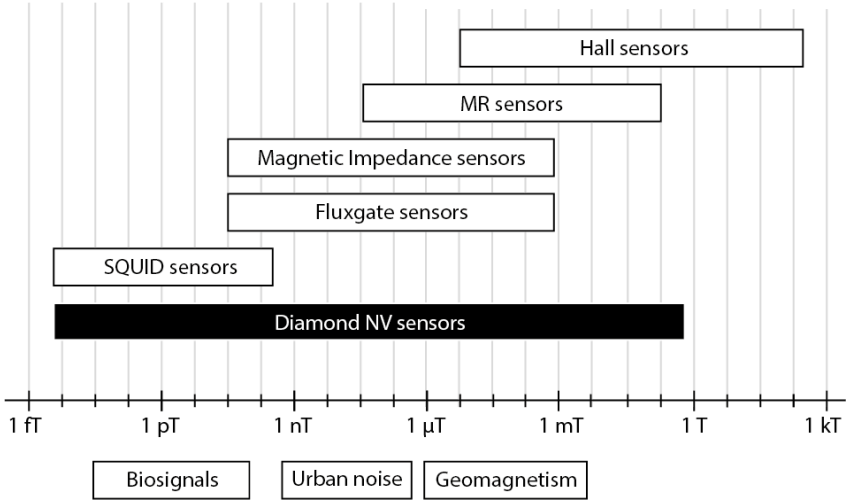

Figure 1 Magnetometer dynamic range comparison (partial selection) [5].

Based upon diamond material's suitability for operating in harsh environments, one of the interesting niche applications of NV diamond sensors is the space environment. The benefits for constructing ultrasensitive quantum magnetometers can be seen in a better characterization of the Earth's magnetic field, and even, for example, future possible usage by Global Navigation Satellite Systems (GNSS). An improved knowledge about the quantum sensing field might aid in creating future GNSS systems with a higher positional accuracy. This would be also an advantage for the navigation of cars, boats, and airplanes. The aviation industry could also benefit from the fast characterization of changes in the magnetic field, enabled by the fast response time of NV magnetometry. A quick determination of the weak Earth's surrounding field could, for example, protect high-flying airplanes from charged particles [6] etc.

Another magnetometry application is to measure the lithospheric magnetic field of the Earth. This originates from magnetized rocks in the Lithosphere. This could aid in the detection of large metal resources in our Earth's crust, which would be useful for mining, and the characterization of geological provinces, and could be used in geological studies. [7] However the properties of NV centres in diamond are highly interesting in multiple scientific and application branches for which magnetometer can be envisioned.

The usage of NV spin centres has much wider perspectives, for example in the nanoscale nuclear magnetic resonance (NMR) sensing. It has been, for example, used to detect protons in an organic sample external to diamond [8] and in other sensing situations [1], [9]. Using a spin echo, the NV centre is able to sense sub-nanotesla field fluctuations from the protons, enabling both time-domain and spectroscopic NMR measurements on the nanometre scale [10], [11] which is a longstanding challenge. Although many technical issues remain, the potential of three-dimensional nanoscale imaging with room-temperature operation and the elemental selectivity of the NV-based nano NMR could become an important complement to current state-of-the-art nanoscale imaging techniques such as cryo-electron tomography and magnetic resonance force microscopy [12]–[14]. Drug analysis by pharmaceutical researchers and molecular analysis, in general, might also benefit strongly from this technique.

As diamond is biocompatible and presents a low toxicity, nano-diamonds containing NV centres can also be inserted into living objects such as living cells or whole organisms. The NV centre shows an excellent photostability and the surface of nano-diamonds can also be functionalized so that they can attach to specific sites in the cell, which enables a local monitoring of biological activity, which is of a great interest for cellular biology [5], [15], [16]. Also, the medical diagnostics can benefit from NV magnetometry. A study investigating the potential of a new generation magnetometers for magnetoencephalography (MEG) has been performed [17]; the use of NV centres can lead to an increase of the dynamical range of detection and the spatial resolution and resolve problems with the external magnetic field shielding. This is possible because of the small size and room-temperature operation of NV diamond-based sensors, which might allow to place sensors directly on the scalp surface. If the noise floor of the NV sensor could reach the one of conventionally used SQUID (Superconducting QUantum Interference Device), this will be highly beneficial for small integrated devices operating at room temperature. This way, one of the fundamental limitations of MEG is overcome, i.e. the noise induced by the pickup coils that need to be cryogenically cooled [18]. Hence the method opens up possibilities to brain analysis in outside-the-lab environment.

NV centres can also be employed in imaging of spin textures in ferromagnetic structures, such as magnetic read/ write heads in magnetic hard drives [19]. This could be done by fabricating a NV centre in scanning probe tips, such as a diamond AFM tip and providing a spatial resolution of ~ 20 nm, while retaining also the non-invasive and quantitative sensing. In this way, the calibration and characterization of the magnetic head performances, which resolution is highly challenging to reach for other techniques, could benefit from NV magnetometry. [5] The same can be expected for defectoscopy in general. Every conductive material can produce a magnetic field when current is passed through it. NV magnetometry could be used to precisely characterize this, in general, ultra-low magnetic and electric fields. An example here would be the system certification, technical inspection etc. Also, interesting applications could be monitoring of pipelines [20]. Pipelines are essential transportation resources for an efficient functioning of modern society. However, often, their aggressive environment makes such measurements complex. The needs for modernization of existing pipelines and building of new pipelines pose several problems to be solved.

Recently, much attention has been paid to find effective non-contact method solutions of these problems. The magnetometry technique is one of such methods. At the moment the high-precision absolute quantum Overhauser "POS" (proton Overhauser sensor) magnetometers are used in the oil-and-gas fields. There is a potential to perform such measurements using NV magnetometers, as they share the characteristic of non-invasiveness. [21], [22]

Magnetometer technologies such as fluxgate, proton-precession, and optically pumped magnetometers have proved their viability with the many space missions they have flown in. However, these space missions have also shown the limitations of these technologies, for instance fluxgate magnetometers have shown to be prone to drifting scale factors and voltage offsets, requiring periodic recalibration [23], [24]. On the other hand, proton-precession magnetometers and optically-pumped magnetometers have shown to exhibit excellent sensitivity (e.g., 10–50 pT RMS), absolute accuracy (0.1–1.0 nT), and a dynamic range (1–100 μT), but also require high power sources (>10 W), take in large volumes (>100 cm3) and have a considerable mass (>1 kg). [23], [24]

Consequently, these instruments are no longer suitable to be used in many emerging aerospace applications, particularly in the popular smaller platforms and probes such as CubeSats and NanoSats. Magnetometer size, weight and power must be reduced, while preserving or even enhancing performance to increase the usability in the aforementioned small platforms. As many of the magnetometers summed up so far are close to their applicability limits, new types of magnetometers will take their place. Particularly, NV-diamond based quantum magnetometers are promising candidates [23].

Apart from sensing applications, NV centres have risen interests for application in quantum computing [8]. NV centres are one of the few quantum systems which can operate at room temperature, which could one day be the key to the commercialization of quantum computing. [1]

1.3. Space benefits in using NV magnetometry

As mentioned in the previous section, since 1990s the nitrogen-vacancy centre in diamond are gaining interest as a platform for quantum sensing and quantum computing experiments. [25] Our interest in the quantum sensing application is to build a diamond-based magnetometer. Its working principle relies on the NV centre, a colour centre occurring in diamond which can be employed as a non-invasive magnetic probe with high sensitivity [2]. In the previous section, it was also mentioned that navigation techniques could benefit from an increased accuracy in the Earth's magnetic field map. The same is true for the navigation of satellites. Employing NV based magnetometers in the space industry could lead to various benefits discussed briefly here. The possibility of filtering out spurious magnetic fields in space vehicles based upon the NV centres wide dynamic range, their vector characteristics, the operation speed, and its combination with pulsed protocols could potentially enable a more precise magnetic field measurement from inside a spacecraft and thus eliminate the need for long booms. The robust diamond material is able to withstand harsh space environments and the NV centres, as the sensing element, are functional

in a wide temperature range. The wide linear dynamic range (0.9 fT – 1 T) [2] makes it possible to measure magnetic field contributions of various amplitudes. The fast response time of the sensor to changes in the magnetic field is based on the possible high frequency Rabi oscillations and spin polarization cycle lengths (~200 ns for the NV centre) [5] and renders measuring fast fluctuating signals, whereas the long duration measurement provides averaging of fluctuating fields. It is thus possible to measure both on long and short spatial and temporal scales, at the same time. In addition, NV magnetometry is inherently vectoral, compared to currently used three-axis fluxgate magnetometers. For these sensors, the 3D accuracy depends on the orthogonality of the three scalar magnetometers. The sensors are typically mounted on a boom outside of the spacecraft, which causes the orthogonality to change or drift in time because of the harsh space environment. NV magnetometers on the other hand are based on diamond, in which an over complete basis of NV centre orientations is naturally present.

Advances in NV magnetometer construction, presented in this work, can lead towards both a decrease in mass and improvements of sensitivity of portable, fully integrated devices. Those are compelling properties which have been proved hard to reach at the same time in a single small size instrument. This combination is what makes the sensor so interesting for space magnetometry, which requires state-of-the-art equipment to withstand the difficult environment, yet deliver scientifically valuable information. This PhD study is aimed at unlocking the potential of NV spin state detection using PDMR to become the new standard for space magnetometry. During the Orbit Your Thesis! programme, we use the NV magnetic sensing technique, not only to map the magnetic field of the Earth, yet also to distinguish between its various sources, both internal and external. This can render separating the spatial and temporal scales of the different magnetic field contributions. As a specific contribution to this field, space weather will be monitored by our sensors onboard the ISS. This study could help in understanding of minute magnetic field sources and could aid in future for mitigating their negative effects on, for example, energy grid or communication networks [26].

The first space-located magnetic field research was already performed in 1958 by the Russian Sputnik 3 satellite. This is an example of a Low Earth Orbit (LEO) satellite [24] launched already more than 60 years ago. It featured a three-axis fluxgate magnetometer with the aim of performing vector magnetic field measurements. This spacecraft was not fully spin-stabilized, since there were no stabilization systems, and it did not have a proper attitude reference. This made the first vector measurements of the earth's magnetic field rather unusable, and the full fluxgate sensor potential could not be fully utilized. The instrument measurement range was 15 – 60 μT with design resolution between 7-30 nT, however it was suffering from various technical issues, such as voltage source causing signal oscillations up to 50-100 mV (whereas instrument sensitivity was 10 μV/nT) [24]–[26]. Since then, there has been a major progress in this subject. However, since the reliability of the fluxgate vector measurements depends on the orthogonality of the three scalar magnetometers, NV magnetometers (which are inherently vectoral and can withstand rough environments easily) have an advantage compared to fluxgate magnetometers in the harsh space environment adding a benefit of miniaturization.

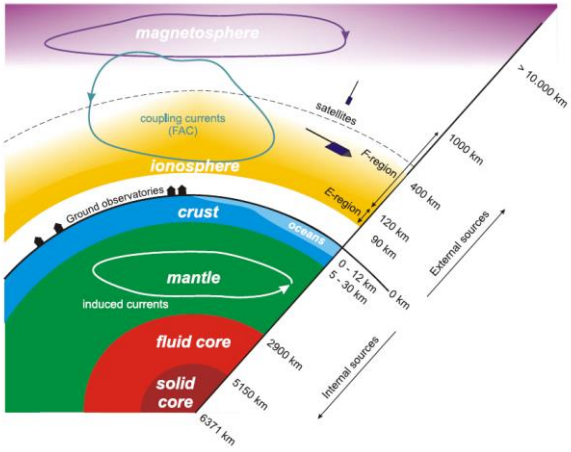

Figure 2 Various sources contributing to the near-Earth magnetic field [27]

To summarize, space magnetometry is a very highly demanding branch of science. It requires state-of-the-art equipment that pushes the boundaries by considering requirements imposed by many, sometimes conflicting, factors such as a wide dynamic range, sampling rate, radiation hardness, thermal stability, and most importantly a high sensitivity. These requirements stem from the fact that measuring the magnetic field in near-Earth environment space is a difficult task. The field itself is a superposition of fields produced by many different sources, overlapping temporally and spatially. These contributing sources of magnetic field are illustrated in Figure 2 and it can be seen that the total magnetic field is then composed of a few distinct magnetic field components characterized on smaller spatial and temporal scales, for example by the field induced by magnetized rocks in the lithosphere. Another contributor is the weak magnetic field created by oceanic tides. However, there is also a large group of other contributions to the net magnetic field starting 100 km above Earth's surface, such as fields induced by electrical currents in the ionosphere and magnetosphere. Moreover, satellites are moving objects. This results in space-time-aliasing that needs to be disentangled, reducing the sensitivity of the measurements [27]. During years of space exploration, there has been a constant improvement in quality of the magnetic measurements in space. [28] NV diamond-based magnetometry has potential to satisfy the previously named criteria as it is characterized by a low noise level [9], [27], [29]. The aim of this work is to prove that this sensor can also potentially acquire data about the magnetic field on small timescales and for longer periods of time without drift or need for recalibration.

2. Chapter 2 - Concept and methodology

2.1. Nitrogen-vacancy centres

Magnetometry principles described within this work are based on nitrogen-vacancy (NV) centres inside the diamond. Diamond crystal lattice is formed by carbon-carbon atomic bonds in a face-centred cubic (tetrahedral) structure. The forming of NV centres in diamond can occur either during its growth (both natural or artificial) or after high energy particle irradiation of nitrogen-containing diamond, when two carbon atoms are replaced by a nitrogen atom and an adjacent vacancy. Nitrogen can be also implanted to the diamond lattice. The density of NV centres can be tuned to match desired sample properties. It can vary from single NV centres to NV centres ensembles with a density of up to approximately 50 ppm. The high NV density gives purple to dark reddish colour to otherwise colourless diamond (see Figure 3 where different defects can give the sample different colour properties in ambient lighting).

The NV centres in the diamond are randomly aligned along one of the four possible NV directions. However, under specific conditions [9] the diamonds can be grown with a preferential <111> orientation matching one of the NV centres axis. However, a drawback of the preferential orientation obtained by CVD growth is that this material is not optimal for implementation of vector magnetometry.

The NV colour centres act in some way comparably as atoms in a free space with properties like long-lived spin quantum states or well-defined optical transitions. Although they are contained in the solid-state lattice which relates them with diamond solid state properties [30]. NV centre structure is shown in Figure 3.

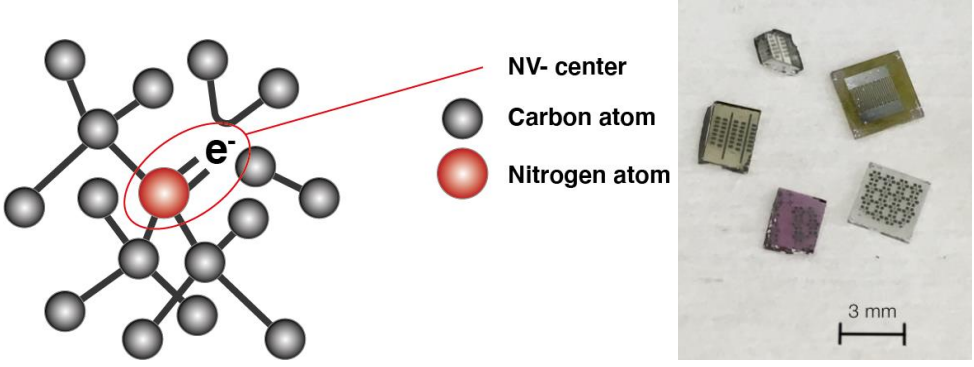

Figure 3 (left) Diamond structure with NV centre [31] (right) Photo of different types of diamond samples containing various density of NV centres, transparent are of very low NV density in which single NVs can be found, purple sample contains ~ 10 ppm of NV centres, and yellow contains substitutional nitrogen

NV centres can be found in different charge states, namely positive, neutral, and negatively charged state. [5] For NV^0 (neutral) charge state, the nitrogen atom electrons couple with the vacancy electrons. Two electrons are given by N and three electrons are given by vacancies. Therefore, the formed centre has neutral charge and is called NV^0 centre. The NV^0 centre can gain an additional electron, forming a NV^- state and responsible for the paramagnetic behaviour.

The additional electron can be supplied by other impurities in the diamond structure i.e., substitutional nitrogen, leading to negative charging of the complex, resulting in NV^- centres. Because of the NV^- centre is responsible for majority of the behaviours described in this work, it will be used without the sign and referred to as NV centre further on. The NV^- centre has six electrons which occupy molecular orbitals where their combined spin is fixed at 0 or ±1. These NV states can occur as a spin singlet and spin triplet states. The different triplet combinations are shown in Figure 4. The triplet ground state and an optically excited triplet state are noted $^3A_2$ and ^3E respectively. A schematic overview of possible spin transitions is further given in Figure 5 and 6. Energy levels in the spin triplet states are shown with the corresponding m_s value.

The energetic splitting between the |0> and the |±1> states is called the zero-field splitting (ZFS), fixed at approximately 2.87 GHz at room temperature for the ground state (GS) and approximately 1.42 GHz for the excited state (ES). [32] When no external magnetic field is applied, the |+1> and |-1> energy levels are equal.

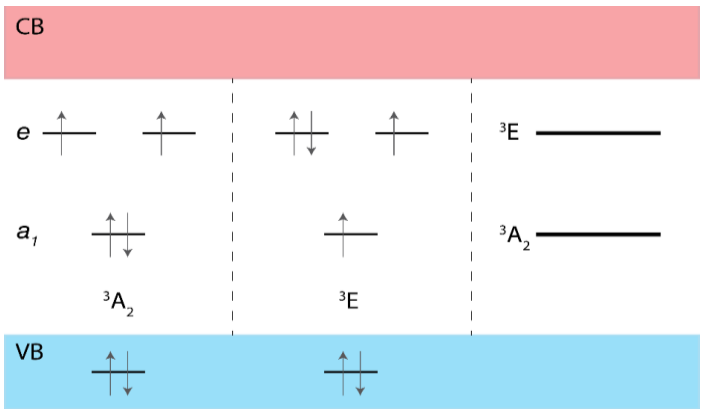

Figure 4 Molecular orbitals of the spin triplet states. Schematic diagram of the defect states in the gap and their occupation in the ground ($^3A_2$) and excited (^3E) states. [33]

The photoluminescence (PL) of the NV centre is substantially higher when the |0> state is populated, which enables the optical spin state detection called the Optical Detection of Magnetic Resonance (ODMR) which can be used for magnetic field sensing and will be further discussed in the next section.

2.2. Optical detection of magnetic resonance (ODMR)

The ODMR detection method relies on the principles already discussed in section 2.1 and occurs when the resonance frequency of 2.87 GHz is applied, promoting spin flips from |0> to |±1> of the ground spin triplet state. In absence of the magnetic field, one can infer the value of zero-field-splitting with this method. In the presence of an external magnetic field, the |±1> level splits by the Zeeman splitting. In presence of a non-zero external magnetic field, the Zeeman effect has to be taken into account in the spin dynamics. This effect lifts the m_s-degeneracy of the |±1> energy sublevels and splits them into m_s = +1 and m_s = -1 sublevels. When the sublevels are split, the applied microwave field can cause two transitions, one from |0> to |-1> and one from |0> to |+1>. These two transitions will manifest themselves at two different resonance frequencies in the measured ODMR spectrum, symmetrically located on either side of the original ZFS. The abovementioned transition between energy levels can be seen in Figure 5.

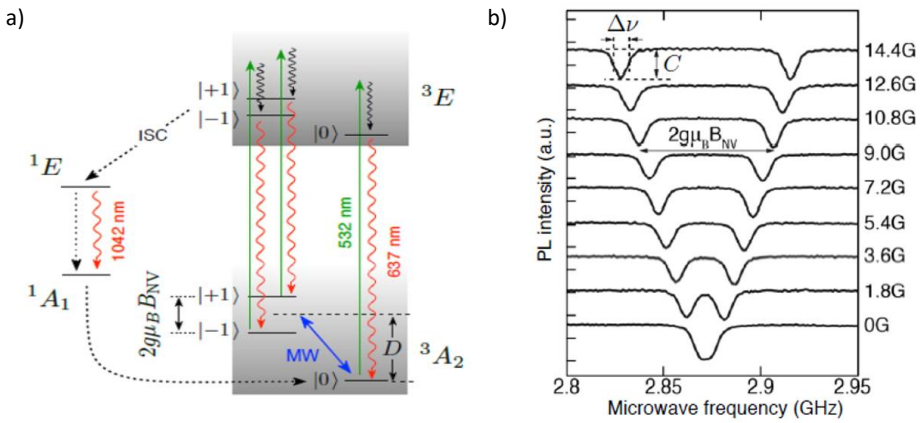

Figure 5 a) The diagram shows the energy levels and possible transitions of the NV centre together with the magnetic spin states and its relation to the external magnetic field. When electron of the NV centre is excited while resonant microwave frequency is applied it has non-zero probability to decay through the non-luminescent metastable states which can be detected as decreased intensity of red luminescence in ODMR spectrum. [5] b) Optically detected electron spin resonance (ESR) spectra for a single NV centre applying external magnetic fields of different magnitudes. [5]

As the Zeeman splitting is caused by the external magnetic field, it can reveal information about this field. The intensity of the magnetic field determines two working regimes of sensing to be distinguished: the weak field regime (< 100 mT) and strong field regime (> 100 mT). For field intensity less than 100 mT [10], the transversal component of the magnetic field is negligible and the frequency change $v_{\pm}$ in respect to magnetic field variation is approximately linear as can be seen in equation below.

$$v_{\pm} = D \pm g\mu_B B_{NV}/h \qquad (1)[5]$$

, where D is the axial zero field splitting parameter, h Planck's constant, g the g-factor of the electronic spin, μ_B the Bohr magneton and B_{NV} the magnetic field projection along the NV axis.

In Figure 5b is shown the linear dependency of the splitting on a externally applied magnetic field and demonstrates the use of the NV centres for magnetometry. The intensity of externally applied magnetic field can be calculated from the splitting $v_{\pm}$ by using the equation (1) above. In the region of 50 – 100 mT, the |0> and to |-1> level can cross. At 50 mT this crossing occurs for the excited state spin sublevel, called ESLAC (excited state level anticrossing) and at 100 mT at the ground state GSLAC (the ground state level anticrossing). At this fields, the |0> and to |-1> spin state mix. When further increasing the field, the complex will eventually enter the strong field regime. The electron spin resonance (ESR) frequencies will become strongly correlated to the orientation of the magnetic field as the NV defect axis no longer accurately represents the direction of the quantization axis. This behaviour occurs at high magnetic fields above ~ 1T applied transversally. [2]

2.3. Photoelectric detection of magnetic resonance (PDMR)

The PDMR principle relies on the photo-electric charge dynamics of the NV centre under green laser light excitation. In Figure 6 is shown that there can be another path of the excited electron comparatively to the ODMR. By two step photoionization it is possible for NV centre electron to be further promoted into the conduction band (CB). Upon its excitation to the conduction band of the diamond, it can freely travel under an applied bias electrical field and be detected in form of photocurrent.

When the electron is promoted to the CB it changes the charge state of the NV^- centre to the neutral NV^0 state. However, the photoionization of the electron from the valence band (VB) to the ground state of the NV^0 centre provides a possibility of recovering the negatively charged state. This is only possible if the photon excitation energy is larger than ~2.2 eV. [34] The full photoionization cycle thus produces in total two charge carriers (one electron and one hole): an electron by photoionization from NV^- and a hole by photoionization from VB to NV^0. Due to the charge circulation described above, the PDMR method is sustainable. The technique described could be also applied to certain other defects in diamond as well.

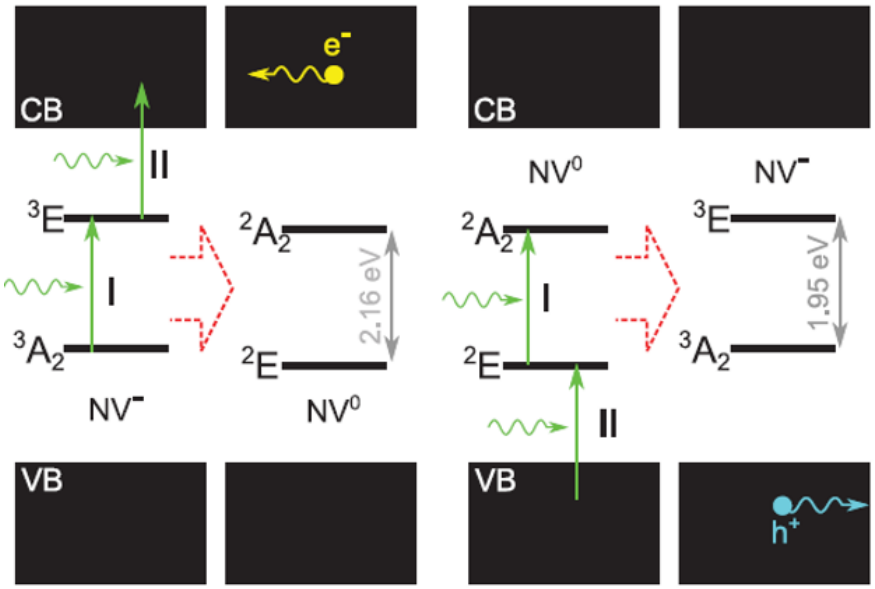

Figure 6 The simplified diagram of the energy levels and possible transitions of the NV centre electron to conduction band (CB) and its back conversion form NV0 to NV- by obtaining electron from valence band (VB)[3]

The PDMR spectrum is analogical to the ODMR, and both methods can be utilized at the same time. The working principle of PDMR is very similar to ODMR. A microwave magnetic field at the resonance frequency applied to the NV center will induce the spin sub-level transition at the ground state energy, thus the electron is promoted from $m_s = 0$ into the $m_s = \pm 1$ spin state. Followed by photoexcitation, the decay via the metastable singlet state with a probability of ~ 30% occurs leading to the reduction of photocurrent. The electron confined in the metastable state in this way is prevented from the two-step photoionization process, resulting in decrease of photocurrent intensity, analogous to the decreased level in photoluminescence in ODMR. In case that the electron is in the state $m_s = 0$, it can be either further photoionized or decay radiatively to the triplet ground state. Identically to the ODMR, when external magnetic field is applied, the resonances detected by the photocurrent readout method appear at two different frequencies in the spectrum due to the Zeeman splitting effect. The difference of those two resonances is proportional to the magnetic field applied.

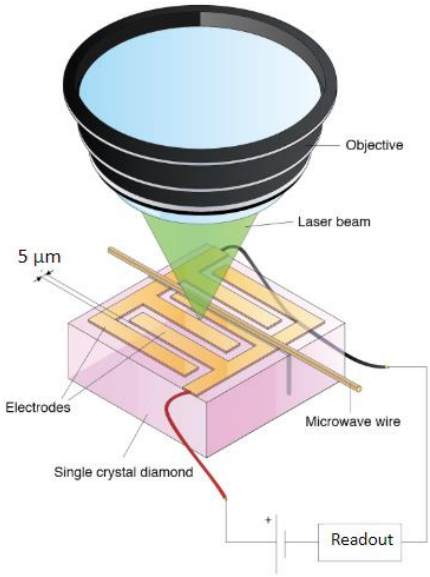

Figure 7 Simplified scheme of the PDMR readout setup [3]

Despite the similarity in principle of the ODMR and PDMR method, the signal collection rate differs. Unlike the ODMR, the PDMR charge-carrier detection rate does not saturate with the high laser power intensity.[35] Based on the assumption that the sensitivity of the magnetometer is inversely proportional to the root mean square of the detection rate, the PDMR measurements can theoretically be more sensitive than ODMR measurements. [3], [36]. This is further described in section 2.6 by equation (3). Another difference of both methods can be seen in Figure 7 where the excitation light is focused in between the electrodes fabricated on top of the diamond sample surface, while generating photocurrent signal, which is collected is via the electrodes. This way the diamond act as both sensor and a detector leading to the possibility of miniaturization of the entire system by removing the optical detection path.

2.4. Magnetic field vector measurements

Measuring of the vectorial behaviour of an ambient magnetic field as well as its magnitude are often of relevance in numerous applications. In construction of most of the classical detectors, three scalar magnetometers are orthogonally fixed to one another in order to perform vectoral measurements.[28] The precision of the manufacturing process and its calibration determines the accuracy of this procedure. In some instances, this alignment or calibration can vary over time. On the other hand, NV centres due to their placement in diamond crystalline lattice, offer the possibility to measure projection of ambient magnetic field aligned along four different NV centre axes. [30] These four directions then constitute a complete basis, with respect of which external magnetic field can be defined, which enables the use of NV based devices as vector magnetometers.

As already discussed in section 2.1., by implementing the ODMR or PDMR method, it is possible to address the NV centres and determine the projection of an external magnetic field onto is axes. [2], [5], [30] By using NV centre ensemble diamond sample when external bias magnetic field is applied, the resulting example spectrum and its corresponding NV axes are shown in Figure 8. As can be seen, the detected resonances are symmetrically centred around 2.87 GHz (ZFS) frequency. Due to their allocation to the stable diamond crystalline lattice, the measured $B_{1\text{-}4}$ can be then precisely transformed into $B_{x,y,z}$ frame of reference of the sensor itself and utilized in the appropriate applications (i.e. characterization of Earth's magnetic field or navigation).

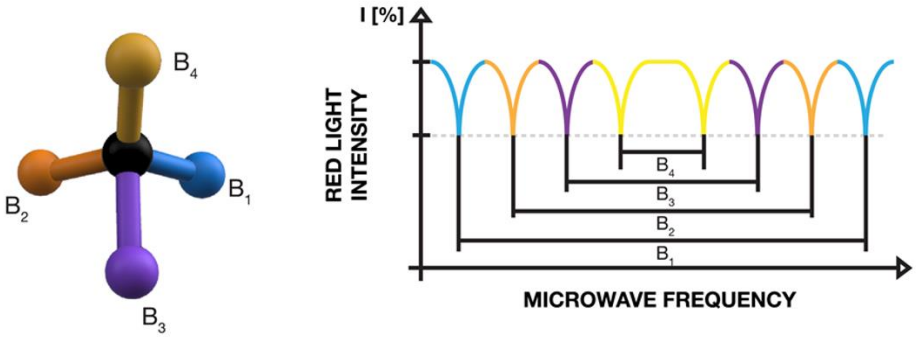

Figure 8 (left) Simplified model representation of four different NV centres alignment in diamond crystalline structure, with colours corresponding to the (right) ESR spectrum with eight resonance frequencies used to determine magnetic field $B_{1\text{-}4}$.

2.5. Pulsed quantum measurements

In addition to the Continuous Wave (CW) measurements described in sections 2.3 - 2.4, where the illumination of the NV centre with green laser light is continuous, with a simultaneous MW frequency sweep there are several pulsed measurement protocols to allow for ESR detection. The pulsed measurements are more sensitive than the conventional CW measurement technique. Not only they can lead to sensitivity improvements, but they can also be used to filter out unwanted DC or AC signals.

There is a variety of possible pulse sequences, ranging from rather simple ones to complex series of microwave and laser pulses. We will describe two basic ones: the Ramsey and Hahn echo pulse schemes. The CW method is easier to implement compared to pulsed measurement schemes. However, the use of pulsed measurements brings some extra benefits, for example frequency locking, better sensitivity, and noise decoupling. Therefore, we envision both methods being used in a complementary way.

In the following explanations the concept of the Bloch sphere [37] will be introduced. This is a schematic representation of the electronic spin state vector. This representation makes it easier to visualize the effects of the individual MW pulses. To better understand the following chapters, the terms T_1, T_2, and T_2^* relaxation times must be defined. The parameter T_1 describes how fast the spins are relaxing back from a polarised state into their equilibrium state. Coherence time T_2 is describing how long it will take the spins to decay from the superposition state to their equilibrium state (transversal spin relaxation). The T_2^*, dephasing time describes the rapid phase decoherence induced for example by the inhomogeneous magnetic field. Aforementioned times describe how long the spin is addressable before decaying or dephasing.

2.5.1. Ramsey sequence

The Ramsey sequence is shown in Figure 9 and 10. It consists of an initializing green laser pulse, followed by two $\pi/2$ pulses, separated by a free spin precession time τ (π/2 pulse means a spin rotation by π/2, i.e. creation of a superposition state). Another green readout pulse, during which the red fluorescence signal is measured, gives information about the acquired phase. The Ramsey measurements can be therefore used for spin magnetometry. In particular, when a magnetic field is applied the electron spin acquired phase is linearly proportional to the magnetic field. This technique can be used for DC B-field measurements. The optimal sensitivity is acquired when the free precession time is close to the dephasing time T_2^*. [5]

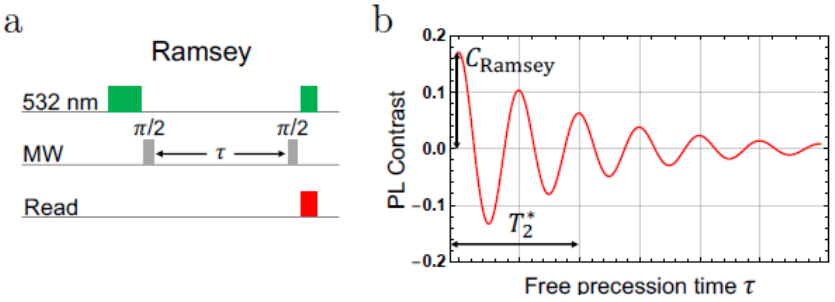

Figure 9 Ramsey sequence [9]

Aside from providing us with a higher sensitivity, employing a Ramsey pulse scheme also has the benefit of being largely insensitive to AC magnetic fields. This Ramsey sequence can be used to characterize steady magnetic fields and detailed description of the pulse scheme is illustrated on the left side of Figure 10. The positive and negative contributions of these AC fields approximately cancel each other out.

On the right side of this figure, there is a representation of the spin state vector on the Bloch sphere. The colours of the arrows on the Bloch spheres relate to the different stages of the pulse sequences with the same colour scheme.

The sequence starts by shining a green laser light on the centres. This will polarize the spin into the ground energy level with spin-state $m_s = 0$. A first $\frac{\pi}{2}$ pulse rotation over the x-axis will bring the electrons in a superposition of the $|0>$ and $|1>$ states i.e. tilting by 90 degrees. This is indicated by the dark green arrow. The red arrow indicates the precession for defined time. In presence of the B-field the spin will acquire the phase proportional to the B-field. Then another $\pi/2$ pulse is applied, which flips the electron spin state vector again by 90 degrees (light blue arrow). The readout is done with green laser light pulse. This measures the component of the electronic spin state along the z-axis after the time τ. From the acquired phase the magnetic field can be calculated, as already stated.

$$\eta_{Ramsey} \sim \frac{\hbar}{g\mu_B} \cdot \frac{1}{C\sqrt{\mathcal{L}_0 t_L R}} \cdot \frac{1}{\sqrt{T_2^*}}, \qquad (2)[5]$$

, where $\hbar$ is the reduced Planck constant, g is NV gyromagnetic ratio, μ_B is the Bohr magneton, C is the ESR contrast, v is the measured FWHM, and $\mathcal{L}_0$ is the NV defect PL rate and t_L is the readout laser pulse duration.

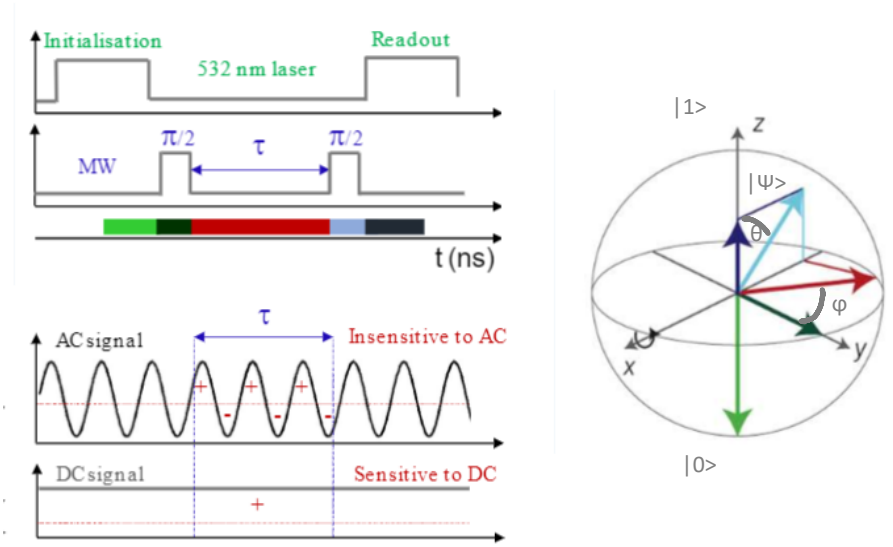

Figure 10 Ramsey pulse scheme (left) and Bloch sphere (right) scenario, where the system is initialized to a lower state (light green). A π/2-pulse creates a superposition state (dark green), and after a delay τ (red) a second π/2-pulse (light blue) is applied and the vector projection to the upper state (dark blue) is measured. The Bloch sphere in the inset shows the state of the Bloch vector at selected times, which are marked in the same colour in scheme on the left. The state of the vector can be mathematically written as $|\psi\rangle=\cos(\theta/2)|0\rangle+\exp(i\phi)\sin(\theta/2)|1\rangle$. *[37]*

2.5.2. Hahn echo sequence

Compared to the Ramsey sequence, Hahn echo features an extra π pulse halfway through the free precession time. This enables to compensate interactions with inhomogeneous magnetic field and allows to measure unperturbed coherence time T2. The Hahn sequence is illustrated on the left side of Figure 11. By the extra π pulse in the middle of the sequence the spin is flipped by 180 degrees (the brown arrow). Then it will continue to preces around the z axis, but in the opposite direction (blue arrow). Therefore, the phase accumulated during the first $\tau/2$ precession is cancelled out in the second $\tau/2$. [7]. The Hahn sequence enables the readout of AC magnetic fields.

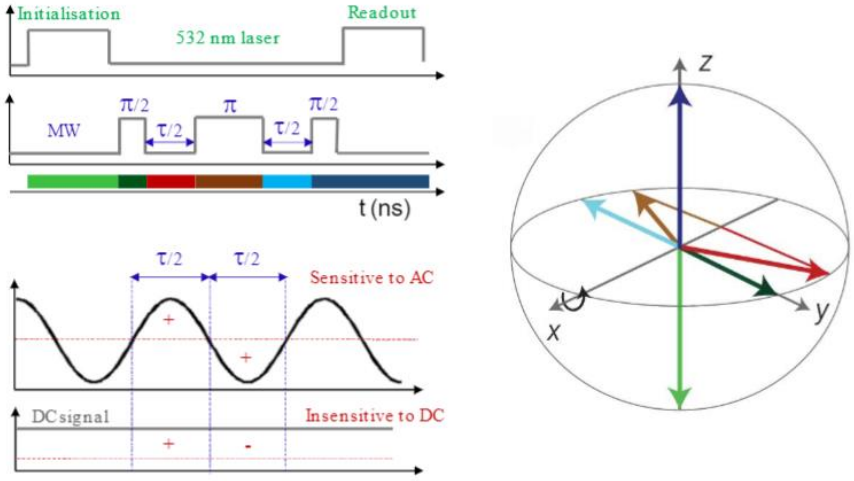

Figure 11 Hahn echo pulse scheme(left) and Bloch sphere (right). In this scenario the system is adiabatically tuned from the initialization to the lower state (light green). A π/2-pulse creates a superposition state (dark green), and after a delay of τ /2 (red) a π-pulse mirrors the state vector (brown) to the other half of the Bloch sphere. After another delay of τ /2 (light blue), a 3π/2-pulse is used to rotate to the upper state (dark blue). The Bloch sphere in the inset shows the state of the Bloch vector at selected times, which are marked in the same colour in a scheme on the left [37]

2.6. Sensitivity of continuous wave magnetic field measurements

The detected resonance has a Lorentzian function profile (see Figure 12b) from which theoretical sensitivity can be calculated.

$$\eta = \frac{4h}{3\sqrt{3}g\mu_B} \cdot \frac{v}{c\sqrt{R}} \qquad (3)[9]$$

, where h is the Planck constant, g is NV gyromagnetic ratio, μ_B is the Bohr magneton, c is the experimental spin contrast, v is the measured FWHM, and R is the detection rate (photons per second for ODMR, or electrons per second for PDMR). The formula indicates the smallest detectable magnetic field limited by so called shot noise [9] and allows to model the optimal parameters and predict the sensitivity of the system.

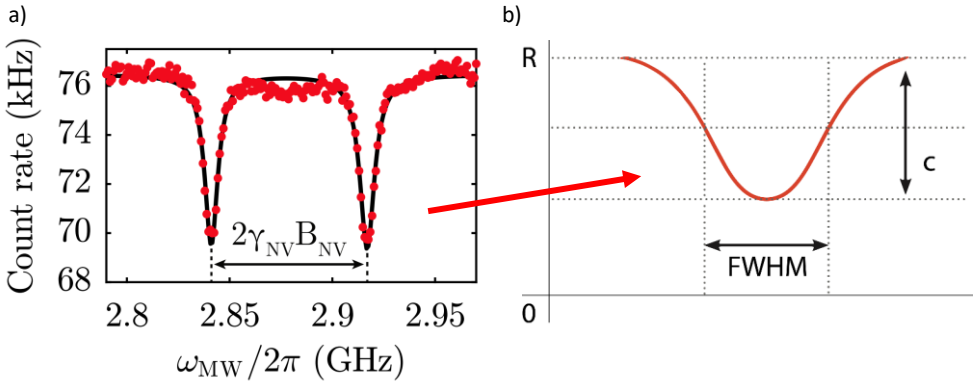

Figure 12 a) Example of optically detected electron spin resonance (ESR) of a single NV centre with applied bias magnetic field BNV. [33] b) Single peak described by Lorentzian function with key parameters to determine magnetic field sensitivity: R – photon count per second, FWHM (Δv) – full width half maximum of the resonance, c – contrast.

This is especially useful for example during sample characterization and selection of optimally performing samples for magnetometry. These characteristics are shared by most of spin-based magnetometers. PDMR provides some advantages in this case, since shot noise is reduced by the increased electron detection rate compared to PL photon detection due to limited collection efficiency of the later one and saturation under high light excitation power. [9]

The theoretical magnetic field sensitivity is given by the fundamental spin projection error which can be approached by repetitive pulsed spin projection measurements [5].

2.7. Microwave-free NV magnetometry with ground state level anti-crossing (GSLAC)

In this section a methodology is described for alternative NV magnetometry approach without needing using microwaves to induce the spin transitions [38]. The ground state level anticrossing (GSLAC) in NV centres can be utilized for microwave-free measurements of the vector magnetic field.

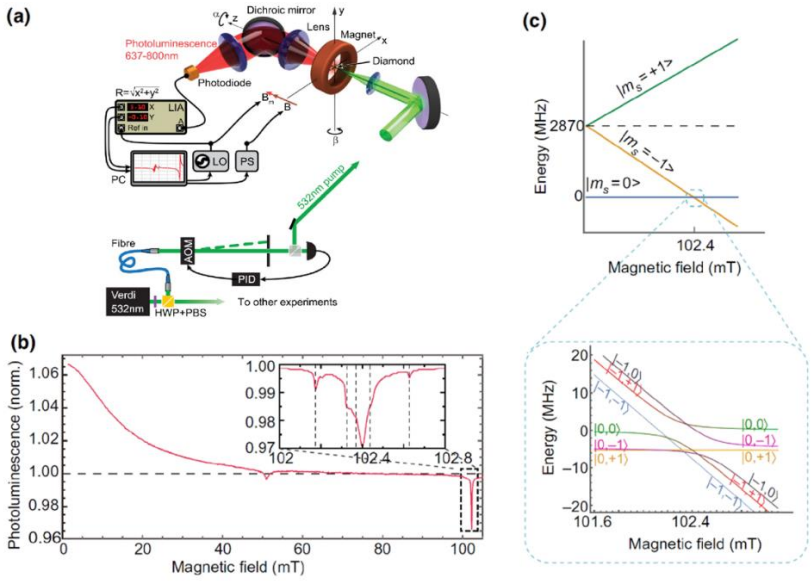

Figure 13 (a) Schematic of the experimental setup which we built up in this work. The key parts are the green laser for excitation of the NV centres, electromagnet driving the GSLAC, and detection part. (b) The photoluminescence spectrum containing GSLAC at B_0 = ~ 102.4 mT (c) The diagram of energy levels combination for the electron spin state m_s (0,-1, +1) and the ^{14}N-nuclear spin state m_I (0,-1, +1) (indicated accordingly $|m_s, m_I\rangle$). [14],[30], [37]

Figure 13a schematically describes our experimental setup for microwave-free magnetometry based on GSLAC in diamond, further detailed in Chapter 6. The typical operation principle of this technique is that green light excites the NV centres in diamond and the red-light emission is detected by the photodetector. The sweeping magnetic field is applied by the electromagnet aligned with one of the NV orientations. When B_0 = ~ 102.4 mT (Figure 13b) magnetic field is applied to the diamond, it causes the anticrossing spin mixing of spin m_s = -1 and m_s = 0 (as shown in Figure 13c), resulting in a decrease in measured red light intensity. When additional external magnetic field is applied it will perturb the anti-crossing conditions, causing a shift of the GSLAC position in the spectrum, which is proportional to the additional external magnetic field. [38]–[41]. Simultaneously with mixing the electron spins, the nuclear spins (such as N) can be polarised [37] leading to additional dips in the resonance spectra.

2.8. Diamond and NV centres fabrication

As the diamond fabrication process can influence the behaviour of the resulting system it is important to understand its underlying basics. But in the same time the author was not engaged in the diamond growth or the NV fabrication processes, therefore the production methods are described only briefly.

Two methods of diamond sample synthesis relevant to the scope of this work are the HPHT (high pressure high temperature) synthesis and CVD (chemical vapour deposition) synthesis of single crystal diamond. Samples created this way can vary by purity. The HPHT method is mimicking the natural formation of diamonds in Earth's mantle under high pressure and high temperature. The first synthetic diamond was successfully grown in 1953 by HPHT method [42].

On the other hand, the CVD made samples are grown inside a reactor at low pressures in microwave-induced CH_4 plasma with addition of hydrogen. The CH_4 is a source of carbon for the growth of diamond. An advantage of the CVD method is the possibility to tune the N-impurity level by N-doping from very pure diamond to nitrogen rich diamond needed for the NV centre formation [43]. Interesting is also a combination of HPHT or CVD substrate and CVD growth by epitaxy [43].

2.8.1. NV centres fabrication

The NV centres can be fabricated in diamond samples for example by means of Ion Implantation [44] or electron or proton Irradiation of N-doped samples [45], followed by an annealing process [46].

During the Ion Implantation the nitrogen (N+) ions are implanted with a depth resolution depending on the implantation energy (keV to several MeV) and ranging from nm to several μm [47], [48]. The implantation can be carried out through a mask, limiting the implantation to area of interest. [49]

Another way of NV centres fabrication is electron or proton irradiation. For electron irradiation the sample is exposed to electron beam of energy in order of > 250 keV [50], which leads to formation of vacancies inside the diamond lattice. To use this method, the sample needs to already contain substitutional nitrogen to convert them to the NV centres after the annealing. Alternative is a proton irradiation with energy of several MeV [50].

Annealing is an important step, required after all of the abovementioned methods to stimulate formation of NV centres. At high temperature (> 650°C) in vacuum the vacancies start migrating towards the substitutional nitrogen. This results in formation of NV centres in diamond with high NV- to NV0 ratio (7:3) [46]. The optimal annealing temperature is 900 – 1200 ^{o}C.

2.9. Lithography processing

Lithography is a process of patterning an image or features to a photoresist after which the pattern is metalized or etched. The following sections describe the basics of the photolithography processing steps in detail, whereas Figure 14 shows the chronology of the individual steps.

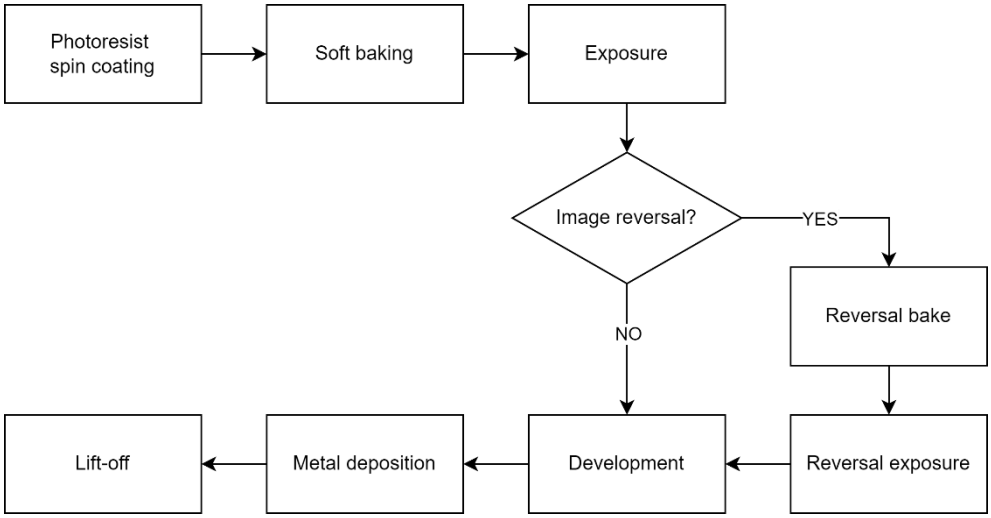

Figure 14 Chronological arrangement of the optical lithography general processing steps from photoresist spin coating up to the liftoff (with and without image reversal step)

2.9.1. Photoresist

Both optical and electron beam photoresists can be found in two types (tones): *Positive* and *Negative*. A *positive* resist is a type of photoresist in which the portion of the photoresist that is exposed to UV light becomes soluble by the photoresist developer. While a *negative* resist is a type of photoresist in which the portion of the photoresist that is exposed to light becomes insoluble in the photoresist developer.

A special kind is a photoresist with image reversal. This type is used within this work during the optical process, as it brings the possibility to use both *negative* and *positive* mask designs. The key working principle in case of the image reversal resist is heat treatment (also known as image reversal bake) which causes a flip of the image by turning *positive* image into *negative*. The selection of this approach was chosen for historical reasons as the first available masks were *negative* and the universality of this process, as both the *positive* and *negative* masks can be used interchangeably, while the process remains the same. [51]

2.9.2. Spin coating

To obtain uniform coating of the sample surface the method of spin coating is used. It involves placement of the substrate to the chuck rotating with desired speed ω (RPM) for defined duration of time t and applying a volume of photoresist on top of the sample (photoresist initial thickness h_0) to achieve desired thickness h of photoresist coating. The additional parameters are photoresist density ρ and photoresist viscosity μ. The resulting thickness can be calculated based on the equation below.

$$h = \frac{h_0}{\sqrt{1+\frac{4\rho\frac{\pi}{30}\omega h_0^2 t}{3\mu}}} \qquad (4)[52]$$

The thickness calculation mainly depends on the speed and time, and for specific photoresist can be typically found in the technical datasheet. The fluid properties, viscosity and surface tension, the spin recipe, geometrical effects of the substrate, and the Bernoulli effects are the key parameters influencing the edge and corner effect (shown in Figure 15) during spin coating reducing the uniformity and quality of photoresist coverage. [52], [53]

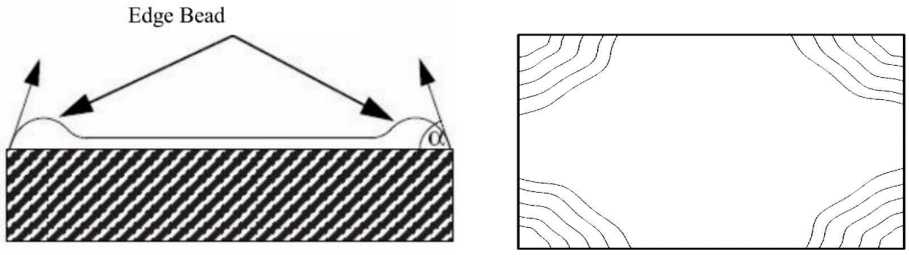

Figure 15 (left) side-view visualization of the photoresist edge bead effect at the edges of the substrate (right) top view of the photoresist buildup in the corners due to substrate geometry and Bernoulli effect [53]

2.9.3. Soft baking

Soft baking is a drying step to remove majority of the solvents from a photoresist coating and plays a very critical role. Not only it turns into a solid layer, but also the photoresist coating becomes photosensitive only after successful soft bake.

Oversoft-baking will degrade the photosensitivity of resists by either reducing the developer solubility or destroying a portion of the sensitizer. Oversoft-baking on the diamond substrate can also lead to reduced resist adhesion causing issues in next steps. Undersoft-baking will result in semi-solid/semi-liquid consistency of photoresist preventing light from reaching the sensitizer and causing the small diamond sample to adhere to a mask leading to potential damage of the mask or loss of the substrate.

Positive resists are incompletely exposed if considerable solvent remains in the coating. This undersoft-baked positive resist is then readily attacked by the developer in both exposed and unexposed areas, causing less etching resistance. [54]

2.9.4. Image-reversal bake

During the image-reversal bake step, the substrate is heated after exposure to promote cross-linking of the photopolymers. Therefore, the exposed areas of the resist lose their ability to develop, while the unexposed areas remain photoactive. The optimal baking parameters depend on the resist and the desired profile of the resist can be found in the respective technical data sheet. The temperatures are typically above 110°C for duration of minutes. The image reversal reproducibility process is relatively sensitive on parameters such as temperature, or photoresist age. [54]

2.9.5. Exposure

As mentioned, the photoresist is a photopolymer that changes its solubility in the developer solution after being exposed to certain wavelengths according to its spectral sensitivity. Typically, the spectrum is in the UV range for optical lithography or an electron beam in case of e-beam lithography. The exposure is one of the key steps in the process allowing the image (or pattern) transfer to the substrate.

In the framework of this thesis the main technique used was parallel light exposure of mask aligned with the sample using mask aligner tool. In this approach the parallel light passes through the transparent areas in the photo mask towards the photoresist film. The mask is typically made of quartz or glass as a carrier and patterns are manufactured on top out of chromium non-transparent coating, which is forming the desired pattern. The mask is brought in contact with the substrate surface and thus this process produces image of 1:1 dimensions on the exposed resist. [54]

The exposure times depend on the wavelength, power, and photoresist thickness and initial values can be found or calculated based on the specific photoresist technical datasheet.

2.9.1. Development

After the exposure the photoresist can be developed. Most widely used photoresists use aqueous bases as developers. Tetramethyl ammonium hydroxide (TMAH) is an example of developer that can be used in this process. This step is one of the most critical steps in the lithography process. The characteristics of the resist-developer interactions determine to a large extent the shape of the photoresist profile and, more importantly, the linewidth control.

The method of applying developer to the photoresist is important in controlling the development uniformity and process latitude. The samples can be developed either individually or in a batch, by using a boat of multiple samples (or wafers) developed simultaneously in a large beaker. This is usually with some form of agitation. This agitation can be either using a magnetic stirrer or simply dipping motion of the boat within the developer.

The time of the sample inside the developer is one of the critical parameters when underdeveloped portions will result in peeling off the deposited metal in next step during lift-off and the over-development will cause two things - widening of lines and the "rounding" of the top edges. The wider lines will result in unprecise dimensions of the desired pattern, whereas the "rounding" issues will lead towards worse lift-off, by increasing the conformity. [55]

2.9.2. Metal deposition

During the metal deposition step, the sample with a resist pattern is covered by a metallic thin film in order to form the electrodes. The material can be deposited by several methods, out of which interesting ones are sputtering or evaporation.

The first option is the magnetron sputtering process, which requires the generation of energetic + ions (generally Argon) that are responsible for sputtering atoms from the target (cathode) in a presence of the magnetic field. The space between target and anode (substrate holder) on which the electric field is applied contains an electron cloud. Magnetic fields cause the electrons to spiral and collide with Ar atoms, which are then ionized. The Ar+ ions are accelerated, strike the target, and knock off target atoms or clusters. [56]

The thermal evaporation is a well-known method for producing thin-film coating in which the source material evaporates in a vacuum after liquidizing it by high temperature heating. When the vacuum is sufficiently high, and the mean free path of atoms is consequently larger than the distance between the crucible and the target the vaporized metallic particles directly reach the substrate where these vapours are condensed to a solid state. In this method, an electron beam holding boat, or a resistive coil are used to accommodate the metal in the form of a powder or solid bar. In order to melt the metals, the resistive boat/coil is exposed to a large direct current (DC) or e-beams are used. [57]

2.9.3. Lift-off

After the sample has been processed (all the steps covered in sections above) the remaining photoresist must be removed. There are two classes of resist lift-off techniques: wet stripping using organic or inorganic solutions, and dry (plasma) stripping. A simple example of an organic lift-off agent is acetone. Although commonly used in laboratory environments, acetone tends to leave residues on the wafer (scumming) and is thus sometimes unacceptable for semiconductor processing. Most commercial organic strippers are phenol-based and are somewhat better at avoiding scum formation. However, the most common wet strippers for positive photoresists are inorganic acid-based systems used at elevated temperatures.

Wet stripping has several inherent problems. Although the proper choice of strippers for various applications can usually eliminate gross scumming, it is almost impossible to remove the final monolayer of photoresist from the wafer by wet chemical means. It is often necessary to follow a wet strip by a plasma descum to completely clean the wafer of resist residues. Also, photoresist which has undergone extensive hardening (e.g., deep-UV hardening) and been subjected to harsh processing conditions (e.g., high energy ion implantation) can be almost impossible to strip chemically. For these reasons, plasma stripping has become the standard in semiconductor processing. An oxygen plasma is highly reactive towards organic polymers but leaves most inorganic materials (such as those that are found under the photoresist) untouched. [58]

3. Chapter 3- Experimental setup and device fabrication

This chapter is covering the lithography process essential for the device fabrication by means of optical lithography and electron beam lithography. It also covers the main parts of the experimental setup development for the PDMR magnetometry measurements and its software.

3.1. Challenges of lithography process on small samples

Due to the diamond fabrication process, the available samples dimensions are mostly smaller than 5 x 5 mm. This results in a troublesome handling of the samples in the cleanroom environment and also brings the main challenge of the uniform photoresist coverage on top of the diamond (shown in Figure 16) substrate, required by the fine structures and patterns reaching resolution of several μm. The major source of photoresist non-uniformity is the edge bead effect, described in section 2.9.2. Those effects are even more pronounced on the small samples where they dominate and prevent successful patterning process.

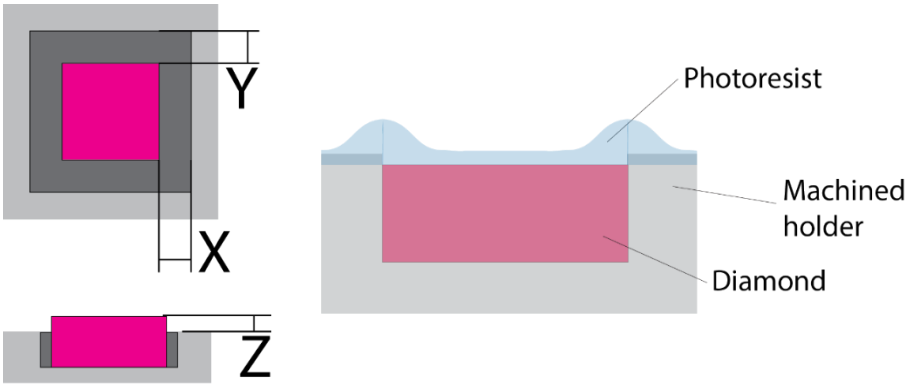

Figure 16 Sample holder parameters (left) affecting the edge bead effect during spin-coating (right)

3.2. Sample holder fabrication by silicon wafer etching

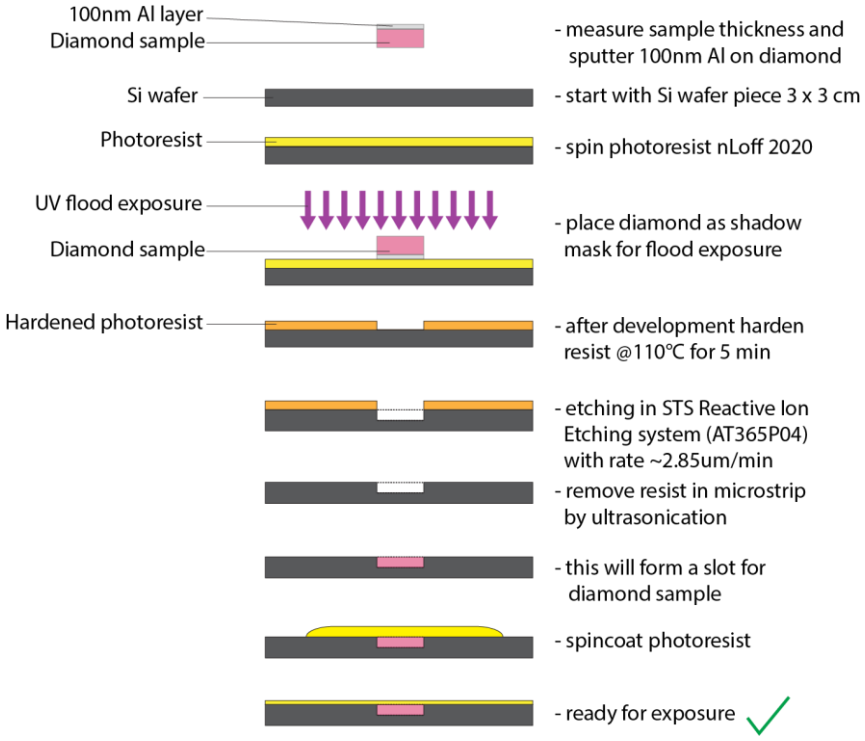

Figure 17 Fabrication process of diamond sample holder by silicon wafer deep reactive ion etching

In Figure 17 is shown the fabrication process of diamond holding socket into the silicon wafer by reactive ion etching process. The processing parameters for the photoresist mask are shown in Table 1 below:

Table 1 Processing parameters for negative photoresist AZ® nLof 2020

Step name	Parameter	Time
Dehydrate silicon wafer substrate	190°C	10 min
Spincoat photoresist on wafer	1000 rpm	35 s
Softbake of the wafer with resist	110°C	60 s
Flood exposure of the resist with diamond as a shadow mask on top	Flood exposure (MA6)	4 s
Post-exposure resist baking	110°C	60 s
Immersion in photoresist developer	Fujifilm OPD5262	90 s
Rinse in deionized water	-	-
Post-bake for STS Reactive Ion Etching	110°C	5 min

3.3. Automated process of 3D printed sample holder fabrication

In section 3.2 we described process of sample holder fabrication in cleanroom environment by etching a socket into the silicon wafer. Despite this process was proven successful and produced reproducible lithography results, and enabled to accommodate irregular shapes of diamond samples, it had several drawbacks. The main disadvantage was long fabrication time of up to 10 hours. This combined with the inconsistent and variable etch rate, the socket depth was not always perfectly fitting. When the critical dimensions were outside the limits, the process needed to be restarted. The silicon wafers are also fragile and can release hazardous dust particles, during handling.

Therefore, in Figure 18 a novel automated method utilizing SLA 3D printing approach of the sample holders is shown. This method, combined with the parametric generation of the holder 3d model, is based on a calibrated sample photo and sample thickness measurement. It significantly reduces the time needed to fabricate sample holder. This reduces overall time of the lithography process and amount of processing steps. Except for the time reduction, there is reduction in costs in materials and chemicals. Another advantage of this approach allows to design holders with constant thickness of material between the diamond and bottom part of the holder, and to apply custom correction factors in sample holder socket dimensions. Which in turn further improves the reproducibility of the method by controlling all the critical parameters. Additionally, it allows customization of the holders by e.g., adding a text or markers, which is useful especially when handling samples of similar dimensions. The 3d printed resin models are after washing and curing non-toxic.

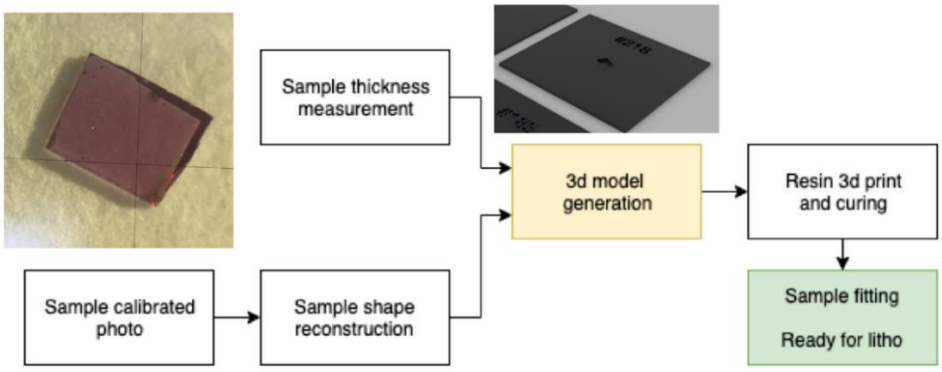

Figure 18 Simplified schematic for the 3D printed sample holder procedure

Figure 19 contains code example used for automated generation of the sample holder 3d model in open source software OpenSCAD [59]. This code example is used for samples with square or rectangular dimensions.

```
id = "#256";

sampleLength = 2.8;
sampleWidth = 2.8;
sampleHeight = 0.5;

XYcorrf = 0.025;
Zcorrf = 0.05;

h = 0.0001;
r = 3;

x1 = 20-r*2;
y1 = 20-r*2;
z1 = 1.5-h;

x2 = sampleLength+XYcorrf;
y2 = sampleWidth+XYcorrf;
z2 = sampleHeight+Zcorrf;

r1 = 0.5;
difference(){
 minkowski(){
  cube([x1,y1,z1], center = true);
  cylinder(h, r, center=true);
 }
 translate([0,0,z2])
 cube([x2, y2, z2], center = true);

 translate([-0.4,y1/2.3, z1/2-0.5+h])
 linear_extrude(0.5)
 text(id,2.5,halign = "center", valign = "center");

 translate([x2/2,0,z2])
 cylinder(z2,r1,r1, center = true);

 translate([-x2/2,0,z2])
 cylinder(z2,r1,r1, center = true);

 translate([0,y2/2,z2])
 cylinder(z2,r1,r1, center = true);

 translate([0,-y2/2,z2])
 cylinder(z2,r1,r1, center = true); }
```

Figure 19 Code snippet for the parametric sample holder 3D model generation in OpenSCAD

Figure 20 shows sample holder generated by the aforementioned code snippet in OpenSCAD and the manufactured sample holder with diamond sample inserted into the socket. Figure 21 shows the dimensional accuracy of this method, where the sample is protruding from the socket by 6.7 µm and lateral dimensions are producing gap between sample and holder of ~150 µm.

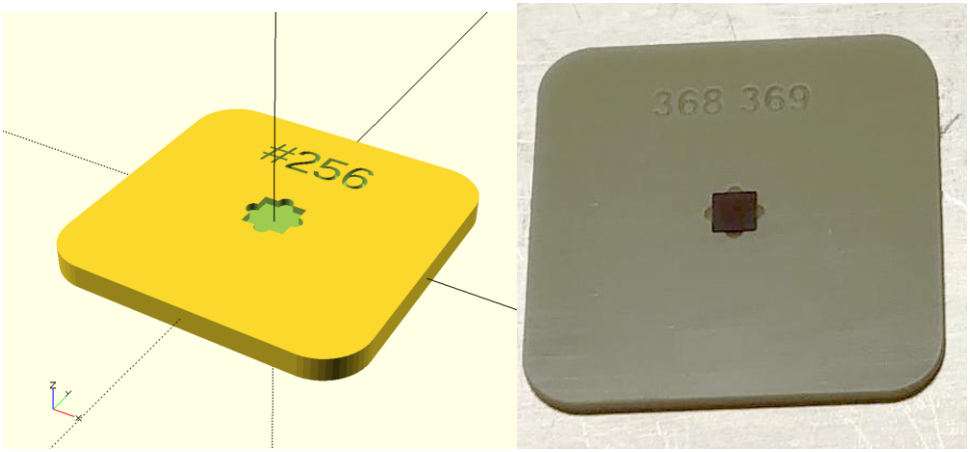

Figure 20 (left) Sample holder generated in the OpenSCAD by the parametric generated code based on the sample dimensions (right) 3D printed sample holder with diamond sample (2.9 x 2.9 x 0.5 mm^3) inserted in the well-fitting socket

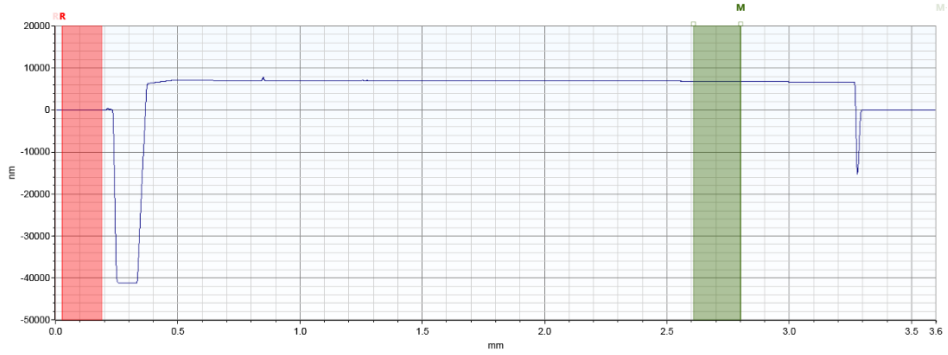

Figure 21 Profilometry measurement of the sample (#369) inserted inside the socket, shows the height difference between holder (R - red) and sample (M – green) is 6.7 µm and lateral gap is approximately 150 µm

3.4. Optical lithography process

This section covers the optical lithography process and the mask design used within this work. The optical lithography photoresist used in this work is AZ 5214E (Microchemicals) in both EU and JP versions, the recipe for both is identical.

3.4.1. Optical mask design

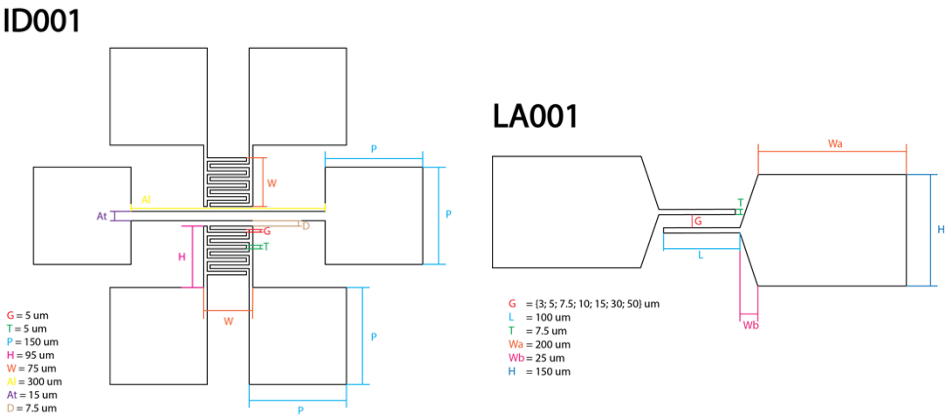

Figure 22 Design of two electrode patterns used for successful PDMR measurements (left) interdigitated electrodes of 5μm gap with patterned antenna (right) linear electrodes array ranging from 3μm to 50μm

The lithography mask is essential for transferring the desired pattern to the sample. In course of this work two main designs (ID001 and LA001) have been develop and are discussed in Figure 22. The ID001 is an interdigitated electrode design, with gap of 5 μm. In between of two electrode pairs a microwave antenna is placed which is used to transmit the microwave field on the sample necessary for ODMR and PDMR measurements. This pattern allows to deposit array of 16x ID001 electrode pairs on the 3 x 3 mm sample surface and is used mainly to cover larger areas of the sample, enabling to study different regions of the sample determined by laser excitation spot or collect photocurrent from larger area when using defocused light or larger laser spot diameter. The second most used pattern is LA001, which is an array of linear electrodes with variable gap from 3 μm to 50 μm. The microwave antenna in this pattern is placed perpendicular to the electrodes. Those electrodes are typically used for bulk (i.e., homogenous) samples.

The overview of the mask is shown in Figure 23 and it contains several different pattern types and their variations. The mask is divided into four repeating quadrants. Two blue quadrants are designed to be used with positive photoresist and two red quadrants are designed to be used with negative photoresist. This design feature is improving the mask longevity as well as its versatility.

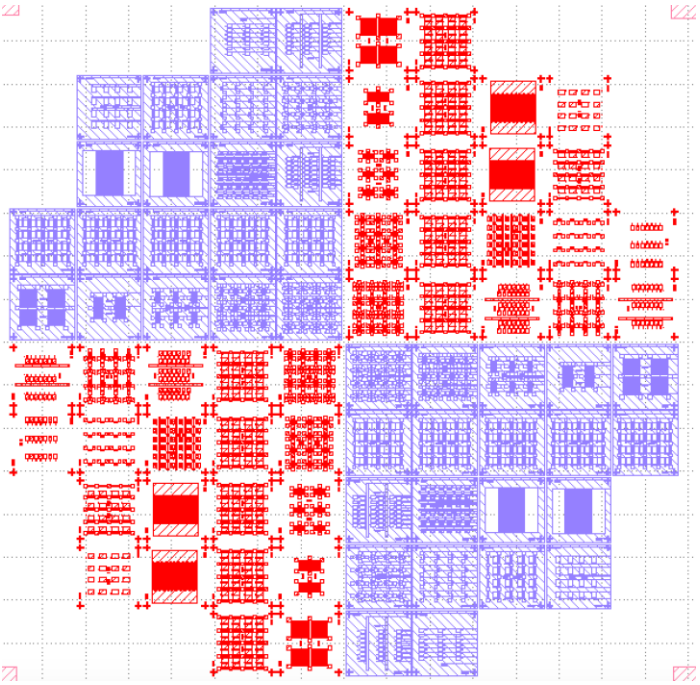

Figure 23 Mask layout containing various designs optimized for 3 x 3 mm samples arranged in four quadrants, two for positive resist (blue) and two for negative resist (red).

3.4.2. Optical lithography methodology

Table 2 chronologically describes the processing parameters for spin coating of photoresist AZ® 5214E. This photoresist can be used in both positive mode and in negative mode by use of image reversal methodology (image reversal steps are marked red in the table below).

Table 2 Processing parameters for photoresist AZ® 5214E with image reversal (IR STEP)

Step name	Parameter	Time
Spin coat photoresist on a sample holder with embedded diamond	5000 rpm	30 s
Softbake of the holder with resist	90°C	60 s
Exposure with aligned mask	Soft contact (MA6)	3 s
Post-exposure resist baking (IR STEP)	120°C	30 s
Flood exposure with blank glass (IR STEP)	Flood exposure (MA6)	5 s
Immersion in photoresist developer	AZ® 351B : H_2O (1 : 4 ratio)	Max 60 s
Rinse in deionized water	-	-

After the photoresist spin coating and pattern development on the sample, the next step is metal deposition by sputtering. The recipe used is:

- 30s soft oxygen plasma for accidental photoresist monolayer removal and oxygen diamond surface treatment
- Titanium 20 nm or 5nm thick
- Aluminium 100 nm or 20 nm thick

The titanium and aluminium are deposited in-situ without venting the system and breaking vacuum which prevents forming titanium oxide. The material choice is titanium because it can form interface layer with good adhesion with diamond and also the top layer, which is in this case aluminium. The aluminium is chosen to ease wirebonding. Both metal stack thicknesses (Ti/Al - 20/100 and 5/20) were tested for wirebonding to produce stable layers.

After the metal deposition the next step is the liftoff. This is done by ultrasonicating the sample in a Teflon boat in warm (55°C) acetone for about 15 minutes. After the liftoff in the acetone, it is sonicated in isopropanol for 2 minutes, followed by thorough washing in deionised water and drying by compressed air.

3.4.3. Optical lithography results

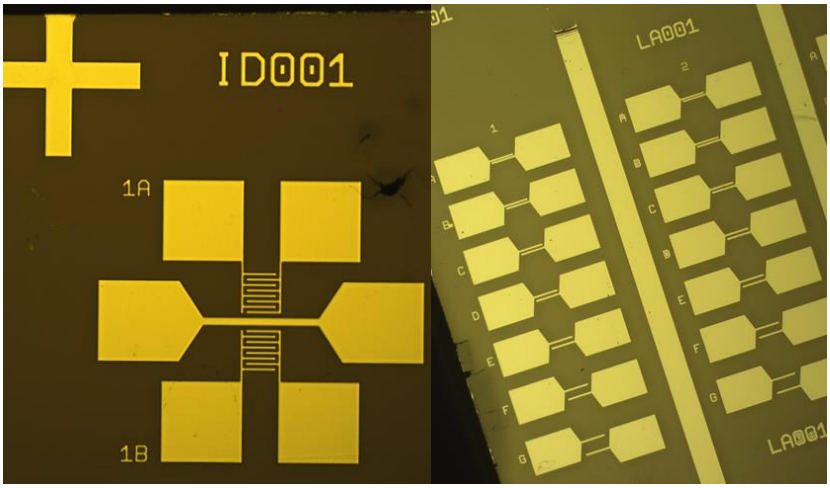

Figure 24 (left) interdigitated electrodes (ID001) of 5μm gap with patterned antenna (right) linear electrodes array ranging from 3μm to 50μm

The Figure 24 shows the ID001 and LA001 final device patterns after successful development, metal deposition, and lift-off. The above-described method is highly reproducible, with the resist uniformity allowing "edge to edge" sample coverage lithography. This result is significant as it confirms the lithography method developed in course of this thesis is suitable for small diamond samples.

3.5. E-beam lithography process

To achieve sub-micron resolution of the patterned structure, e-beam lithography was explored. The process was adapted to diamond sample inside the holder and usable electrodes down to 200nm electrode gap were developed by the following process.

3.5.1. E-beam mask design

Table 3 Marking and electrode gap used in the mask design

Marking	**A**	**B**	**C**	**D**	**E**	**F**	**G**
Electrode gap (nm)	100	200	500	800	1000	2500	50

The mask designed for the E-beam lithography benchmarking on small diamond samples was composed of linear electrode array ranging from 50 nm to 2500 nm gap (as shown in Table 3 and in Figure 25).

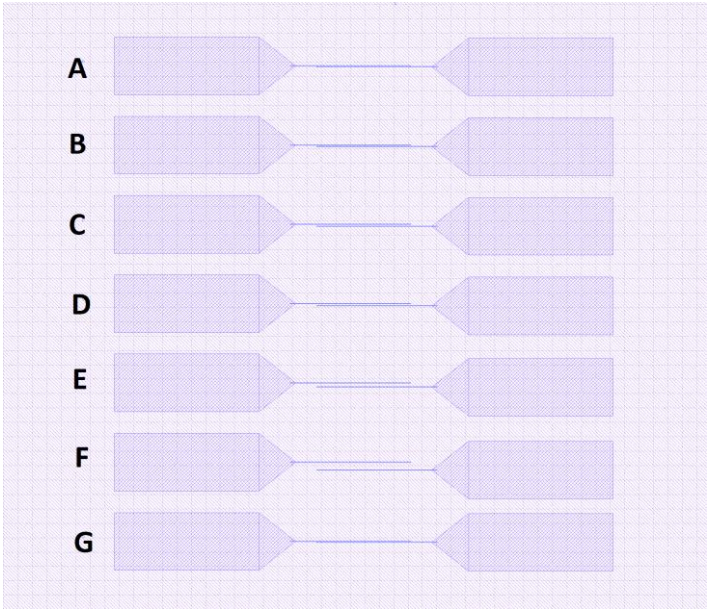

Figure 25 Mask design for benchmarking of the e-beam process on small diamond samples

3.5.2. E-beam methodology

Table 4 Processing parameters for PMMA in Anisole (PMMA3A)

Step name	Parameter	Time
Layer 1		
Spincoat PMMA3A	1000 rpm	30 s
Softbake of the holder with resist	120°C	120 s
Layer 2		
Spincoat PMMA3A	3000 rpm	30 s
Softbake of the holder with resist	120°C	120 s
ESPACER™ 300Z coating	5000 rpm	30 s
ESPACER™ dry bake	90°C	30 s

In Table 4 the processing parameters are chronologically described for spin coating of two layers of PMMA3A (3% PMMA in anisole). The PMMA is used for E-beam lithography.

3.5.3. E-beam results

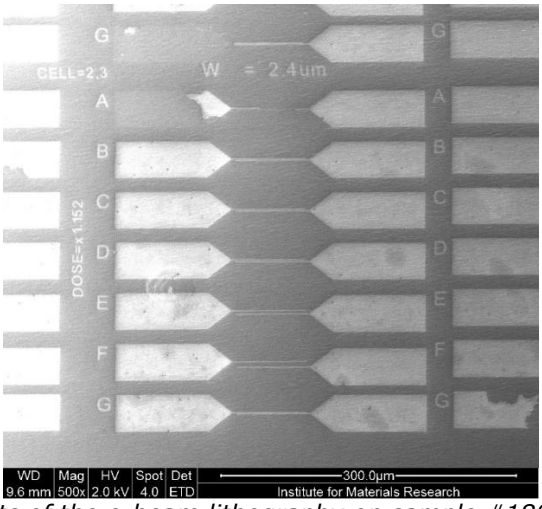

Figure 26 Results of the e-beam lithography on sample #180, electrode gap sizes corresponding respectively to the electrode marking are shown in Table 3

The results, shown in Figure 26, confirm the viability and usability of the above-mentioned procedures to prepare nanoscale contacts on top of the diamond sample by e-beam lithography. It opens further possibilities for more complex applications and, in combination with PDMR method, it will enable to downscale the readout structures to surpass the spatial resolution of ODMR, limited to ~ 250 nm due to optical diffraction.

The yielded devices were inspected by SEM (scanning electron microscopy). Then, the 200 nm electrode pair (B) was wirebonded on each respective pad and tested on the measurement setup, where the usability of the electrodes was confirmed by measuring IV curves in range ±1 V (5 V/μm) first in dark, and then under 1mW green laser illumination (see Figure 27).

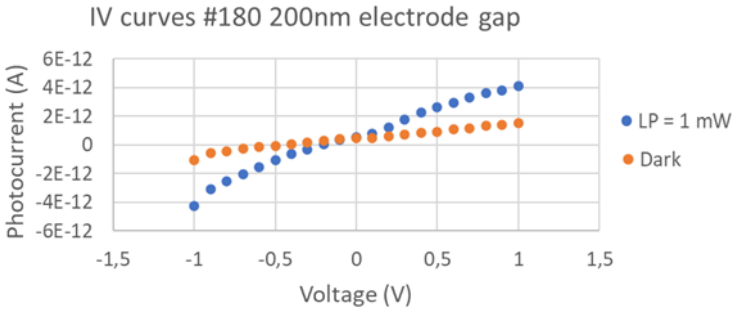

Figure 27 IV curves on sample #180 with e-beam electrodes with 200 nm gap (position B) performed in dark (orange) and under 1 mW green illumination (blue)

3.6. Laboratory measurement and setup description

During this PhD research four different NV measurement setups have been developed and used for various laboratory measurements. Each setup is dedicated to a slightly different task. Due to this, the hardware of each of the setup slightly differs in purpose. The key differences are briefly described further in this section.

Section 3.6.1 describes the general setup layout followed by a full list of hardware used across the setups. The component name and type, the communication interface and protocol used within the software, if applicable, are included. It also summarizes the list of used commands and/or functions and provides link to the user manual. All the laboratory setups were equipped with a control software developed during this PhD work.

Section 3.6.2 discusses the automated software and serves as a guide for the user to be able to navigate in the program. The section summarizes the global and high-level overview of the control software, going deeper into routines and subroutines and addressing the key functions of the program. The major focus is dedicated to the software main loop (see section 3.6.2) as it contains the core functionality of the program and is essential to understand the measurement routines and the principle of operation. The chapter 3.6.3 contains the detailed description of the setup hardware components.

The setups and their key differences are described on following pages.

3.6.1. General setup layout

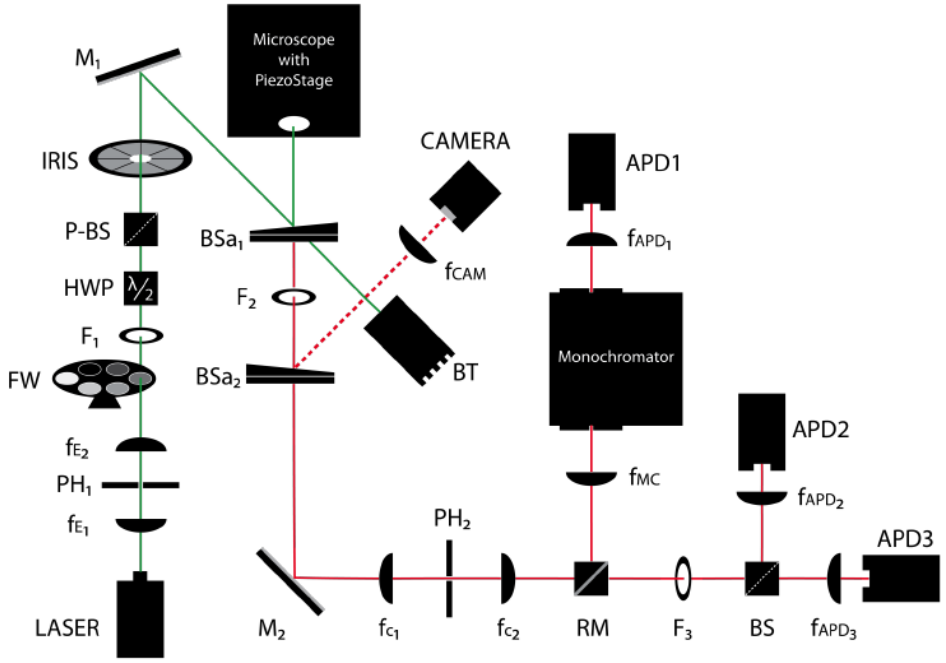

Figure 28 General confocal setup layout

In Figure 28 is shown the example of general layout of scanning confocal fluorescence microscopy setup that can be used for the imaging and measurements on NV centres in diamond. The laser is used for the sample excitation, piezostage is used for fine sample scanning to search for NV centres or specific location on the sample, avalanche photodetector (APD) can be used to collect the signal after filtering out the green light by a filter. Alternatively, the detection beam can be routed to more advanced systems such as spectroscopy-based measurements, utilized via monochromator/detector system or a spectroscopy camera. Furthermore, the setup can also vary by the sample mounting alignment (as shown in Figure 29), having impact on complexity, ease of use, magnetic field access, and spatial footprint. In the figure can be seen multiple optical parts playing role in laser beam parameters or otherwise useful for the setup performance. Those are i.e., pinhole (PH), half-wave plate (HWP), filter wheel (FW), mirrors (M) and lenses (f), beam trap (BT), beam splitters (BS), or removable mirrors (RM).

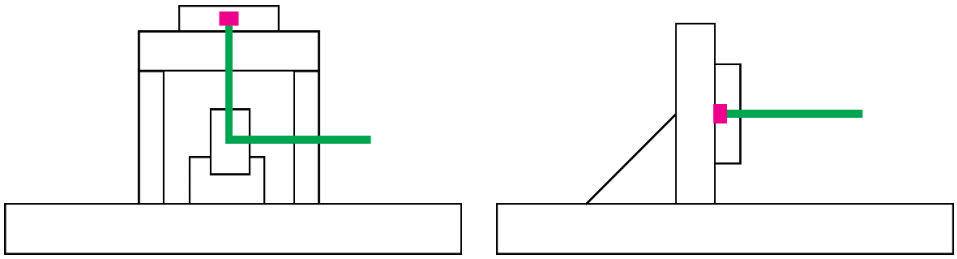

Figure 29 Setup alignment layout schematics (left) vertical alignment (righ) horizontal alignment. Purple rectangle represents the diamond sample containing NV centres, green line represents the excitation laser light.

Setup 1 (Spectroscopy setup)

The key difference of Setup 1 from all the other measurement setups is, that it is equipped with Andor spectroscopy camera for acquiring spectroscopy information of the samples. The setup is used to characterize for example diamond sample and to measure their characteristics. At the current date the system is equipped with Keysight AWG enabling pulsed measurements by synthesizing high frequency arbitrary waveforms and pulses.

Setup 2 (Magnetometry setup)

The Setup 2 is most often used for magnetometry measurements and is equipped with magnet holder for the purpose of ODMR/PDMR resonance splitting. The S2 also has automated control of laser intensity by robotic polarizing wheel and servo-controlled detector.

Setup 3 (NMR setup)

The Setup 3 is equipped with a Time-tagger and Pulse streamer (Swabian Instruments) and was designed mainly to perform NMR on single NV. The system is equipped with series of microwave switches enabling the complex MW + RF sequences necessary for NMR operation.

Setup 4 (OSCAR-QUBE test bench setup)

The Setup 4 is specialized setup designed as test bench model for the project OSCAR-QUBE magnetometer. The system is designed as "low-budget" simplification of the measurement system. Compared to the other systems, this system is not a confocal system and does not have piezo controlled stage, instead has XYZ stepper motor stage.

Hardware comparison list

The hardware on each setup varies because each of the systems has a different use, which is also reflected by the hardware used. In table below the key hardware differences of each system are listed. However, despite the differences, the software mainframe is the same with modular control of individual hardware resources.

Table 5 Comparison of key hardware components between experiment setups

	S1	**S2**	**S3**	**S4**
Microwave	Keysight AWG	SR SG380	Windfreak synthNV	OSCAR
Laser	GEM 532	GEM 532	GEM 561	OSCAR
Stage	PI piezo	Piezoconcept	PI piezo	PI stepper
Preamp	SR570	SR570	SR570	Femto 10e10
Lockin	SR830	AMETEK 7270	SR830	None
Readout	NI card	NI card	NI card + Timetagger	OSCAR
Bias	Keithley 2400	Keithley 487	Keithley 487	OSCAR

3.6.2. Setup software

The software can be divided into 4 sections: Initialization sequence, Utility loop, Main loop, and Master stop loop shown in the Figure 30. The sequence is that upon launch of the program, the initialization sequence initializes all the GUI values for easy user interaction and initializes the communication protocols with the hardware. During this part all the VISAs and COM ports are established and are used as local variables across the system.

The design of the main loop of the program is illustrated in Figure 30. It can be separated into individual modular components. The components are measurement selection, various GUI operations for user friendly operation, photon counting and photocurrent readout on idle, control routines to prevent running of multiple concurrent processes at the same time in order to protect the measurement system. Finally, it consists of 4 main tasks: XY(Z) scan, Depth scan, ODMR/PDMR sweep, and Pulsed measurement. After which all the data are saved to the drive. All the components are further described in following sections.

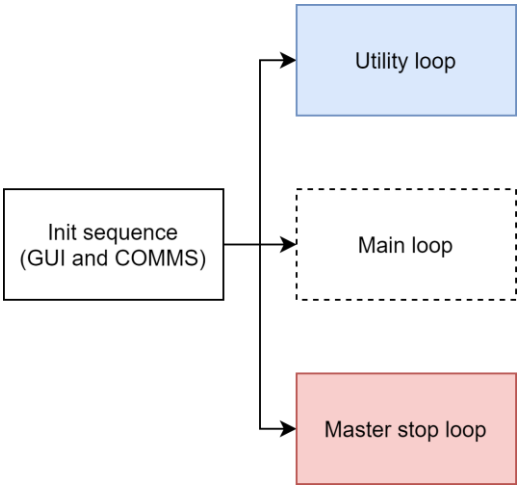

Figure 30 Global software layout

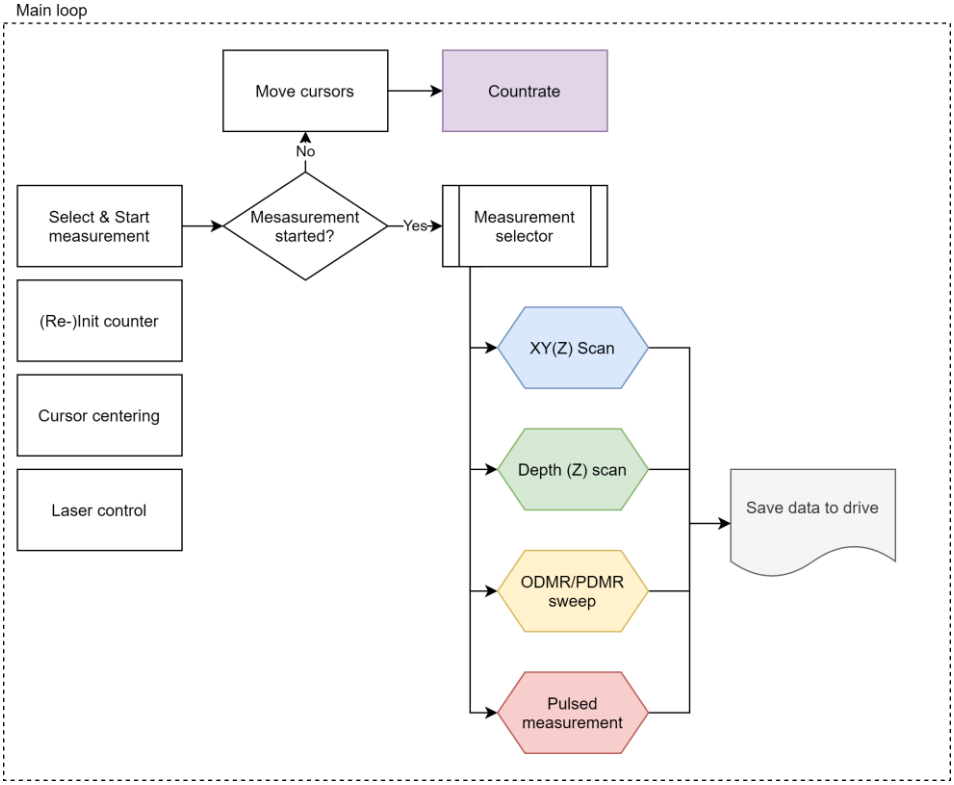

Figure 31 General main loop overview

Figure 32 and Figure 33 contain description of the main control software graphical user interface layout. It allows the user to map the sample, find and optimize the position of NV centres and to run the ODMR and PDMR measurements. The control system is also enabling the user to run pulsed measurements described in the abovementioned chapters. The acquired data are then automatically saved and file with measurement parameters generated to maintain measurement log and are backed up to the Google Drive for later data postprocessing.

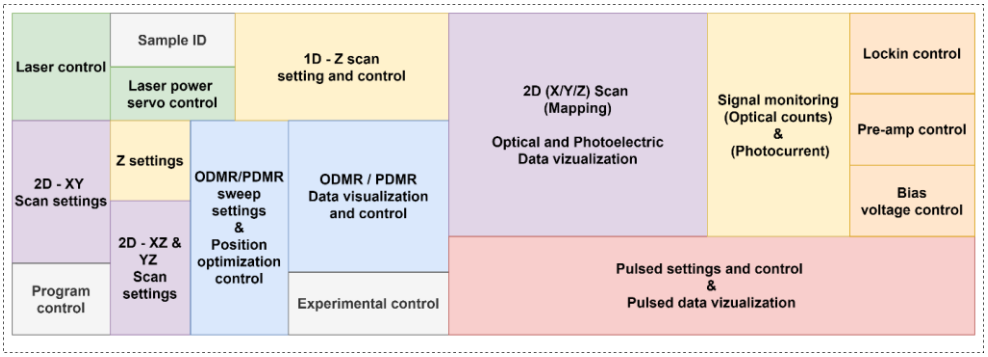

Figure 32 GUI general layout schematics

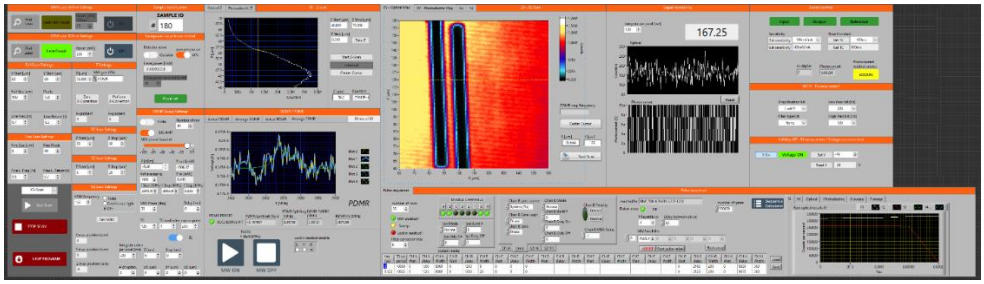

Figure 33 Global GUI layout overview preview

3.6.3. Setup 1 (Spectroscopy setup)

Here below are listed all the hardware components of the Setup 1 laboratory system.

Table 6 List of equipment currently present on setup 1 (by 02/02/2021)

Function	Part/device	Model	Company	Description
Optical excitation	Green laser	Gem 532	Laser Quantum	CW solid-state laser, 532 nm emission wavelength, 500 mW maximal power
Pulsing	Acousto-optic modulator (AOM)	AOMO 3200-146	Crystal Technology	20 ns rise time, 31 MHz modulation bandwidth, 1000:1 contrast ratio, 80 % diffraction efficiency
	RF source	AODR 1200AF-DIF0-1.0	Crystal Technology	Digital modulation, 200 MHz frequency, 1 W output power
Separation of PL light from laser excitation	Dichroic mirror	DMLP550L	Thorlabs	Ø2" Longpass Dichroic Mirror, 550 nm Cut-On
Focusing of laser light on sample (objectives shared with other confocal set-ups)	Oil objective	PlanApo N	Olympus	60X, NA = 1.42, W.D = 170 µm
	Water objective	UplanSApo	Olympus	60X, NA = 1.2, W.D = 130 to 210 µm

	Air short-distance objective	UPlanSApo	Olympus	40X, N.A. = 0.95, W.D = 110 to 230 µm
	Air long-distance objective	M Plan Semi-Apochromat	Olympus	100X, N.A. = 0.8, WD = 3.4 mm
Sample movement	Electric xy stage for coarse movement	Omicron	Vacuum Physik	Electric XY Microscope Stage
	Piezoelectric xyz stage	PZT flexure stage P-517K023	PI	XYZ Piezo System, 100 µm × 100 µm × 20 µm
	Piezo stage controller	E-501.00	PI	Digital Multi-Channel Piezo Controller, 3 Channels, 90 to 120 V, Sub-D Connector(s), Capacitive Sensors, Analog Inputs
Photoluminescence detection	Pinhole	P30S	Thorlabs	Ø1" Mounted Precision Pinhole, 30 ± 2 µm Pinhole Diameter
	Long-pass Spectral filter to block laser light	FELH0550	Thorlabs	OD > 5
	Long-pass Spectral filter to select NV-PL	FELH0650	Thorlabs	OD > 5

	Band-pass Spectral filter to select GeV PL	FB600-10	Thorlabs	
	Short-pass Spectral filter	FES0600	Thorlabs	
	Single photon counter	SPCM-AQRH-14	Excelitas Technologies	Dark counts < 100 cts/s, dead time: 20 ns, Output count rate before saturation: 40 MCts/s
	Gating for time-resolved measurements	MCS8A	FastComtec	200 MHz digital channel
	Gating for time-resolved measurements	PCIe-6374	National Inst.	3.5 MHz analog channel, 10 MHz digital channel
Photoelectric detection	Voltage source	Keithley 6221	Tektronix	0-105V
	Voltage source	SM 7020	Delta Electronika	0-70V, Higher voltage stability compared with Keithley 9221
	Current-to-voltage preamplifier	SR570	Standford Research Systems	5 fA/√Hz input noise, 1 MHz maximum bandwidth (at low amplification), 1 pA/V maximum

				gain, configurable signal filters
	Current-to-voltage preamplifier	DLPCA-200	Femto	440 fA/√Hz input noise at 400kHz and 100 nA/V
	Lock-in amplifier	SR830	Standford Research Systems	1 mHz to 102.4 kHz range, >100 dB dynamic reserve, 0.01 degree phase resolution, Time constants from 10 µs to 3 ks
MW signal generation, amplification and pulsing	MW source	SynthHD Pro	Windfreak	54MHz – 13.6GHz, +18 dBm output power, 0.01 dB amplitude output power step size
	MW amplifier	ZHL-16W-43-S+	Mini-Circuits	1800 to 4000 MHz, gain: 45 dB, gain flatness: ±2.0 dB
Pulse sequences generation	Arbitrary wave generator	M8190A	Keysight	4 digital and 2 analog output channels, 8 GSa/s sampling rate
Spectroscopy	Spectrometer and CCD camera	Kymera 193i-A	Andor	180-1200nm

3.7. References for Chapters 1-3

[1] C. L. Degen, F. Reinhard, and P. Cappellaro, 'Quantum sensing', *Rev. Mod. Phys.*, vol. 89, no. 3, p. 035002, Jul. 2017, doi: 10.1103/RevModPhys.89.035002.

[2] T. Wolf *et al.*, 'Subpicotesla Diamond Magnetometry', *Phys. Rev. X*, vol. 5, no. 4, p. 041001, Oct. 2015, doi: 10.1103/PhysRevX.5.041001.

[3] E. Bourgeois *et al.*, 'Photoelectric detection of electron spin resonance of nitrogen-vacancy centres in diamond', *Nat Commun*, vol. 6, no. 1, p. 8577, Oct. 2015, doi: 10.1038/ncomms9577.

[4] 'Orbit Your Thesis'. https://www.esa.int/Education/Orbit_Your_Thesis (accessed Sep. 29, 2021).

[5] L. Rondin, J.-P. Tetienne, T. Hingant, J.-F. Roch, P. Maletinsky, and V. Jacques, 'Magnetometry with nitrogen-vacancy defects in diamond', *Rep. Prog. Phys.*, vol. 77, no. 5, p. 056503, May 2014, doi: 10.1088/0034-4885/77/5/056503.

[6] W. K. Tobiska *et al.*, 'Global real-time dose measurements using the Automated Radiation Measurements for Aerospace Safety (ARMAS) system', *Space Weather*, vol. 14, no. 11, pp. 1053–1080, 2016, doi: 10.1002/2016SW001419.

[7] N. Lu *et al.*, 'Application of Airborne Magnetic Survey in Deep Iron Ore Prospecting—A Case Study of Jinling Area in Shandong Province, China', *Minerals*, vol. 11, no. 10, Art. no. 10, Oct. 2021, doi: 10.3390/min11101041.

[8] M. Gulka *et al.*, 'Room-temperature control and electrical readout of individual nitrogen-vacancy nuclear spins', *Nat Commun*, vol. 12, no. 1, p. 4421, Jul. 2021, doi: 10.1038/s41467-021-24494-x.

[9] J. F. Barry *et al.*, 'Sensitivity optimization for NV-diamond magnetometry', *Rev. Mod. Phys.*, vol. 92, no. 1, p. 015004, Mar. 2020, doi: 10.1103/RevModPhys.92.015004.

[10] I. Schwartz *et al.*, 'Blueprint for nanoscale NMR', *Sci Rep*, vol. 9, no. 1, p. 6938, May 2019, doi: 10.1038/s41598-019-43404-2.

[11] D. B. Bucher *et al.*, 'Quantum diamond spectrometer for nanoscale NMR and ESR spectroscopy', *Nat Protoc*, vol. 14, no. 9, pp. 2707–2747, Sep. 2019, doi: 10.1038/s41596-019-0201-3.

[12] J. Zopes, K. S. Cujia, K. Sasaki, J. M. Boss, K. M. Itoh, and C. L. Degen, 'Three-dimensional localization spectroscopy of individual nuclear spins with sub-Angstrom resolution', *Nat Commun*, vol. 9, no. 1, p. 4678, Dec. 2018, doi: 10.1038/s41467-018-07121-0.

[13] P. Maletinsky *et al.*, 'A robust scanning diamond sensor for nanoscale imaging with single nitrogen-vacancy centres', *Nature Nanotech*, vol. 7, no. 5, pp. 320–324, May 2012, doi: 10.1038/nnano.2012.50.

[14] K. Bian *et al.*, 'Nanoscale electric-field imaging based on a quantum sensor and its charge-state control under ambient condition', *Nat Commun*, vol. 12, p. 2457, Apr. 2021, doi: 10.1038/s41467-021-22709-9.

[15] G. Petrini *et al.*, 'Is a Quantum Biosensing Revolution Approaching? Perspectives in NV-Assisted Current and Thermal Biosensing in Living Cells', *Advanced Quantum Technologies*, vol. 3, no. 12, p. 2000066, 2020, doi: 10.1002/qute.202000066.

[16] R. Schirhagl, K. Chang, M. Loretz, and C. L. Degen, 'Nitrogen-vacancy centers in diamond: nanoscale sensors for physics and biology', *Annu Rev Phys Chem*, vol. 65, pp. 83–105, 2014, doi: 10.1146/annurev-physchem-040513-103659.

[17] E. Boto *et al.*, 'On the Potential of a New Generation of Magnetometers for MEG: A Beamformer Simulation Study', *PLOS ONE*, vol. 11, no. 8, p. e0157655, 8 2016, doi: 10.1371/journal.pone.0157655.

[18] T. Schönau *et al.*, 'A three-axis SQUID-based absolute vector magnetometer', *Review of Scientific Instruments*, vol. 86, no. 10, p. 105002, Oct. 2015, doi: 10.1063/1.4933386.

[19] Y. Tao, A. Eichler, T. Holzherr, and C. L. Degen, 'Ultrasensitive mechanical detection of magnetic moment using a commercial disk drive write head', *Nat Commun*, vol. 7, no. 1, p. 12714, Sep. 2016, doi: 10.1038/ncomms12714.

[20] J. J. Villegas-Saucillo, J. J. Díaz-Carmona, M. A. Escarola-Rosas, H. Vázquez-Leal, J. Martínez-Castillo, and A. L. Herrera-May, 'Measurements of the Magnetic Field Variations Related with the Size of V-Shaped Notches in Steel Pipes', *Applied Sciences*, vol. 11, no. 9, Art. no. 9, Jan. 2021, doi: 10.3390/app11093940.

[21] E. D. Narkhov, V. A. Sapunov, A. U. Denisov, and D. V. Savelyev, 'Novel quantum NMR magnetometer non-contact defectoscopy and monitoring technique for the safe exploitation of gas pipelines', Kuala Lumpur, Malaysia, Dec. 2014, pp. 649–658. doi: 10.2495/ESUS140571.

[22] D. B. Bucher, D. R. Glenn, H. Park, M. D. Lukin, and R. L. Walsworth, 'Hyperpolarization-Enhanced NMR Spectroscopy with Femtomole Sensitivity Using Quantum Defects in Diamond', *Phys. Rev. X*, vol. 10, no. 2, p. 021053, Jun. 2020, doi: 10.1103/PhysRevX.10.021053.

[23] J. S. Bennett *et al.*, 'Precision Magnetometers for Aerospace Applications: A Review', *Sensors*, vol. 21, no. 16, Art. no. 16, Jan. 2021, doi: 10.3390/s21165568.

[24] H. Korth *et al.*, 'Miniature atomic scalar magnetometer for space based on the rubidium isotope 87Rb', *Journal of Geophysical Research: Space Physics*, vol. 121, no. 8, pp. 7870–7880, 2016, doi: 10.1002/2016JA022389.

[25] A. Gruber, A. Dräbenstedt, C. Tietz, L. Fleury, J. Wrachtrup, and C. von Borczyskowski, 'Scanning Confocal Optical Microscopy and Magnetic Resonance on Single Defect Centers', *Science*, vol. 276, no. 5321, pp. 2012–2014, Jun. 1997, doi: 10.1126/science.276.5321.2012.

[26] R. Pirjola, A. Viljanen, A. Pulkkinen, and O. Amm, 'Space weather risk in power systems and pipelines', *Physics and Chemistry of the Earth, Part C: Solar, Terrestrial & Planetary Science*, vol. 25, no. 4, pp. 333–337, Jan. 2000, doi: 10.1016/S1464-1917(00)00027-1.

[27] N. Olsen, G. Hulot, and T. J. Sabaka, 'Measuring the Earth's Magnetic Field from Space: Concepts of Past, Present and Future Missions', *Space Sci Rev*, vol. 155, no. 1, pp. 65–93, Aug. 2010, doi: 10.1007/s11214-010-9676-5.

[28] R. C. Snare, 'A history of vector magnetometry. Measurement Techniques in Space Plasmas.', *American Geophysical Union*, vol. 1998, pp. 101–114.

[29] W. J. P. van Enckevort and E. H. Versteegen, 'Temperature dependence of optical absorption by the single-substitutional nitrogen donor in diamond', *J. Phys.: Condens. Matter*, vol. 4, no. 9, pp. 2361–2373, Mar. 1992, doi: 10.1088/0953-8984/4/9/028.

[30] C. (Carson A. Teale, 'Magnetometry with ensembles of nitrogen vacancy centers in bulk diamond', Thesis, Massachusetts Institute of Technology, 2015. Accessed: Dec. 12, 2021. [Online]. Available: https://dspace.mit.edu/handle/1721.1/103852

[31] G. Balasubramanian *et al.*, 'Ultralong spin coherence time in isotopically engineered diamond', *Nature Mater*, vol. 8, no. 5, pp. 383–387, May 2009, doi: 10.1038/nmat2420.

[32] P. Neumann *et al.*, 'Excited-state spectroscopy of single NV defects in diamond using optically detected magnetic resonance', *New J. Phys.*, vol. 11, no. 1, p. 013017, Jan. 2009, doi: 10.1088/1367-2630/11/1/013017.

[33] A. Gali, T. Simon, and J. E. Lowther, 'An ab initio study of local vibration modes of the nitrogen-vacancy center in diamond', *New J. Phys.*, vol. 13, no. 2, p. 025016, 2011, doi: 10.1088/1367-2630/13/2/025016.

[34] P. Deák, B. Aradi, M. Kaviani, T. Frauenheim, and A. Gali, 'Formation of NV centers in diamond: A theoretical study based on calculated transitions and migration of nitrogen and vacancy related defects', *Phys. Rev. B*, vol. 89, no. 7, p. 075203, Feb. 2014, doi: 10.1103/PhysRevB.89.075203.

[35] E. Bourgeois, M. Gulka, and M. Nesladek, 'Photoelectric Detection and Quantum Readout of Nitrogen-Vacancy Center Spin States in Diamond', *Advanced Optical Materials*, vol. 8, no. 12, p. 1902132, 2020, doi: 10.1002/adom.201902132.

[36] P. Siyushev *et al.*, 'Photoelectrical imaging and coherent spin-state readout of single nitrogen-vacancy centers in diamond', *Science*, vol. 363, no. 6428, pp. 728–731, Feb. 2019, doi: 10.1126/science.aav2789.

[37] T. Faust, J. Rieger, M. J. Seitner, J. P. Kotthaus, and E. M. Weig, 'Coherent control of a classical nanomechanical two-level system', *Nature Phys*, vol. 9, no. 8, pp. 485–488, Aug. 2013, doi: 10.1038/nphys2666.

[38] A. Wickenbrock *et al.*, 'Microwave-free magnetometry with nitrogen-vacancy centers in diamond', *Appl. Phys. Lett.*, vol. 109, no. 5, p. 053505, Aug. 2016, doi: 10.1063/1.4960171.

[39] H. Zheng *et al.*, 'Microwave-Free Vector Magnetometry with Nitrogen-Vacancy Centers along a Single Axis in Diamond', *Phys. Rev. Applied*, vol. 13, no. 4, p. 044023, Apr. 2020, doi: 10.1103/PhysRevApplied.13.044023.

[40] V. Ivády *et al.*, 'Photoluminescence at the ground-state level anticrossing of the nitrogen-vacancy center in diamond: A comprehensive study', *Phys. Rev. B*, vol. 103, no. 3, p. 035307, Jan. 2021, doi: 10.1103/PhysRevB.103.035307.

[41] H. Zheng *et al.*, 'Electrical readout microwave-free sensing with diamond', *arXiv:2201.01801 [physics, physics:quant-ph]*, Jan. 2022, Accessed: Jan. 15, 2022. [Online]. Available: http://arxiv.org/abs/2201.01801

[42] 'Nanodiamond', in *Carbon Materials and Nanotechnology*, John Wiley & Sons, Ltd, 2010, pp. 329–388. doi: 10.1002/9783527629602.ch5.

[43] A. Stacey, I. Aharonovich, S. Prawer, and J. E. Butler, 'Controlled synthesis of high quality micro/nano-diamonds by microwave plasma chemical vapor deposition', *Diamond & Related Materials*, vol. 1, no. 18, pp. 51–55, 2009, doi: 10.1016/j.diamond.2008.09.020.

[44] J. Meijer *et al.*, 'Generation of single color centers by focused nitrogen implantation', *Appl. Phys. Lett.*, vol. 87, no. 26, p. 261909, Dec. 2005, doi: 10.1063/1.2103389.

[45] J. Schwartz, S. Aloni, D. F. Ogletree, and T. Schenkel, 'Effects of low-energy electron irradiation on formation of nitrogen–vacancy centers in single-crystal diamond', *New J. Phys.*, vol. 14, no. 4, p. 043024, Apr. 2012, doi: 10.1088/1367-2630/14/4/043024.

[46] Z. Huang *et al.*, 'Diamond nitrogen-vacancy centers created by scanning focused helium ion beam and annealing', *Appl. Phys. Lett.*, vol. 103, no. 8, p. 081906, Aug. 2013, doi: 10.1063/1.4819339.

[47] J. Meijer *et al.*, 'Towards the implanting of ions and positioning of nanoparticles with nm spatial resolution', *Appl. Phys. A*, vol. 91, no. 4, pp. 567–571, 2008, doi: 10.1007/s00339-008-4515-1.

[48] S. D. Trofimov *et al.*, 'Spatially controlled fabrication of single NV centers in IIa HPHT diamond', *Opt. Mater. Express, OME*, vol. 10, no. 1, pp. 198–207, Jan. 2020, doi: 10.1364/OME.10.000198.

[49] J.-M. Cui *et al.*, 'Generation of Nitrogen-Vacancy Centers in Diamond with Ion Implantation', *Chinese Phys. Lett.*, vol. 29, no. 3, p. 036103, Mar. 2012, doi: 10.1088/0256-307X/29/3/036103.

[50] A. M. Edmonds *et al.*, 'Generation of nitrogen-vacancy ensembles in diamond for quantum sensors: Optimization and scalability of CVD processes'. arXiv, Apr. 03, 2020. doi: 10.48550/arXiv.2004.01746.

[51] 'Imaging in Resist: Standing Waves and Swing Curves', in *Fundamental Principles of Optical Lithography*, John Wiley & Sons, Ltd, 2007, pp. 129–190. doi: 10.1002/9780470723876.ch4.

[52] U. G. Lee, W.-B. Kim, D. H. Han, and H. S. Chung, 'A Modified Equation for Thickness of the Film Fabricated by Spin Coating', *Symmetry*, vol. 11, no. 9, Art. no. 9, Sep. 2019, doi: 10.3390/sym11091183.

[53] N. Atthi, O.-U. Nimittrakoolchai, W. Jeamsaksiri, S. Supothina, C. Hruanun, and A. Poyai, 'Study of optimization condition for spin coating of the photoresist film on rectangular substrate by Taguchi design of an experiment', *Songklanakarin Journal of Science and Technology*, vol. 31, no. 3, pp. 331–335, 2009.

[54] 'Conventional Resists: Exposure and Bake Chemistry', in *Fundamental Principles of Optical Lithography*, John Wiley & Sons, Ltd, 2007, pp. 191–222. doi: 10.1002/9780470723876.ch5.

[55] 'Photoresist Development', in *Fundamental Principles of Optical Lithography*, John Wiley & Sons, Ltd, 2007, pp. 257–296. doi: 10.1002/9780470723876.ch7.

[56] Kiyotaka Wasa, *Handbook of Sputter Deposition Technology, Fundamentals and Applications for Functional Thin Films, Nano-Materials and MEMS*, October 26, 2012.

[57] J. Koskinen, '4.02 - Cathodic-Arc and Thermal-Evaporation Deposition', in *Comprehensive Materials Processing*, S. Hashmi, G. F. Batalha, C. J. Van Tyne, and B. Yilbas, Eds. Oxford: Elsevier, 2014, pp. 3–55. doi: 10.1016/B978-0-08-096532-1.00409-X.

[58] 'Introduction to Semiconductor Lithography', in *Fundamental Principles of Optical Lithography*, John Wiley & Sons, Ltd, 2007, pp. 1–28. doi: 10.1002/9780470723876.ch1.

[59] ‘OpenSCAD’. https://openscad.org (accessed Jan. 31, 2022).

[60] ‘Team OSCAR-QUBE awarded the Hans von Muldau Team Award at IAC’. https://www.esa.int/Education/Orbit_Your_Thesis/Team_OSCAR-QUBE_awarded_the_Hans_von_Muldau_Team_Award_at_IAC (accessed Mar. 22, 2022).

[61] ‘ESA selects payloads for Ariane 6 first flight’. https://www.esa.int/Enabling_Support/Space_Transportation/Ariane/ESA_selects_payloads_for_Ariane_6_first_flight (accessed Mar. 22, 2022).

4. Chapter 4 - Pulsed photoelectric coherent manipulation and detection of N-V center spins in diamond

Authors contribution: I developed the system control software and data acquisition algorithm. Also, the main idea of the MW triggering on which is the paper based is taken up from the patent US20170328965A1 of which I am the first author. This part relates to the microwave triggering that allows the high contrast spin readout. This work focuses on advancing the PDMR readout technique towards single NV centre readout and demonstrating that it is viable for pulsed measurements allowing the spin manipulation. This work is setting an important baseline for the next more advanced research and applications, such as quantum NMR or quantum computing by addressing individual qubits electrically, as well as step towards miniaturization.

PHYSICAL REVIEW APPLIED 7, 044032 (2017)

Pulsed Photoelectric Coherent Manipulation and Detection of N-V Center Spins in Diamond

Michal Gulka,[1,2] Emilie Bourgeois,[1,3] **Jaroslav Hruby**,[1] Petr Siyushev,[4] Georg Wachter,[5] Friedrich Aumayr,[6] Philip R. Hemmer,[7] Adam Gali,[8,9] Fedor Jelezko,[4] Michael Trupke,[5] and Milos Nesladek[1,3,*]

[1] Institute for Materials Research (IMO), Hasselt University, Wetenschapspark 1, B-3590 Diepenbeek, Belgium

[2] Faculty of Biomedical Engineering, Czech Technical University in Prague, Sítna sq. 3105, 27201 Kladno, Czech Republic

[3] IMOMEC division, IMEC, Wetenschapspark 1, B-3590 Diepenbeek, Belgium

[4] Institute for Quantum Optics and IQST, Ulm University, Albert-Einstein-Allee 11, D-89081 Ulm, Germany

[5] Vienna Center for Quantum Science and Technology, Atominstitut, TU Wien, 1020 Vienna, Austria

[6] Institute of Applied Physics, TU Wien, Wiedner Hauptstrasse 8-10, 1040 Vienna, Austria

[7] Department of Electrical and Computer Engineering, Texas A&M University, College Station, Texas 77843, USA

[8] Institute for Solid State Physics and Optics, Wigner Research Centre for Physics, Hungarian Academy of Sciences, PO Box 49, H-1525 Budapest, Hungary

[9] Department of Atomic Physics, Budapest University of Technology and Economics, Budafoki út 8, H-1111 Budapest, Hungary

(Received 10 November 2016; revised manuscript received 17 February 2017; published 28 April 2017; corrected 8 June 2017)

Abstract:

We demonstrate hybrid photoelectric pulse protocols for reading the spin states of nitrogen-vacancy (N-V) centers in diamond, compatible with coherent spin control and performed on shallow nitrogen-implanted electronic grade diamond. The measurements are carried out on spin ensembles from 1000 to just five N-V centers as a first step towards the fabrication of scalable photoelectric quantum chips. Specific microwave protocols are developed that suppress background photocurrent related to ionization of N_S^0 defects and provide a high contrast and SNR. The technique is demonstrated on Rabi and Ramsey sequences.

DOI: 10.1103/PhysRevApplied.7.044032

I. INTRODUCTION

Hybrid quantum detection approaches are considered very promising in the realization of scalable systems for quantum computation [1]. Here we demonstrate coherent manipulation and photoelectric readout of nitrogen vacancy (N-V) spin states in diamond as a basic building block for scalable miniaturized electric quantum devices [2]. The developed readout protocols are based on the N-V center two-photon ionization. Further on, by providing microwave (MW) on-resonance-triggering for a lock-in amplification, the photocurrent induced by the photoionization of single substitutional nitrogen N_S^0 (P1 defect) is subtracted from the detected signal. The presented technique allows for high readout contrast—the offset only due to the electronic noise—and signal readout up to high frequencies of approximately 20 MHz. The high sensitivity of the proposed protocols allows us to read the spin state of approximately five N-V centers.

N-V solid-state qubits in diamond are among the most studied quantum systems today due to their record spin coherence time at room temperature [3] and are used for quantum sensing applications (e.g., magnetometry [4], thermometry [5], or single-spin nano-magnetic-resonance imaging [6]). The optically detected magnetic resonance (ODMR) method [7] used as a major technique for N-V center readout in diamond has important limitations in the scalability and does not provide integration with electronic chip. Recently, we have introduced the photoelectrically detected magnetic resonance (PDMR) technique [8] for reading out the electron spin state of negatively charged N-V center in diamond. This method provides a vast enhancement of over 2.5 orders of magnitude in detection rates compared to ODMR measured in similar experimental conditions (see Ref. [9] for details). The technique is potentially applicable to other materials such as SiC [10], GaN, or AlN [11]. Although we have demonstrated the principle of this method, it was used only for continuous wave (CW) readout of the j0i and j1i spin states of N-V ensembles in lab-grown chemical vapor deposition (CVD) or high pressure high temperature (HPHT) diamonds [8]. In order to use the advantages of the PDMR technique in quantum sensing and computational schemes, it is necessary to demonstrate that the photoelectric readout is compatible with the quantum control of individual N-V electron spins. The photoelectric detection of Rabi oscillations was demonstrated, for example,

in two-level exciton systems in quantum dots [12,13] or in silicon [14–16]. Here, we perform coherent operations with PDMR on spin ensembles of just a few (approximately five) N-V centers by designing specific readout sequences. We demonstrate these protocols by performing Rabi and Ramsey measurements on shallow N-V ensembles implanted in electronic grade diamond that is—unlike bulk crystals—a material suitable for future quantum devices. The proposed method leads to a significant suppression of background photocurrents, which is one of the main limiting factors in achieving PDMR on single N-V sites [8,17] and considerably increased signal-to-noise ratio (SNR) compared to CW PDMR measurements [8,9].In this way, we can experimentally verify the SNRs that were previously only theoretically predicted [18].

II. EXPERIMENTAL SETUP AND PRINCIPLE

Figure 1(a) depicts the hybrid photoelectric quantum chip used in our measurements. Type-II a single-crystal electronic grade diamond is implanted with 8-keV $^{14}N^{4+}$ ions and annealed at 900°C to create ensembles of shallow N-V centers (depth 12 ± 4 nm). The implantation fluence is varied to create a total of five regions with different N-V densities (from approximately 15 to 10^4 μm^{-2}). The sample is equipped with coplanar Ti-Au electrodes with a 50-μm gap and mounted on a circuit board to enable MW excitation and photocurrent readout. The MW is provided using two printed antennas [19]. Green laser illumination induces the two-photon ionization of N-V centers from the $|0\rangle$ and $|\pm1\rangle$ $^3A_2$ NV ground-state (GS) spin manifolds to the conduction band (CB) [Fig.1(b)] [20,21]. A dc electric field is applied in between the electrodes, and the photocurrent is read out by a lock-in amplification after sensitive preamplification (see Ref. [22] for more details on the experimental setup). The magnetic resonance (MR) contrast in the detected photocurrent is obtained under resonant microwave excitation (2.87 GHz) inducing transitions from the j0i to the j1i spin sublevels of the N-V ground state [23]. Electrons photoexcited from the j1i GS manifold have a nonzero probability of undergoing shelving transitions from the N-V excited state to the metastable ^1E state [24–26]. During the time in which the j1i spin electron is stored in the metastable singlet state (approximately 220-ns lifetime) [8,27,28], it is protected from photoionization. This electron shelving leads to a reduction of the overall photocurrent and, thus, to a minimum in the photocurrent signal at the resonant MW frequency [8]. So far, the photocurrent signal from N-V centers is read out either by the lock-in technique referenced to the laser-pulse frequency [8,9] or by detecting the dc photocurrent after implementing a laser readout pulse [18]. Both proposed methods suffer from a background photocurrent induced by the photoionization of other defects such as substitutional nitrogen (N_S^0) [9], which reduces the detected MR contrast, preventing the application of PDMR for single N-V detection. Here we perform PDMR readout using pulse sequences and referencing the lock-in signal to the MW pulses. In this way, we detect only the proportion of the photocurrent affected by the MW field, i.e., variations in the photocurrent signal related to $|0\rangle \leftrightarrow |\pm1\rangle$ transitions. Therefore, we obtain a resonance spectrum with a positive contrast defined as $(S_{max} - S_{min}) / (S_{max} + S_{min})$, where S is the ac signal detected by the lock-in amplifier, and its maximum is equivalent to approximately 30% (or less) of the total dc off-resonant N-V photocurrent. Because the ac off-resonant photocurrent is zero, the detection contrast between off- and on-resonant MW frequencies is approximately 100%

and is reduced only by the detected noise. As an additional advantage, the background signal from defects other than N-V is filtered out when scanning the MW frequency around the N-V resonant line.

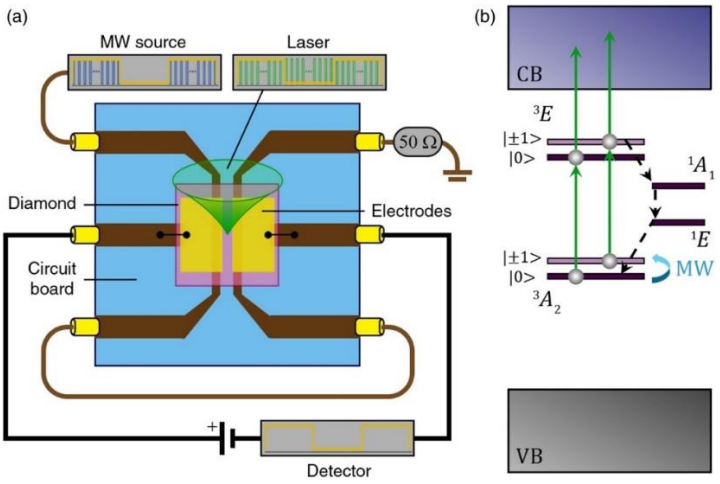

FIG. 1. (a) Schematics of the setup used for pulsed PDMR, showing a type-IIa nitrogen implanted diamond mounted on the circuit board. (b) Simplified electronic energy-level scheme of the NV center showing two photon ionization of the electron from the GS to the CB. Spin-selective decay through metastable ^1E state enables the PDMR (MW, microwave; VB, valence band; CB, conduction band).

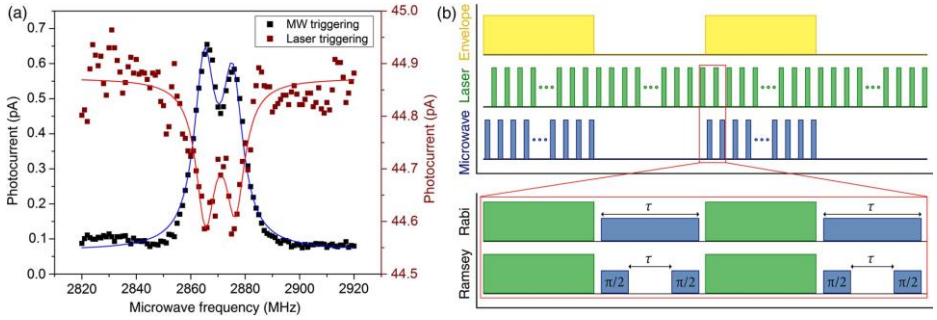

FIG. 2. (a) Comparison of the laser- (dark red dots) and MW- (black dots) triggering CW PDMR method in the case of a fast measurement (single PDMR scan). Data were measured on a N-V ensemble using similar experimental conditions and fitted. (b) PDMR pulse trains that encode high-frequency pulse sequences (Rabi, Ramsey) into a low-frequency envelope used as a reference for lock-in detection

The use of MW triggering sequences gives significantly lower electronic noise that is identified to originate from the coupling of MW irradiation to photocurrent readout circuits. To quantify the benefit of the MW-triggering scheme, we measure CW PDMR spectra at the same position using both approaches (lock-in amplifier referenced to the laser and MW pulse frequency, with similar experimental conditions), and we compare the SNRs for both cases. The photocurrent signal S is determined from a fit of the PDMR spectrum. The noise N is calculated as the standard deviation of the off-resonant (blank) photocurrent signal. At the highly implanted region of the sample (corresponding to approximately 1000 N-Vs in focus of the objective), the MW triggering yields a 7.4 times improvement in the SNR. The illustrative spectra are shown inFig.2(a). The vast improvement in the SNR is visible even for a very fast measurement.

To achieve coherent manipulation of spins with photoelectric readout, we encode single-pulse sequences into a low-frequency envelope [Fig. 2(b)]. A continuous series of consecutive laser pulses is used in which each pulse serves for the spin initialization and spin-state readout. Bursts of spin manipulation MW pulses time shifted with respect to laser pulses are added to encode any arbitrary sequence. A MW trigger pulse marks the start of the pulse burst during which the low-frequency-modulated photocurrent signal is measured. In the off period of the duty cycle, a train of spin-polarization laser pulses maintains the occupation of the $|0\rangle$ state. We explore envelope frequencies from 30 Hz up to 1 kHz, tuned to obtain the highest SNR. In principle, this method enables us to encode any pulse sequence into the low-frequency envelope. Here we demonstrate this technique on Rabi and Ramsey measurements, which are key sequences for quantum measurements [29].

III. EXPERIMENTAL RESULTS AND DISCUSSION

Rabi measurements (see Fig. 3) are performed first in the region of the sample with approximately 1000 N-V centers in the focus of the objective (region R1 [22]). Static magnetic field is applied perpendicularly to the $<100>$ diamond plane to split the $|\pm1\rangle$ spin levels. We then vary the duration of resonant MW pulses at constant power [see Fig. 2(b)] to determine the duration of the π pulse.

As expected, the Rabi frequencies calculated [22] from the fit [30] of these measurements depend linearly on the square root of the MW power (Fig. 3 inset). The presented measurement proves the possibility of coherent spin readout using the MW-triggered PDMR envelope pulse scheme. The measured Rabi oscillations for MW peak power of 3.2 W are plotted in Fig. 3, yielding a Rabi decay time of approximately 490 ns on the sample area with the highest $^{14}N^{4+}$ ion implantation fluency.

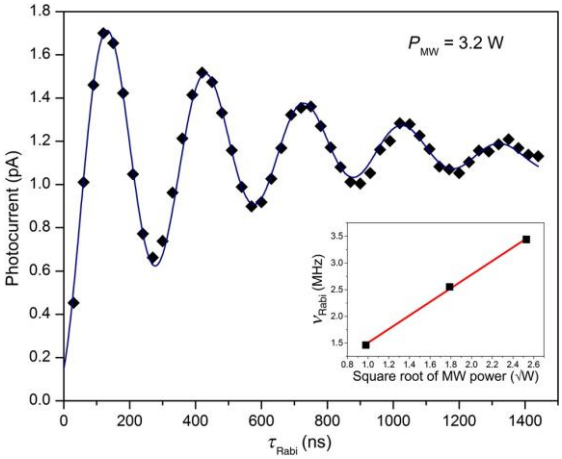

FIG. 3. Photoelectric detection of Rabi oscillations using the envelope technique with MW triggering. The black scatter points are the experimental data for MW power of 3.2 W, and the blue line is fitted assuming an exponential damping. Inset shows the dependence of the frequency of Rabi oscillations with respect to the square root of the applied microwave power (red line is the result of the linear fit).

To show the applicability of the designed PDMR protocols, we demonstrate functional Ramsey fringe pulse sequences [Fig. 2(b)] employed to characterize the N-V center free-spin dynamics. The measurement is performed at the same position as the Rabi experiment. By varying the free-precession time τ_{Ram}, we observe a decay curve consisting of the superposition of three cosine functions with different frequencies δ_i (for conditions, see Ref. [22]). Each frequency corresponds to the detuning of the applied MW frequency from one of the hyperfine ^{14}N transitions such that $\delta 1 = \nu_{Ram} - 2.2$ MHz, $\delta 2 = \nu_{Ram}$, and $\delta 3 = \nu_{Ram} + 2.2$MHz [31,32], where ν_{Ram} is the Ramsey frequency. The measurement is performed for different detunings δ_2 (4, 8, 12, 16, 20MHz) from the central resonant frequency. The results are shown in Fig. 4. As expected, we observe a linear dependence of the Ramsey frequency to the detuning values (Fig. 4 inset). The average dephasing time T_2 for all measurements is approximately 41 ns using single exponential decay fitting [33] or approximately 66 ns using Gaussian decay fitting of the data [34]. This short value reflects the decoherent interactions of N-V ensembles on the sample area overimplantedwith$^{14}N^{+}$ ions(regionR1[22]). The main source of dephasing is the bath of paramagnetic substitutional nitrogen impurities (N_S^0 centers), although^{14}Nnuclearspins can also contribute [27,35,36]. Despite the very fast decay, our technique enables us to read out Ramsey fringes at high frequency of 20 MHz with a very high contrast, confirming the ability of MW-referenced PDMR to measure samples with very short T_2 times with high SNR. By the proposed technique, Hahn echo or more complex sequences such as the Carr-Purcell-Meiboom-Gill pulse train can be encoded into the envelope carrier. The base value of the MW-triggered photocurrent is inversely proportional to the detuning frequency, reflecting the occupation of spin states integrated over the statistical weight of the $|0\rangle$ and $|-1\rangle$ manifolds.

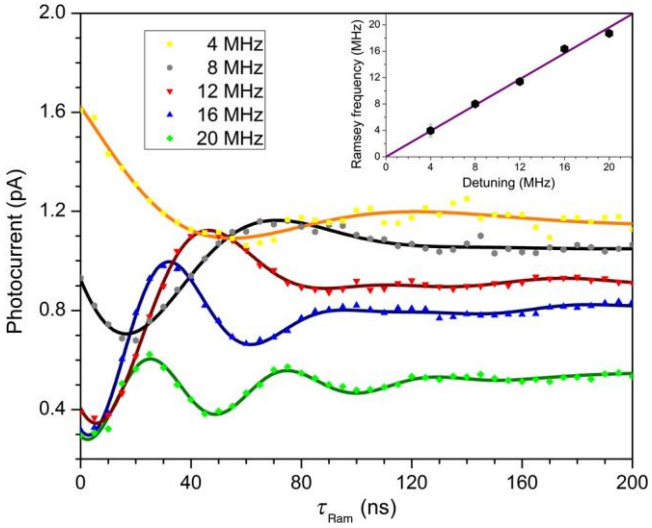

FIG. 4. Photoelectric detection of Ramsey fringes for different detuning of MW excitation frequency from the N-V resonant frequency. The scatter points are the experimental data fitted considering a single exponential decay (continuous lines). Inset shows the linear dependence of Ramsey frequency to the MW detuning (purple line is the result of the linear fit).

An important milestone for the PDMR technique is to reach coherent manipulation of single N-V spins. While our recent studies [8,9] and other published work [18] demonstrate PDMR on N-V ensembles, the photoelectric readout of single spins is not achieved yet. To downscale the number of N-V centers, we use the N-implanted electronic grade diamond containing five regions of descending N-V densities corresponding to ensembles from 1000 to approximately five N-V centers in focus of the objective. The number of N-V centers is calibrated from photoluminescence counts of a single N-V obtained under the same conditions.

First, we measure the total photocurrent signal upon downscaling the N-V ensembles [see Fig. 5(a) inset]. For this, we use the lock-in technique referenced to a pulsed laser without the MW field applied. These data can be fitted using a sublinear function. We speculate that this is due to a reduction of recombination lifetime in the highly implanted region. From the fit, we experimentally determine the total photocurrent resulting from the ionization of a single N-V to be approximately 1.0 pA for an electric field of 2×10^4 V cm-1 similar to predictions presented in Refs. [8,18]. However, the measured photocurrent is a sum of the N-V–related photocurrent and of the background signal originating mainly from single substitutional nitrogen N_{S0} ionization. We estimate that at these power conditions, approximately 75% of the signal comes from two-photon ionization of the N-V centers [9]. Thus, we experimentally verify the predictions of the photocurrent value expected for single N-V centers in given electric field conditions by measurements on a small number of N-V centers (approximately five) downscaled by at least approximately 10^4 times compared to previous measurements [18]. Figure 5(a) shows pulse PDMR

spectra obtained for decreasing numbers of N-V centers in the focus of the objective. The data are fitted using a two-peak Gaussian function [36] averaging over the central and hyperfine MR lines and a noise background offset is subtracted from the spectra. The estimated value of the single N-V photocurrent at resonance frequency averaged from all four measurements is approximately 2 fA. This value is approximately 50 times lower than the photocurrent expected for a single N-V in the used conditions based on CW light-triggered measurements (see above) and considering a CW PDMR contrast of approximately 10% [9]. This decrease is attributed to several factors such as the use of the duty cycle (resulting in a reduced effective MW and laser power) and the loss of the contrast during the laser readout pulse (since the laser pulse is used for both readout and initialization of the N-Vs).

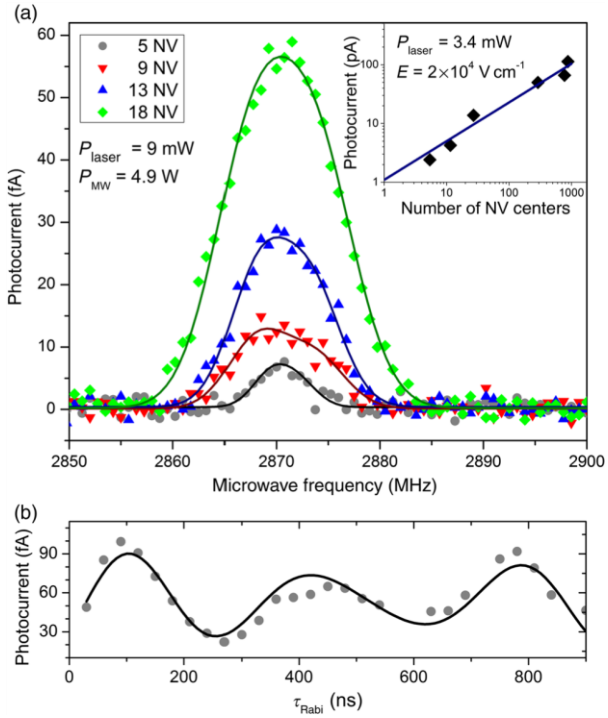

FIG. 5. (a) Photocurrent spectra measured on small spin ensembles down to five N-Vs using a sequence consisting of a short laser pulse followed by a MW π pulse. The experimental data are fitted with two Gaussian functions. For comparison, the inset shows the total photocurrent from different numbers of N-V centers measured with only laser excitation (blue line is the result of the fit). (b) Rabi measurement on five N-V centers at MW power of 3W. The fit of the data takes into account the beating originating from the coupling to the nitrogen nuclear spins with frequency of 2.2 MHz, similar to the fitting of Ramsey data in Fig. 4.

By using pulse PDMR protocols with MW triggering, i.e., without any contribution of background photocurrent originating from N_{S0} photoionization, we demonstrate Rabi measurement on the sample region with the lowest implantation density corresponding to five N-Vs in the focus [Fig. 5(b)]. The presented results show the applicability of the scheme for measurements of just very few individual N-V centers.

To explore the limitations of the pulsed PDMR method, we concentrate on the comparison of the theoretical and experimental values of the noise level. The main components of the total noise N_{rms} come from the shot noise generated by the photocurrent $I_{SN}(rms)$ [37,38], input noise of the preamplifier $I_{preamp}(rms)$, and input noise of the lock-in amplifier $I_{lock\text{-}in}(rms)$ expressed as

$$N_{\mathrm{rms}} = [\delta I_{\mathrm{SN}}(\mathrm{rms}) + \delta I_{\mathrm{preamp}}(\mathrm{rms}) + \delta I_{\mathrm{lock\text{-}in}}(\mathrm{rms})]\sqrt{\Delta f},$$

where Δf is the bandwidth of detection electronics. Thanks to the lock-in amplifier detection, one is able to reduce the noise significantly, since in this case, Δf corresponds to the equivalent noise bandwidth (ENBW) determined by the lock-in amplifier time constant. The ENBW can be then very narrow, thus, increasing the SNR by rejecting the white noise [37]. The total noise is then calculated as

$$N_{\mathrm{rms}} = [\sqrt{e \cdot I} + \delta I_{\mathrm{preamp}}(\mathrm{rms})] + \delta I_{\mathrm{lock\text{-}in}}(\mathrm{rms}) \cdot \sqrt{\mathrm{ENBW}},$$

where e is the elementary charge, and I is the measured photocurrent. Considering the specifications for our preamplifier and lock-in amplifier, we calculate for the CW technique $N_{rms}/\sqrt{ENBW}$ of approximately 60.4 fA $Hz^{-1/2}$ with a dominant noise originating from the preamplifier (approximately 60 fA $Hz^{-1/2}$ at a given frequency) compared to the measured value of approximately 83.7 fA $Hz^{-1/2}$ for 1000 N-Vs in the focus. We speculate that this difference (23.3 fA $Hz^{-1/2}$) between the experimental and predicted noise is due to the photocurrent noise correlated to MW cross talk occurring on the chip level. This type of crosstalk noise should be significantly reduced for the pulsed measurements where the laser readout pulse is decoupled from the MW pulse. To confirm this, we determine the correlated noise for the experiment in Fig. 5(a) performed using the pulsed protocols. In this configuration, the correlated noise is reduced to 4.4 fA $Hz^{-1/2}$. The correlated noise compared to the optically-triggered CW PDMR (212.5 fA $Hz^{-1/2}$) is, therefore, reduced by a factor of 48. The shot noise for the MW-triggered PDMR is approximately 0.126 fA $Hz^{-1/2}$ calculated for a single N-V spin photocurrent (considering a differential current between the spin $|0\rangle$ and $|\pm1\rangle$ states of 100 fA).

IV. CONCLUSION

To conclude, we demonstrate pulsed coherent readout techniques for small ensembles down to five individual N-V centers in shallow implanted electronic grade diamond, which is the material used for relevant quantum applications. We develop MW-referenced pulse sequences enabling us to eliminate the N_S^0-related background photocurrents, which was previously identified as a main obstacle to using the PDMR technique for readout of single N-V spins. In this way, together with the lock-in readout technique, we reach a signal detection contrast close to 100%. A significant reduction of the correlated noise compared to the CW technique makes possible an order of magnitude enhancement of the SNR. We develop hybrid Rabi and Ramsey photoelectric coherent spin manipulation protocols encoding high-frequency MW and laser-pulse sequences into a low-frequency envelope. A further enhancement in the SNR can be achieved by designing nanoscopic electrodes for operating efficiently single N-Vs with high photoelectron gain [8,9]. The ability to read out and control the spin state by the hybrid photocurrent method presented here demonstrates perspectives on progressing towards a compact and scalable single-spin device.

ACKNOWLEDGMENTS

Support from the EU (FP7 project DIADEMS, Grant No. 611143), Grant Agency of the Czech Republic (Project No. 16-16336S), Czech-Flemish bilateral Project No. BOF15BL08, and Flemish Scientific Research Project (FWO) No. G0E7417N are acknowledged. We thank Professor Dmitry Budker from Johannes Gutenberg University, Mainz and from University of California, Berkeley for valuable discussions.

[1] S. Pirandola and S. L. Braunstein, Physics: Unite to build a quantum Internet, Nature (London) 532, 169 (2016).

[2] A. Morello, J. J. Pla, F. A. Zwanenburg, K. W. Chan, K. Y. Tan, H. Huebl, M. Möttönen, C. D. Nugroho, C. Yang, J. A. van Donkelaar, A. D. C. Alves, D. N. Jamieson, C. C. Escott, L. C. L. Hollenberg, R. G. Clark, and A. S. Dzurak, Single-shot readout of an electron spin in silicon, Nature (London) 467, 687 (2010).

[3] G. Balasubramanian, P. Neumann, D. Twitchen, M. Markham, R. Kolesov, N. Mizuochi, J. Isoya, J. Achard, J. Beck, J. Tissler, V. Jacques, P. R. Hemmer, F. Jelezko, and J. Wrachtrup, Ultralong spin coherence time in isotopically engineered diamond, Nat. Mater. 8, 383 (2009).

[4] P. Maletinsky, S. Hong, M. S. Grinolds, B. Hausmann, M. D. Lukin, R. L. Walsworth, M. Loncar, and A. Yacoby, A robust scanning diamond sensor for nanoscale imaging with single nitrogen-vacancy centres, Nat. Nanotechnol. 7, 320 (2012).

[5] P. Neumann, I. Jakobi, F. Dolde, C. Burk, R. Reuter, G. Waldherr, J. Honert, T. Wolf, A. Brunner, and J. H. Shim, High-precision nanoscale temperature sensing using single defects in diamond, Nano Lett. 13, 6 (2013).

[6] T. Staudacher, F. Shi, S. Pezzagna, J. Meijer, J. Du, C. A. Meriles, F. Reinhard, and J. Wrachtrup, Nuclear magnetic resonance spectroscopy on a ð5-nanometerÞ^3 sample volume, Science 339, 561 (2013).

[7] A. Gruber, A. Dräbenstedt, C. Tietz, L. Fleury, J. Wrachtrup, and C. von Borczyskowski, Scanning confocal optical microscopy and magnetic resonance on single defect centers, Science 276, 2012 (1997).

[8] E. Bourgeois, A. Jarmola, P. Siyushev, M. Gulka, J. Hruby, F. Jelezko, D. Budker, and M. Nesladek, Photoelectric detection of electron spin resonance of nitrogen-vacancy centres in diamond, Nat. Commun. 6, 8577 (2015).

[9] E. Bourgeois, E. Londero, K. Buczak, J. Hruby, M. Gulka, Y. Balasubramaniam, G. Wachter, J. Stursa, K. Dobes, F. Aumayr, M. Trupke, A. Gali, and M. Nesladek, Enhanced photoelectric detection of NV magnetic resonances in diamond under dual-beam excitation, Phys. Rev. B 95, 041402(R) (2017).

[10] W. F. Koehl, B. B. Buckley, F. J. Heremans, G. Calusine, and D. D. Awschalom, Room temperature coherent control of defect spin qubits in silicon carbide, Nature (London) 479, 84 (2011).

[11] H. Seo, H. M. Govoni, and G. Galli, Design of defect spins in piezoelectric aluminum nitride for solid-state hybrid quantum technologies, Sci. Rep. 6, 20803 (2016).

[12] A. Zrenner, E. Beham, S. Stufler, F. Findeis, M. Bichler, and G. Abstreiter, Coherent properties of a two-level system based on a quantum-dot photodiode, Nature (London) 418, 612 (2002).

[13] Y. Wu, I. M. Piper, M. Ediger, P. Brereton, E. R. Schmidgall, P. R. Eastham, M. Hugues, M. Hopkinson, and R. T.
Phillips, Population Inversion in a Single InGaAs Quantum Dot Using the Method of Adiabatic Rapid Passage, Phys. Rev. Lett. 106, 067401 (2011).

[14] F. Hoehne, L. Dreher, M. Suckert, D. P. Franke, M. Stutzmann, and Martin S. Brandt, Time constants of spin-dependent recombination processes, Phys. Rev. B 88, 155301 (2013).

[15] F. Hoehne, L. Dreher, D. P. Franke, M. Stutzmann, L. S. Vlasenko, K. M. Itoh, and M. S. Brandt, Submillisecond Hyperpolarization of Nuclear Spins in Silicon, Phys. Rev. Lett. 114, 117602 (2015).

[16] F. M. Hrubesch, G. Braunbeck, A. Voss, M. Stutzmann, and M. S. Brandt, Broadband electrically detected magnetic resonance using adiabatic pulses, J. Magn. Reson. 254, 62 (2015).

[17] J. Chen, S. Lourette, K. Rezai, T. Hoelzer, M. Lake, M. Nesladek, L.-S. Bouchard, P. Hemmer, and D. Budker, Optical quenching and recovery of photoconductivity in single-crystaldiamond,Appl.Phys.Lett.110,011108(2017).

[18] F. M.Hrubesch,G.Braunbeck,M.Stutzmann,F.Reinhard,and M. S. Brandt, Efficient Electrical Spin Readout of NV^-CentersinDiamond,Phys.Rev.Lett.118,037601(2017).

[19] M. Mrózek, J. Mlynarczyk, D. S. Rudnicki, and W. Gawlik, Circularly polarized microwaves for magnetic resonance study in the GHz range:

Application to nitrogen-vacancy in diamonds, Appl. Phys. Lett. 107, 013505 (2015).

[20] P. Siyushev, H. Pinto, M. Vörös, A. Gali, F. Jelezko, and J. Wrachtrup, Optically Controlled Switching of the Charge State of a Single Nitrogen-Vacancy Center in Diamond at Cryogenic Temperatures, Phys. Rev. Lett. 110, 167402 (2013).

[21] K. Jensen, V. M. Acosta, A. Jarmola, and D. Budker, Light narrowing of magnetic resonances in ensembles of nitrogenvacancy centers in diamond, Phys. Rev. B 87, 014115 (2013).

[22] See Supplemental Material at http://link.aps.org/supplemental/10.1103/PhysRevApplied.7.044032 for additional information about methods, materials and data fitting.

[23] G. Balasubramanian, I. Y. Chan, R. Kolesov, M. Al-Hmoud, J. Tisler, C. Shin, C. Kim, A. Wojcik, P. R. Hemmer, A. Krueger, T. Hanke, A. Leitenstorfer, R. Bratschitsch, F. Jelezko, and J. Wrachtrup, Nanoscale imaging magnetometry with diamond spins under ambient conditions, Nature (London) 455, 648 (2008).

[24] F. Jelezko and J. Wrachtrup, Single defect centres in diamond: A review, Phys. Status Solidi A 203, 3207 (2006). [25] M. W. Doherty, N. B. Manson, P. Delaney, F. Jelezko, J. Wrachtrup, and L. C. L. Hollenberg, The nitrogen-vacancy colour centre in diamond, Phys. Rep. 528, 1 (2013).

[26] L. J. Rogers, M. W. Doherty, M. S. J. Barson, S. Onoda, T. Ohshima, and N. B. Manson, Singlet levels of the NV^- centre in diamond, New J. Phys. 17, 013048 (2015).

[27] V. M. Acosta, A. Jarmola, E. Bauch, and D. Budker, Optical properties of the nitrogen-vacancy singlet levels in diamond, Phys. Rev. B 82, 201202(R) (2010).

[28] J.-P. Tetienne, L. Rondin, P. Spinicelli, M. Chipaux, T. Debuisschert, J.-F. Roch, and V. Jacques, Magnetic-fielddependent photodynamics of single NV defects in diamond:
an application to qualitative all-optical magnetic imaging, New J. Phys. 14, 103033 (2012).

[29] T. Wolf, P. Neumann, K. Nakamura, H. Sumiya, T. Ohshima, J. Isoya, and J. Wrachtrup, Subpicotesla Diamond Magnetometry, Phys. Rev. X 5, 041001 (2015).

[30] R. Hanson, O. Gywat, and D. D. Awschalom, Roomtemperature manipulation and decoherence of a single spin in diamond, Phys. Rev. B 74, 161203(R) (2006).

[31] L. Childress, M. V. Gurudev Dutt, J. M. Taylor, A. S. Zibrov, F. Jelezko, J. Wrachtrup, P. R. Hemmer, and M. D. Lukin, Coherent dynamics of coupled electron and nuclear spin qubits in diamond, Science 314, 281 (2006).

[32] H. Xin, L. Gang-Qin, X. Zhang-Cheng, and P. Xin-Yu, Influence of microwave detuning on Ramsey fringes of a single nitrogen vacancy center spin in diamond, Chin. Phys. Lett. 29, 2 (2012).

[33] C. Grèzes, Towards a Spin-Ensemble Quantum Memory for Superconducting Qubits (Springer International Publishing, New York, 2015).
[34] G.-Q. Liu, X.-Y. Pan, Z.-F. Jiang, N. Zhao, and R.-B. Liu, Controllable effects of quantum fluctuations on spin freeinduction decay at room temperature, Sci. Rep. 2, 432 (2012).
[35] J. M. Taylor, P. Cappellaro, L. Childress, L. Jiang, D. Budker, P. R. Hemmer, A. Yacoby, R. Walsworth, and M. D. Lukin, High-sensitivity diamond magnetometer with nanoscale resolution, Nat. Phys. 4, 810 (2008).
[36] V. R. Horowitz, B. J. Alemán, D. J. Christle, A. N. Cleland, and D. D. Awschalom, Electron spin resonance of nitrogenvacancy centers in optically trapped nanodiamonds, Proc. Natl. Acad. Sci. U.S.A. 109, 13493 (2012).
[37] A. Mandelis, Signal-to-noise ratio in lock-in amplifier synchronous detection: A generalized communications systems approach with applications to frequency, time, and hybrid (rate window) photothermal measurements, Rev. Sci. Instrum. 65, 3309 (1994).
[38] R. Pettai, Noise in Receiving Systems (Wiley-Interscience, New York, 1984).

5. Chapter 5 - Magnetic field sensitivity of the photoelectrically read nitrogen-vacancy centres in diamond

Authors contribution: I am the main author of this work and I developed software, electrode fabrication process, realized measurements, data processing, and writing of the paper. This work is exploring the use of a laser wavelengths that only stimulate NV centres and do not lead to photoionization of additional defects (namely P1 substitutional nitrogen) which can contribute to the photocurrent signal and are excited by green 532nm wavelength. Whereas yellow-green 561nm wavelength should theoretically only excite the NV centres. Therefore, this work is positioned within my PhD work on finding optimal ways to realize PDMR readout and advancing this technology further.

Magnetic field sensitivity of the photoelectrically read nitrogen-vacancy centres in diamond

Jaroslav Hruby[1,2], Michal Gulka[1,3], Massimo Mongillo[4], Iuiliana P. Radu[4], Emilie Bourgeois[1,2] and Milos Nesladek[1,2]

[1]Institute for Materials Research (IMO), Hasselt University, Wetenschapspark 1, B-3590 Diepenbeek, Belgium.

[2]IMOMEC Division, IMEC, Wetenschapspark 1, B-3590 Diepenbeek, Belgium.

[3]Institute of Organic Chemistry and Biochemistry, Czech Academy of Sciences, 166 10 Prague, Czech Republic.

[4]Imec, Kapeldreef 75, Leuven, B-3001, Belgium

Abstract:
In this work we report on the sensitivity of photo-electrical detection of magnetic resonances (PDMR) for magnetometry measurement using low density nitrogen vacancy (NV) ensembles in CVD-grown diamond. We demonstrate that the selection of the laser excitation wavelength is of importance for achieving optimal magnetic field sensitivity. The PDMR sensitivity obtained using a yellow-green (561 nm) laser surpass the performances of a green laser (532 nm), by suppressing the photoionization of defects other than NV centres (such as P1 centres). It consequently allows to carry out the PDMR measurements at lower laser powers with increased magnetic resonance contrast. Noticeably for both the green and yellow-green illuminations PDMR leads to improved sensitivity to magnetic fields in the selected conditions compared to ODMR.

Magnetic field sensors are widely used in applications including consumer electronics and space probes. Their working principles are mainly based on classical electro-magnetism or semiconducting principles such as the Hall effect or giant magnetoresistance (GMR). A new generation of magnetometers that works on quantum mechanical principles, such as SQUIDS, vapor phase magnetometers and others [1], [2], have been developed in parallel. One of the possible magnetometer configurations, which recently triggered significant interests, is based on the NV color centre in diamond [3]–[5]. The NV spin sensor can detect the magnetic field through the detection of the Zeeman split between the m_s = -1 and m_s = +1 spin sublevels or through phase accumulation when m_S = 0 and m_S = (-1) are in a superposition state. Compared to other devices, the NV spins offer advantages in terms of vector field magnetometry, wide dynamic range, long term stability, and room-temperature operation [3], [4]. So far, Optically Detected Magnetic Resonance (ODMR) NV magnetometers, based on the detection of the photoluminescence emitted by NV centres under excitation (see Figure 1b), have been studied [5]–[7].

Sensitivities ranging from typically 1 $nT/Hz^{1/2}$ to below $1pT/Hz^{1/2}$ [3], depending on the experimental configuration and on the type of detection protocols used, have been reached. However, the main challenge for practical applications of such devices remains their miniaturization and integration into compact devices [7].

Alternatively, the NV spin state can be read using the recently established Photoelectric Detection of Magnetic Resonances (PDMR) [8]–[13]. PDMR make use of the spin-state dependent photocurrent resulting from NV centres two-photon ionization (Figure 1b) and might provide a pathway to compact sensors integrated with electronics. The essential parameter to evaluate the performance of such detectors is the detection sensitivity. In this work we evaluate the magnetic field sensitivity of a continuous-wave (CW) PDMR-read device and compare it with CW ODMR readout executed in parallel on the same sample. The highest sensitivities using NV centres have been achieved so far employing ODMR technique in dense NV ensembles (concentrations in the range of 1 ppm or higher) [6].

Nevertheless, there is also a range of applications using magnetometers with single NV centres with a typical CW sensitivity of $\sim 1\ \mu T/Hz^{1/2}$ per NV [14]. For pulsed measurements the sensitivity of $\sim 10\ \mu T/Hz^{1/2}$ has been reached using nanopillars for light detection.[15] The single NV centre configurations is also used, for example, in scanning diamond magnetometry to map the magnetic field at nanoscale. Low-density ensembles with isolated NV centres spread in 2D plane across the diamond surface can alternatively provide a high spatial resolution and mapping of magnetic field in wide-field magnetometry configuration, relevant for instance for biological sensing [15]. For this reason, we concentrate our work on low-density NV ensembles. Additionally, in such study the complex spin interactions present in high-density ensemble systems can be omitted allowing a better comparison of electrical and optical detection sensitivity.

CW ODMR and PDMR measurements were performed under yellow-green (561 nm) and green (532 nm) laser excitations. The selection of the excitation wavelength is important due to the presence of opto-electrically active defects other than NV centres in diamond crystals, in particular P1 centres (single substitutional nitrogen centres -N_S). These defects can be photoionized and thus contribute to the photoelectric signal, limiting the PDMR contrast [8]–[10], [12], [16]. We show that using yellow-green light the PDMR contrast can be substantially enhanced compared to green illumination, leading also to a 10-fold sensitivity improvement when compared to ODMR measured simultaneously on the same CVD diamond sample. The PDMR technique Is of interest for the development of sensitive magnetometers capable of miniaturization and integration with electronics.

The PDMR and ODMR measurements were carried out using a custom-built microscope that allows simultaneous optical and electrical detection of magnetic resonances [8]–[10], [12], [16]. A green (532 nm) or a yellow-green (561 nm) gem laser from Laser Quantum was pulsed at a low frequency (131 Hz) using acousto-optic modulators. The laser-pulsing frequency was used as a reference for lock-in readout of the photocurrent. The laser beams were focused on the diamond sample using an air objective (40x, numerical aperture of 0.95). The photoluminescence (PL) emitted by the diamond under excitation was filtered using a 650 nm and a 665 nm cut-off long-pass filters and detected in confocal mode using an avalanche photodiode (APD). For the experiments, we used a diamond layer epitaxially grown by plasma enhanced chemical vapor deposition (PDS-17 reactor from ASTeX) on top of a single-crystal high-pressure high-temperature [100] Ib diamond. The residual nitrogen in the growth chamber led to the formation of NV centres with the concentration of ~ 10 ppb (corresponding to ~ 200 NV centres in the optical confocal volume) as estimated from PL intensity compared to a reference sample with known NV concentration. The grown diamond sample was acid-cleaned in fuming H_2SO_4 with KNO_3 and rinsed in deionized water. It was equipped with interdigitated contacts (5 μm gap) for photocurrent detection and with a microwave (MW) strip-line for application of the MW field required for NV spin manipulations. Contacts and strip-lines were prepared by means of optical lithography using sputtering deposition and consisted of 20 nm layer of titanium covered with 100 nm layer of aluminum. The electrodes and the MW strip line were wire-bonded to the printed circuit board tracks (see Figure 1a). The proximity of the strip-line to the measured NV ensembles (~ ten of μm) allows to use low MW powers (i.e., lower than 100 mW), limiting thus the sample heating. A bias electric field (~3×10^4 $V \cdot cm^{-1}$) was applied between the electrodes and the collected photocurrent was pre-amplified (with a gain of 2×10^8 VA^{-1}) using a Stanford Research SR570 pre-amplifier and detected using a lock-in amplifier (Stanford Research SR850). The bias electric field was applied for both ODMR and PDMR measurements, as the two methods were used simultaneously.

To acquire the ODMR and PDMR spectra, the MW frequency was varied with the step size of 1-2 MHz (or 150 kHz for hyperfine measurements). Typically, 100 sweeps were acquired per spectrum with the duration of a single sweep of about 55 seconds. The IV characteristics measurements were carried out by sweeping the bias voltage from 0 V to +25 V while detecting the DC current with a picoammeter (Keithley 486).

To perform magnetometry measurements, the degenerated mS = -1 and mS = +1 spin sublevels of the NV centres ground state (see Figure 1b) were first split by applying an external magnetic field using a permanent neodymium magnet. Resulting characteristic 8-peak ODMR and PDMR spectra are depicted in Figure 2a and 2b. We remark that the spin contrast, defined below, of the 8 measured peaks was not evenly distributed, even when trying to fine tune the magnetic field orientation with a precision below 1 degree. This effect could be attributed either to a non-even incorporation of NV centres along the 4 main crystallographic directions during the CVD diamond growth or potentially to a not fully homogeneous magnetic field from our microscopic strip-line antenna. The highest ODMR and PDMR signal contrast (C) were obtained for the resonance line at ~2849 MHz, which was thus selected for further measurements. First, the hyperfine splitting induced by the adjacent 14N nuclear spin was measured both optically and electrically for comparison, using the same conditions (see Figure 2c and 2d). These measurements showed that PDMR can measure hyperfine spectra, similarly to ODMR.

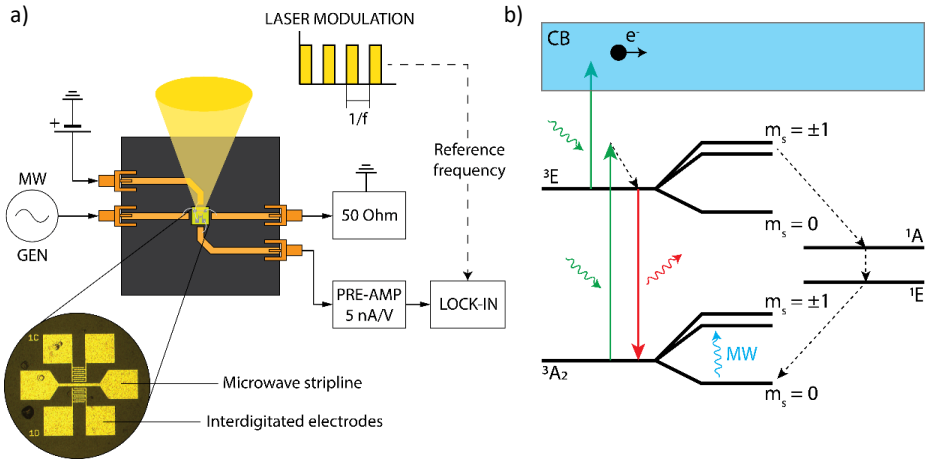

FIG. 1. A) Schematic of the PDMR chip used for experiments and the acquisition setup layout. B) Energy level diagram of the negatively charged NV centre, showing transitions responsible for ODMR and PDMR detection. The green arrows represent the NV two-photon excitation from the NV triplet ground state ($^3A_2$) to the triplet excited state (^3E) and subsequently from the ^3E state to the conduction band (CB) resulting in the generation of a free electron (e^-) contributing to the photoelectric signal. Alternatively, from the excited state, the electron can decay either radiatively emitting a visible photon (red arrow) or non-radiatively, through a spin-dependent transition to a singlet metastable state (^1E ground state and ^1A excited state). The Zeeman splitting frequency is proportional to the applied magnetic field $\Delta v = 2\gamma_{NV}B_z$ where Δv is frequency splitting, γ_{NV} is Bohr magneton, and B_z is magnetic field applied along NV axis.

The small difference between ODMR and PDMR hyperfine spectra linewidths (i.e., full-width-half-maximum - FWHM) can be attributed to the non-identical signal collection volumes addressed by each of the readout techniques [8]. Although the laser focus is the same for both methods, the ODMR detection volume is determined by confocal resolution (~500 nm) whereas in PDMR the

signal is collected from a volume defined by the convolution of the 2-photon absorption volume and the electric field profile and the mean free path of charge carriers [16]. As expected, the resulting FWHM of the single hyperfine line is ~3 times smaller than the FWHM of the fine electron spin resonance (ESR) line.

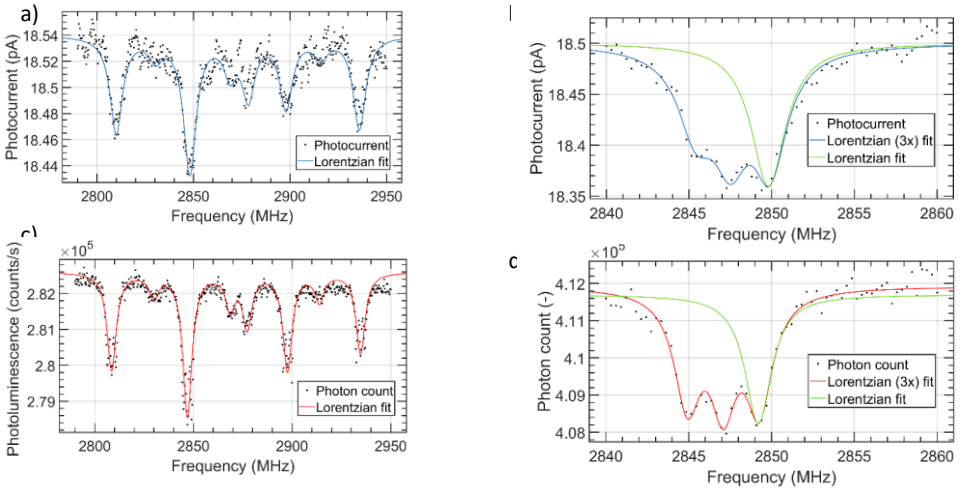

FIG. 2. The ODMR and PDMR spectra measured using yellow-green laser (561 nm). (a) ODMR and (b) PDMR spectra split in eight peaks using a permanent magnet. Single peak of the (c) ODMR and (d) PDMR spectra showing hyperfine interaction (FWHM = 1.95 MHz, C = 0.68 % and FWHM = 2.81 MHz, C = 0.87 % respectively). Experimental conditions: laser power 2.4 mW, microwave power 20 mW, bias voltage +15 V. The fitting used for case a) and b) was 8 peak Lorentzian fit, whereas in case of c) and d) single and triple Lorentzian fitting was used.

We define the measurement contrast as

$$C = (S_{\text{resonant}} - S_{\text{off-resonant}}) / S_{\text{off-resonant}} \quad (1)$$

where S is the photoluminescence or photoelectric signal measured either at resonant or off-resonant MW frequency. From previous works [8], [9], [16] we have found that P1 centres incorporated during the CVD growth reduce the measured PDMR spin contrast when using 532 nm green laser for the spin state readout and polarization. This is due to the fact that the measured current is increased by additional photocurrent generated from photoionization of P1 centres and other opto-electrically active defects.

For this reason, we compared two laser wavelengths (i.e., 532 nm and 561 nm). While the green laser photoionizes the P1 centres [17]–[20], the P1 photoionization cross section is significantly reduced for yellow-green excitation [17], [19]. On the other side, the cross-sections for NV^- photoionization and for repumping of NV^0 to the original NV^- charge state after the photoionization differ only slightly for the two used laser wavelengths [21], [22].

To characterize the photocurrent value, we have measured the current-voltage (I-V) characteristics for different laser powers for both used wavelengths. For these measurements we did not apply any MW field. The resulting I-V curves are depicted in Figure 3a and 3b. It should be mentioned that the photogenerated current includes the electron current as well as the hole current produced by the repumping of the NV^0 charge state to NV^- state [12], [23]. The photon energy of the green laser (2.33 eV) is sufficient to ionize other diamond-related defects (such as P1 centres - photoionization onset ~2.25 eV) resulting in higher detected photocurrent. On the other hand, using yellow-green (2.21 eV) illumination reduces the total photocurrent, which we attribute mainly to the reduction of P1 centre photoionization, although some other defects can be involved as well [16]. Therefore, for the yellow-green excitation we do not need to use very high laser power to have the two-photon NV photoionization dominate over the one-photon P1 centre photoionization. Consequently, the yellow-green is more efficient for NV current generation in terms of signal-to-background ratio.

Further on, we measured the PDMR and ODMR spectra in the range 2.7 to 3 GHz for both the yellow-green and the green laser excitations to examine the value of the spin contrast. We fit the measured resonance peaks (both for PL and photocurrent detection) using a Lorentzian function and calculated the magnetic resonance contrast from the fit. The resulting PDMR contrast dependence on laser power and laser color is depicted in Figure 3c. At lower laser powers (below ~5 mW), a high spin contrast is observed for yellow-green light excitation, whereas we did not observe any spin contrast for the green (in this case the resonance is buried in the noise, as the NV photocurrent modulates the P1 photocurrent). The maximal PDMR contrast obtained under yellow-green illumination (~ 3.2 %) is similar to the maximal ODMR contrast observed under the same excitation wavelength (see below) for the measured sample. This fact supports our conclusions about lower probability of P1 centre ionization by 561 nm laser. At higher laser powers, the PDMR contrast is relatively low for both laser colours. We attribute this effect to the too high rate of light-induced spin polarization compared to the Rabi driving rate (proportional to the square root of the MW power) for high optical excitation powers, as well documented in literature [24]. The best conditions, yielding highest PDMR contrast for given MW power, were for yellow-green excitation at 1.6 mW. Notably, we observe a shift in laser power for the green and yellow-green spin contrast maximum. This fact is in line with generation of photocurrent from P1 centres using the green light: sin fact since we consume some photons for P1 photoionization (i.e., our effective optical power on the NV centres is lower), the NV excitation rates for green are lower and the maximum contrast is obtained at a higher laser power compared to yellow excitation.

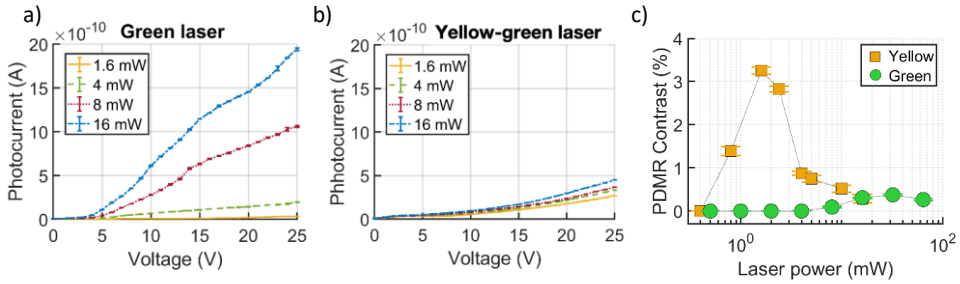

FIG. 3. Comparison of yellow-green and green laser illumination for photoelectric detection. (a) IV curve for green laser illumination measured with picoammeter. (b) IV curve for yellow-green laser illumination measured with picoammeter. (c) PDMR contrast as function of laser excitation power. Microwave power 190 mW (for green), and 250 mW (for yellow-green), bias voltage +15 V.

Based on the experimental results, we predict the sensitivity for the PDMR magnetometry and compare it to the ODMR. For this purpose, we used the shot-noise limited sensitivity (η) formula of the NV system [25]:

$$\eta = \frac{4h}{3\sqrt{3}g\mu_B} \cdot \frac{v}{c\sqrt{R}}, \tag{2}$$

where h is the Planck constant, g is NV gyromagnetic ratio, μ_B is the Bohr magneton, C is the experimental spin contrast, v is the measured FWHM, and R is the signal (i.e., the number of detected photons per second for ODMR or electrons per second for PDMR).

The calculated sensitivities based on the measured data are shown in Figure 4 together with the experimental values of FWHM, spin contrast, and the detection rate. The PDMR measurements with low power green excitation did not lead to any detectable contrast within the signal/noise ratio limits as discussed above. In case of the yellow-green excitation, the spin contrast was significantly enhanced, equalling the contrast of ODMR for the same excitation wavelength. Because under low excitation power the FWHM were also similar for both readout techniques, it is mainly the total photoelectric detection rate with respect to the photon count for ODMR that leads to the enhanced magnetic field sensitivity obtained using PDMR. Noticeably for both the green (for higher laser power) and the yellow-green illuminations (in all measured laser power range) PDMR leads to improved sensitivity compared to ODMR. It should be noted that the use of yellow-green excitation enables to reach a high PDMR sensitivity under considerably reduced laser power. As mentioned earlier, we used low-density NV ensembles with typical concentration around 10 ppb (200 NV centres in the volume contributing to the photoelectric signal). This corresponds to CW PDMR magnetic field sensitivity of about 100 nT/Hz$^{1/2}$, which compares approximately to ~1 μT/Hz$^{1/2}$ for single NV CW ODMR sensitivity in the scanning nanoprobes.[14] The sample that we used for our experiment has rather broad resonance lines, with FWHM in the range of 10 MHz. By using hyperfine lines due to interaction with the ^{14}N spin the linewidth of about 3 MHz was achieved.

However, the FWHM can be further reduced significantly (i.e., below 100 kHz) for low NV doped samples, for example by using ^{12}C isotopically enhanced diamond, thus improving the sensitivity to 1 nT/Hz$^{1/2}$. By increasing the NV concentration and the input laser power the sensitivity could also be further enhanced significantly.

Further device geometry optimization as well as using diamond with narrow NV resonance bandwidth will allow further improvement of the sensitivity. The advantages of our approach are the demonstrated ten-fold increased performance of PDMR compared to ODMR on the same low NV density sample and the possibility to use our method for devices that are fully integrable in compact magnetometers.

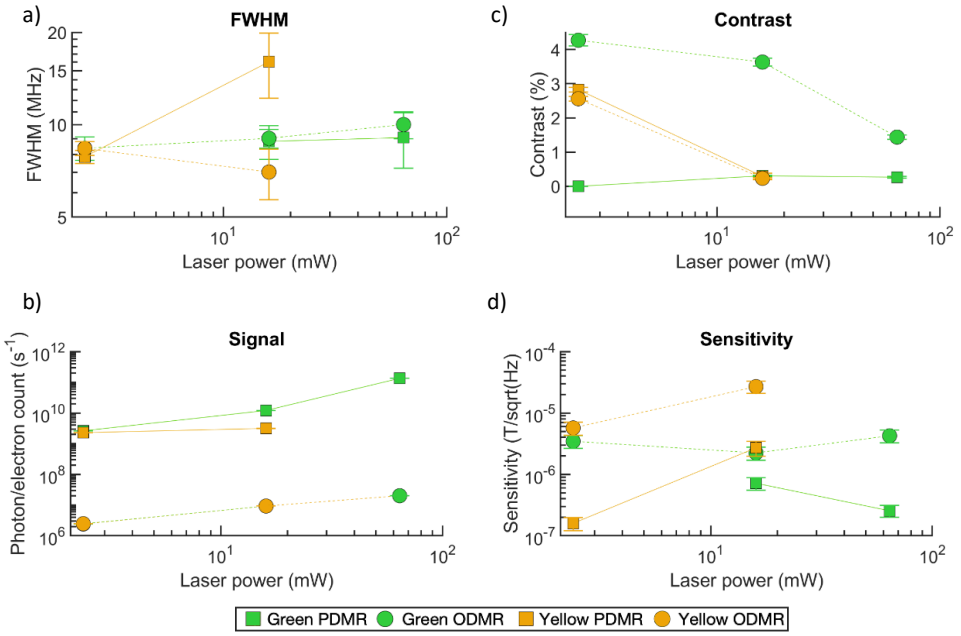

FIG. 4. Magnetic field sensitivity predictions for PDMR and ODMR using yellow-green and green laser. (a) Effect of laser power on the FWHM and (b) on the measured spin contrast. (c) Effect of laser power on detection rate. (d) Sensitivity dependency on laser power. Grey lines serve for eye guidance. Microwave power 190 mW (for green), and 250 mW (for yellow-green). Bias voltage +15 V.

In summary, we have studied the sensitivity of the electrical readout technique for magnetometry measurement using a CVD-grown diamond sample with low NV concentration. We show that the selection of the laser excitation color is of importance in order to achieve optimal magnetic field sensitivity. The PDMR performances obtained using a yellow-green (561 nm) laser surpass the performances of a green laser (532 nm); the higher wavelength illumination enables to achieve better signal-to-background ratio by suppressing the photoionization of defects other than NV centres (such as P1 centres). It

consequently allows to carry out the PDMR measurements at lower laser powers with increased magnetic resonance contrast. In comparison to ODMR, photoelectric readout leads to ten times improved sensitivity to magnetic fields in the selected conditions. Future experimental work is necessary to gain better understanding about the possible charge exchanges between NV centres and other donor or acceptor defects in diamond, which could affect the PDMR contrast.

ACKNOWLEDGMENTS

M.N. acknowledges the QuantERA projects Q-Magine No. S010518N and NanoSpin No. S010418N funded through the Flemish Scientific Foundation (FWO) as well as FWO projects No. G0E7417N and No. G0A0520N and Quantum Flagship project ASTERIQS, No. 820394 and DIAQUANT project, No. S004018N, funded by SBO-FWO. J.H. is a PhD fellow of the FWO No. 11D6620N.

AUTHOR'S CONTRIBUTIONS

J.H. conducted the measurements. M.G., E.B. carried out experimental optimization of detection setup. J.H. developed acquisition software and tailored the setup for photocurrent magnetometry readout, J.H. fabricated electrodes on the diamond sample and was mentored by M.M., E.B., M.N., and I.P.R. supervised partial sub-projects and took part in detailed discussions of results. J.H., M.G, E.B., and M.N. contributed to the manuscript writing. All authors discussed the results and commented on the manuscript. M.N supervised the joint efforts.

REFERENCES

[1] T. Schönau et al., 'A three-axis SQUID-based absolute vector magnetometer', Review of Scientific Instruments, vol. 86, no. 10, p. 105002, Oct. 2015, doi: 10.1063/1.4933386.

[2] Y. Sebbag, E. Talker, A. Naiman, Y. Barash, and U. Levy, 'Demonstration of an integrated nanophotonic chip-scale alkali vapor magnetometer using inverse design', Light Sci Appl, vol. 10, no. 1, p. 54, Mar. 2021, doi: 10.1038/s41377-021-00499-5.

[3] J. F. Barry et al., 'Sensitivity optimization for NV-diamond magnetometry', Rev. Mod. Phys., vol. 92, no. 1, p. 015004, Mar. 2020, doi: 10.1103/RevModPhys.92.015004.

[4] L. Rondin, J.-P. Tetienne, T. Hingant, J.-F. Roch, P. Maletinsky, and V. Jacques, 'Magnetometry with nitrogen-vacancy defects in diamond', Rep. Prog. Phys., vol. 77, no. 5, p. 056503, May 2014, doi: 10.1088/0034-4885/77/5/056503.

[5] F. M. Stürner et al., 'Integrated and Portable Magnetometer Based on Nitrogen-Vacancy Ensembles in Diamond', Advanced Quantum Technologies, vol. 4, no. 4, p. 2000111, 2021, doi: 10.1002/qute.202000111.

[6] T. Wolf et al., 'Subpicotesla Diamond Magnetometry', Phys. Rev. X, vol. 5, no. 4, p. 041001, Oct. 2015, doi: 10.1103/PhysRevX.5.041001.

[7] F. M. Stürner et al., 'Compact integrated magnetometer based on nitrogen-vacancy centres in diamond', Diamond and Related Materials, vol. 93, pp. 59–65, Mar. 2019, doi: 10.1016/j.diamond.2019.01.008.

[8] E. Bourgeois et al., 'Photoelectric detection of electron spin resonance of nitrogen-vacancy centres in diamond', Nat Commun, vol. 6, no. 1, p. 8577, Oct. 2015, doi: 10.1038/ncomms9577.

[9] E. Bourgeois et al., 'Enhanced photoelectric detection of NV magnetic resonances in diamond under dual-beam excitation', Phys. Rev. B, vol. 95, no. 4, p. 041402, Jan. 2017, doi: 10.1103/PhysRevB.95.041402.

[10] M. Gulka et al., 'Pulsed Photoelectric Coherent Manipulation and Detection of NV Centre Spins in Diamond', Phys. Rev. Applied, vol. 7, no. 4, p. 044032, Apr. 2017, doi: 10.1103/PhysRevApplied.7.044032.

[11] F. M. Hrubesch, G. Braunbeck, M. Stutzmann, F. Reinhard, and M. S. Brandt, 'Efficient Electrical Spin Readout of NV Centres in Diamond', Phys. Rev. Lett., vol. 118, no. 3, p. 037601, Jan. 2017, doi: 10.1103/PhysRevLett.118.037601.

[12] M. Gulka et al., 'Room-temperature control and electrical readout of individual nitrogen-vacancy nuclear spins', Nat Commun, vol. 12, no. 1, p. 4421, Jul. 2021, doi: 10.1038/s41467-021-24494-x.

[13] T. Murooka et al., 'Photoelectrical detection of nitrogen-vacancy centres by utilizing diamond lateral p–i–n diodes', Appl. Phys. Lett., vol. 118, no. 25, p. 253502, Jun. 2021, doi: 10.1063/5.0055852.

[14] M. S. Grinolds et al., 'Nanoscale magnetic imaging of a single electron spin under ambient conditions', Nature Phys, vol. 9, no. 4, pp. 215–219, Apr. 2013, doi: 10.1038/nphys2543.

[15] D. Le Sage et al., 'Optical magnetic imaging of living cells', Nature, vol. 496, no. 7446, pp. 486–489, Apr. 2013, doi: 10.1038/nature12072.

[16] E. Bourgeois, M. Gulka, and M. Nesladek, 'Photoelectric Detection and Quantum Readout of Nitrogen-Vacancy Centre Spin States in Diamond', Advanced Optical Materials, vol. 8, no. 12, p. 1902132, 2020, doi: 10.1002/adom.201902132.

[17] M. Nesládek, K. Meykens, L. M. Stals, M. Vaněček, and J. Rosa, 'Origin of characteristic subgap optical absorption in CVD diamond films', Phys. Rev. B, vol. 54, no. 8, pp. 5552–5561, Aug. 1996, doi: 10.1103/PhysRevB.54.5552.

[18] W. J. P. van Enckevort and E. H. Versteegen, 'Temperature dependence of optical absorption by the single-substitutional nitrogen donor in diamond', J. Phys.: Condens. Matter, vol. 4, no. 9, pp. 2361–2373, Mar. 1992, doi: 10.1088/0953-8984/4/9/028.

[19] M. Nesládek et al., 'Dominant defect levels in diamond thin films: A photocurrent and electron paramagnetic resonance study', Appl. Phys. Lett., vol. 72, no. 25, pp. 3306–3308, Jun. 1998, doi: 10.1063/1.121632.

[20] J. Rosa, M. Vaněček, M. Nesládek, and L. M. Stals, 'On Photocurrent (and EPR) Study of Defect Levels in CVD Diamond', physica status solidi (a), vol. 172, no. 1, pp. 113–122, 1999, doi: 10.1002/(SICI)1521-396X(199903)172:1<113::AID-PSSA113>3.0.CO;2-I.

[21] N. Aslam, G. Waldherr, P. Neumann, F. Jelezko, and J. Wrachtrup, 'Photo-induced ionization dynamics of the nitrogen vacancy defect in diamond

investigated by single-shot charge state detection', New J. Phys., vol. 15, no. 1, p. 013064, Jan. 2013, doi: 10.1088/1367-2630/15/1/013064.

[22] L. Razinkovas, M. Maciaszek, F. Reinhard, M. W. Doherty, and A. Alkauskas, 'Photoionization of negatively charged NV centres in diamond: theory and ab initio calculations', arXiv:2104.09144 [cond-mat, physics:physics, physics:quant-ph], Apr. 2021, Accessed: Aug. 23, 2021. [Online]. Available: http://arxiv.org/abs/2104.09144

[23] P. Siyushev et al., 'Photoelectrical imaging and coherent spin-state readout of single nitrogen-vacancy centres in diamond', Science, vol. 363, no. 6428, pp. 728–731, Feb. 2019, doi: 10.1126/science.aav2789.

[24] K. Jensen, V. M. Acosta, A. Jarmola, and D. Budker, 'Light narrowing of magnetic resonances in ensembles of nitrogen-vacancy centres in diamond', Phys. Rev. B, vol. 87, no. 1, p. 014115, Jan. 2013, doi: 10.1103/PhysRevB.87.014115.

[25] A. Dréau et al., 'Avoiding power broadening in optically detected magnetic resonance of single NV defects for enhanced dc magnetic field sensitivity', Phys. Rev. B, vol. 84, no. 19, p. 195204, Nov. 2011, doi: 10.1103/PhysRevB.84.195204.

6. Chapter 6 - Electrical readout microwave-free sensing with diamond

Authors contribution: To this paper I contributed by preparation of the electrodes on the sample and the quantum chip, as well as I contributed to setting up and development of the PDMR based GSLAC measurement. I also partook in the paper writing. Huijie Zheng and myself are the first authors with the same contribution. This work is related to my PhD topic by exploring novel advanced potential use-cases for the PDMR readout technique, in this case microwave-free detection of magnetic resonance, which opens up new domain of research and industrial applications, where using a microwave fields is prohibited or influencing the measured parameters.

Manuscript accepted in Phys. Rev. Applied

Electrical readout microwave-free sensing with diamond

Huijie Zheng†,[1,2,] [1] **Jaroslav Hruby**,[3,4,] [2] Emilie Bourgeois,[3,4] Josef Soucek,[3,5] Petr Siyushev,[6]

Fedor Jelezko,[6] Arne Wickenbrock,[1,2] Milos Nesladek,[3,4,5] and Dmitry Budker[1,2,7]

1 Johannes Gutenberg-Universit¨at Mainz, 55128 Mainz, Germany

2 Helmholtz-Institut, GSI Helmholtzzentrum fur Schwerionenforschung, 55128 Mainz, Germany

3 IMOMEC division, IMEC, Wetenschapspark 1, B-3590 Diepenbeek, Belgium

4 Institute for Materials Research (IMO), Hasselt University, Wetenschapspark 1, B-3590 Diepenbeek, Belgium.

5 Czech Technical University in Prague, Sitna sq. 3105, 272 01, Kladno, Czech

6 Institute for Quantum Optics and IQST, Ulm University, Albert-Einstein-Allee 11, D-89081 Ulm, Germany

7 Department of Physics, University of California, Berkeley, California 94720, USA

(Dated: January 7, 2022)

† authors with the same contributions

[1] zheng@uni-mainz.de

[2] These authors contributed equally to this work.

Abstract: While nitrogen-vacancy (NV^-) centers have been extensively investigated in the context of spinbased quantum technologies, the spin-state readout is conventionally performed optically, which may limit miniaturization and scalability. Here, we report photoelectric readout of ground-state cross-relaxation features, which serves as a method for measuring electron spin resonance spectra of nanoscale electronic environments and also for microwave-free sensing. As a proof of concept, by systematically tuning NV centers into resonance with the target electronic system, we extracted the spectra for the P1 electronic spin bath in diamond. Such detection may enable probing optically inactive defects and the dynamics of local spin environment. We also demonstrate a magnetometer based on photoelectric detection of the ground-state level anticrossings (GSLAC), which exhibits a favorable detection efficiency as well as magnetic sensitivity. This approach may offer potential solutions for determining spin densities and characterizing local environment.

Nitrogen-vacancy (NV) centers in diamond have become a prominent platform for spin-based quantum technology, being utilized to study small-scale quantum information processing concepts and quantum sensing under ambient conditions[1, 2]. Conventionally, the readout of the spin state is based on the optically detected magnetic resonance (ODMR) technique and NV center visualization is performed optically, taking advantage of the high-yield photoluminescence of the NVs. This typically requires setups built on optical tables to achieve the best performance. In that sense, fabrication of miniaturized compact devices and their integration for practical uses is a complex engineering endeavor[3, 4]. Alternatively, electrical readout is a convenient way to measure the spin state of a qubit, and recently, it has been successfully applied to NV centers via, for example, photoelectric detection of magnetic resonance (PDMR)[5], as well as photoelectric readout of electron[6] and nuclear[7, 8] spins. With this detection method, NV^- centers can be addressed with a spatial resolution limited by the nanoscale feature size of electron-beam lithography[3, 5, 6, 8, 9], which could enable spin readout in fabricated dense arrays, and therefore, providing fully integrated quantum diamond solutions. The advantage over optical readout is that photocurrent (PC) detection allows one to overcome the spatial resolution limitation imposed by the diffraction limit. Moreover, electrical readout outperforms optical means in collection efficiency, as the latter are limited by finite-efficiency objective optics and the high index of refraction of diamond, and it is typically on the order of a percent of lower[3]. Photoelectric detection can achieve high efficiency since all the carriers can be collected and multiplied due to photoelectric gain[5]. However, an important problem is the microwave (MW) induced noise and cross-talks[8] which limit the sensitivity of magnetic field sensing and imaging and also provides engineering and technological hurdles for a high-level integration.

Here, we propose and implement a novel microwave-free PDMR detection for monitoring the local NV electron spin dynamics within the diamond lattice; in this scenario, we study spin transitions at the ground-state level anti-crossings (GSLAC), occurring at the fields of ≈ 102.4mT, which lead to narrow resonances and can be employed for sensitive magnetometry. The role of nuclear spins in these transitions and pinpoint differences to microwave-free detection is discussed in Ref.[10]. The developed methodology also opens perspectives for highly integrated magnetometry with electrical readout.

We begin with the investigation of magnetic resonances that originate from ground-state level anticrossing (GSLAC) and cross relaxation by performing both photoelectric and optical readout. Based on these results, we designed and implemented a magnetometer based on the PC detection of the GSLAC. This magnetometer alleviates the requirement of microwave control[11] and PC readout enables better magnetic sensitivity per volume compared to optical detection.

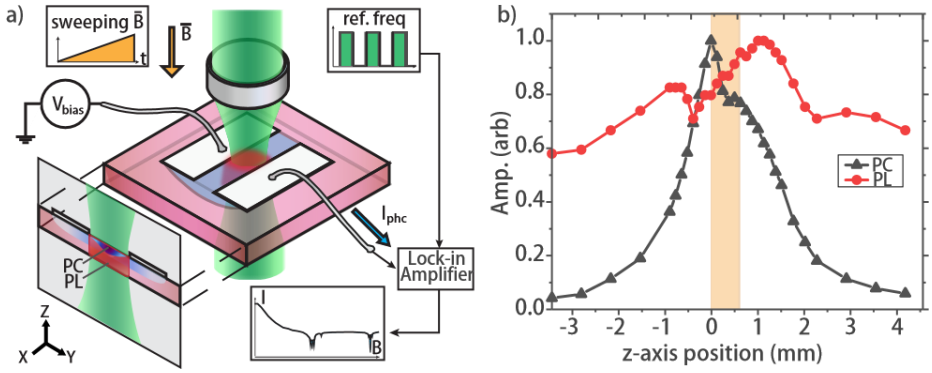

FIG. 1. (a) Schematic representation of the setup used for PC detection. A static magnetic field (B_s) is applied along an NV axis (the z direction). A green laser beam is focused in between a pair of 5μm separated lithographic electrodes. The PC signal, I_{phc}, is detected with a lock-in amplifier with reference to the modulation frequency of the laser light by an acousto-optic modulator (AOM). A projected side view indicates the effective detection volume of PC (blue region) and PL (red region) readout. (b) The signals of PC (black solid triangles) and PL (red solid circles) readout when the focus lens is moved along the light-propagation direction (z-axis, perpendicular to the diamond surface). The diamond sample is indicated with an amber rectangle.

Photoelectric detection of NV⁻ magnetic spectra.

Throughout the experiments a high-pressure high temperature (HPHT) diamond was used (see Appendix B). To collect charge carriers under bias voltage, coplanar Ti/Al electrodes with a 5μm gap were lithographically patterned on the diamond surface. The photocurrent was pre-amplified and recorded via lock-in amplifier (LIA) with a reference to the laser modulation frequency. A custom-made electromagnet was built to provide the background magnetic field [11]. A schematic of the experimental apparatus is depicted in Fig.1 (a), in which a cutaway sectional view is projected to the left. The laser beam is focused onto the diamond with a lens which is mounted on a three-axis translation stage, so that the focal spot can be moved. Optical detection of magnetic resonance and PC readout were carried out simultaneously.

We started our measurements by characterizing an effective interrogation area for the two detection methods, by positioning the laser spot in the vicinity of the electrodes. The laser beam is focused with an estimated beam waist of $\approx 6\mu$m and Rayleigh range $\approx 200\mu$m. We park the spot between the electrodes in the x-y plane and scan the beam through the sample along the z-axis. Figure 1 (b) depicts the recorded signals of PC and PL as the focal point crosses the diamond (note a 50V electric potential to the electrodes was applied in both cases to achieve comparable detection conditions). The scan in Fig.1 (b) starts with the focal point outside the diamond (denoted by the amber rectangle), then proceeds to the electrode plane (front diamond surface, roughly at 0mm where the maximum PC occurs), continues into the diamond sample, towards its back side at 0.65mm, and finally, out of the diamond. The PC signal soars rapidly from nearly zero to maximum within 3-mm movement of the lens when the laser focal spot approaches the near diamond surface, and reaches a maximum at when it is focused exactly on the surface. Under this condition, the NV centers in the effective photoelectric interrogation volume experience optimal optical excitation. When the laser spot passes through the electrode plane, the PC signal falls quickly due to less intense photoionization which is quadratically dependent on the laser intensity, and a rapidly decaying electric field[12]. The PL signal, however, experiences a different z-axial profile: it slightly increases from the level of 0.6 to 0.8 when the focal spot moves from -3mm to -1mm and then falls suddenly to a level of 70% to the maximum.

The reasons behind involve blocking effect of the laser beam by the electrodes. Note the NV centers contributed to the PL across over the entire depth of the sample. PL signal gets maximized at $\sim$ 1.1mm where the focal spot has passed the whole diamond sample. Thereafter, it decreases to 70% at 2mm and finally flattens out.

From the discussion above, we conclude that the electrical readout provides a smaller effective interrogation volume compared to that of the fluorescing region due to the sharp electric field profile and the two-photon ionization process. Conversely, with optical detection, one collects photons from the entire illuminated volume. To better understand the system, we quantitatively reproduce the electric and optical signals based on a microscopic mathematical model[13] and estimate the dimension of the effective detection volume for the two detection methods. The model potentially allows us to predict the densities of NV centers as well as optically inactive impurities [such as substitutional nitrogen atoms (P1 centers)].

Photoionization within diamond.

Figure2 summarizes optical and spin transitions at the 51mT and the GSLAC point. Under sufficient optical illumination, defects inside semiconductor material can be ionized, thereby producing charge carries that move towards electrodes under electric field[15, 16]. Figure2 (a) illustrates the photoionization of NV centers and P1 centers. The photoionization cycle of NV centers in diamond is spin-dependent[14]. Incoming photons with the energy of 1.94eV or higher, can be can lead to photoionization via two photon process of the NV center [3]. In the first ionization step, the electron of the NV promoted to the excited state can decay either radiatively back to the ground state or non-radiatively into the long-lived metastable singlet state (intersystem crossing, ISC). The excited NVs can be further promoted to the conduction band by absorption of a second photon. Under an applied electric field, the electrons can freely travel in the conduction band and can finally be collected. Photoionization changes the NV charge state from NV^- to NV^0. The recovery of the NV^- center by back conversion from NV^0 can be induced by two-photon excitation of the NV^0 center and capture of an electron from the valence band[3]. Recently, it has been suggested that this process can also be accomplished by a single photon[14, 17]. The dynamical cycling between the two charge states is enabled by optical excitation with wavelengths shorter than the zero-phonon line of NV0 [16], in particular, the energies > 2.6eV are needed for that step. Thus, two charge carriers are produced within one cycle: one electron during ionization and one hole during NV− recovery[3]. This dynamic charge circulation enables photoelectric readout of NV centers. Photoionization inside diamond lattice can involve also other defects, e.g. P1 centers. The electrons from P1 centers can be promoted to the CB directly via one-photon ionization [Fig.2 (a)][5, 12, 16]. These generated charge carriers lead to a background photocurrent signal [Fig.2 (a)].

As discussed above, the photoinduced current in ensemble experiments involves the signal produced by both NV and P1 centers. Identifying individual contributions of the two types of defects, would provide additional information useful for optimization of photoelectric readout. Towards this goal, we explored the sharp features in the magnetic-field dependence of both the PC and PL signals, corresponding to the GSLAC and other B-field regions with enhanced cross-relaxation. These are identified as being due to NV-NV[18] and NV interactions with other spins such as those of P1 centers. Some of these features detected optically have already been discussed in Ref.[19]. In Fig.2 (b) we present normalized PL and photocurrent signals as a function of the applied magnetic field under various powers of the green laser light. This figure gives an overview of the changes in the spin contrast and the resonance linewidth, of the cross-relaxation and anticrossing features. Note that the contrast is defined as (signaloff − signalon)/signaloff. A remarkably sharp feature around 102.4mT, indicates the GSLAC which occurs when the Zeeman shift of the |ms = −1i component equals to the zero-field splitting[11, 20]. At around 51.2mT, the observed features correspond to cross-relaxation between the NV center and P1

[3] If the photon energy is higher than 2.6eV, an electron can be promoted from the ground state ($^3A_2$) directly to the CB[14].

centers [20–24], where these two defects can exchange energy due to resonant transition frequencies[21]. The feature that appears near 59mT corresponds to cross-relaxation between on-axis (along z) and off-axis NVs. The sharp GSLAC and relaxation features can be used for detecting electron spin resonance (ESR) with ODMR by tuning the static external magnetic field[22]. In our work, we show the first electric-readout demonstration of ESR that can be used for both spin-system characterization and sensing.

From Fig.2 it is clear that the observed magnetic features show different dependence on the light power in the two detection methods. As concerns the PC readout, both the initial drop [the slope between 0 and 30mT, see Fig.2 (b)] and the GSLAC feature [Fig.2 (c, middle)] increase in magnitude and also their spectral resolution gradually increases under stronger laser excitation, while they remain nearly constant in PL readout. One reason is the photocurrent background from the non-NV defects photoionization which adds a constant photocurrent background, therefore also reducing the spin contrast. Because the NV-related features come from twophoton processes while the P1 centers responsible for the background are ionized with a single photon, the contrast of the measurement improves at higher light powers. Also, the local spin environment can be altered with the application of green light as discussed in Ref. [17]. Currently, it is not known whether such changes will affect the PL and PC readout in the same way. Furthermore, such effects could also account for the narrowing of the GSLAC features (in both methods) in the presence of light, see Fig.2 (c, bottom), due to depopulation of interacting spins (P1s) in the vicinity of NV centers, since more and more impurities are photoionized. This might also explain why the shape and the linewidth of the crossrelaxation feature at 51 mT, see Fig.2 (b), stays nearly the same if observed via PC detection. Interestingly, at the same time, the contrast reduces in the PL signal for feature at 51mT with increasing the laser power. We note also that the NV-NV cross-relaxation feature at 59.5mT and the satellite features around GSLAC, which are prominent in PL have a much lower contrast in PC. The contrast in PL detection on the NV-NV feature accounts up to 2% at low laser power and decreases to 0.7% at higher laser power. For PC, the contrast is too low (<0.1%) to be quantitatively determined over the entire light-power range. For completeness, we point out the ratio of the PL contrasts of the NV-NV to NV-P1 features changes from 0.4 at low light power to 0.22 at high power. The difference in background signals in the overall measurement with the two methods does not fully account for the specific observation here. Understanding the reasons for these behaviors will be the subject of future work.

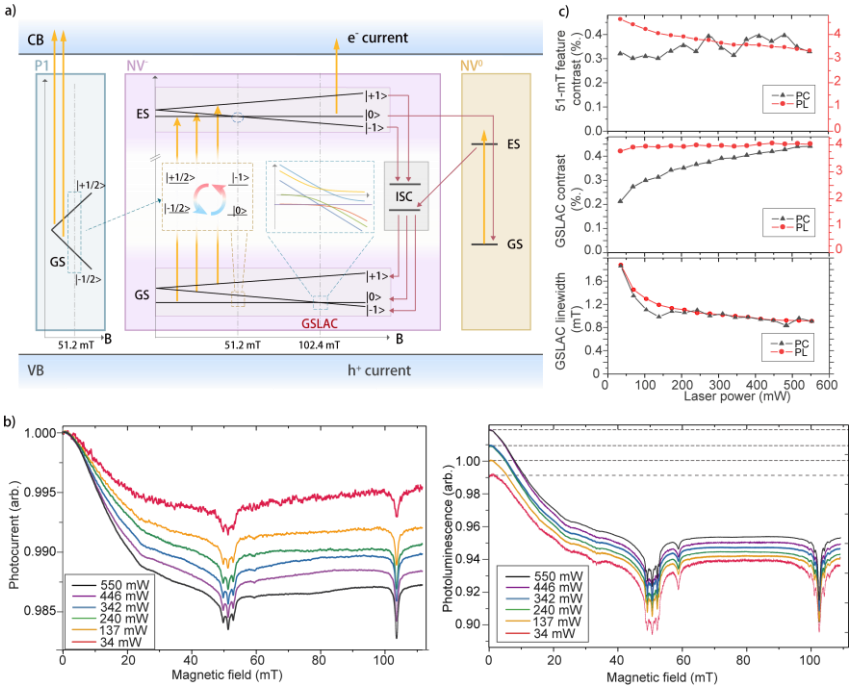

FIG. 2. PC detection vs magnetic field under various laser power. (a) The conventionally assumed photoionization mechanism of NV and P1 defects in diamond (an alternative mechanism has recently discussed in Ref.[14]. Charge and spin initialization is carried out via 532nm laser excitation (amber arrow). The red arrows denote non-radiative decay of electrons to the metastable states or the neutral state (NV^0). ISC: Inter-system crossing. CB: conduction band. VB: valence band. e^-: electron. h^+: free hole. (b) PC (left) and PL (right) signal as a function of magnetic field. The PC and PL signals were monitored while the magnetic field was scanned from 0 to 110 mT in 5 s. The green laser beam of various powers is modulated and the PC is synchronously detected with lock-in amplifier. The data are normalized to the signal value at zero field. The laser power is indicated in corresponding colors in the legend. For visual clarity, the traces in the right figure are manually shifted. The electrical potential applied to the electrodes is 17V. (c) Obtained parameters (contrast and/or full width at half maximum (FWHM)) for the features of cross relaxation and the GSLAC with photoluminescence (solid circles) and PC (solid triangles) readout as a function of the green laser power

To compare with the experiment, we calculate the PC and PL signal in the given experimental conditions and geometric configuration, taking into account the cross section of the Pl emission, photoionization thresholds, optical saturation, etc.[14]. The rate values are taken from the published data calculations that have been verified by comparing the PL and PC traces for different laser powers[13]. Figures 3(a) and (b) show the predicted and measured laser-power dependence of the total PC and PL. Whilst the PC dependence is predicted to be saturation free, in accord with previous models[5], PL should saturate due to the limit imposed by the lifetime of NV^- excited states and shelving into metastable

singlet states. The small deviation from the experiment can be accounted for by the shadowing of the diamond by the electrodes, so effectively the power density is reduced. Figure 3 (c) illustrates the simulated PC and PL signals originating from the NV centers at different depths below the surface where laser spot and electrodes are. The local contributions are indicated with blue and red shaded area (in arbitrary units). It is clear that 90% PC signal comes from a region within 0-30μm in depth where the NV centers experience sufficient both optical excitation and electric field to drive the charge carriers towards electrodes. While photoluminescence is produced throughout the diamond slab and detected once photons get out of the diamond chip, the photocurrent only from the high E-field region beneath the contact is detected. Based on the simulations, we estimate the ratio of effective interrogation volumes of PC to PL detection to be on the order of 1:20.

Electrical-readout magnetometer.

The B-field dependent relaxation at GSLAC can be used for a realization of a microwave-free magnetometer. The principle of PL detection at the GSLAC is introduced in Ref.[20]. Here we extend our approach to photocurrent readout. We apply an alternating magnetic field in addition to the bias field, and the fluorescence signal is demodulated in a properly phased LIA. The derivative signal, corresponding to the changes of the GSLAC slope with respect to the applied alternating B-field is shown in Fig.4(a) with a modulation frequency of 3.3kHz, and a modulation depth of ≈0.1mT which we select to be smaller than the FWHM. Around the GSLAC feature, the derivative signal depends approximately linearly on the magnetic field and can therefore be used for precise magnetic field measurements. The alignment and laser power were optimized to maximize the slope and the sensitivity of the magnetometer. The data near into magnetic field (calibration). Then the background magnetic field is set to the center of the GSLAC feature the zero-crossing are fit with a straight line to translate the LIA output signal (102.4mT) where the magnetometer is maximally sensitive to external magnetic fields. The sensitivity of the magnetometer can be deduced from the noise in the LIA output and the calibration.

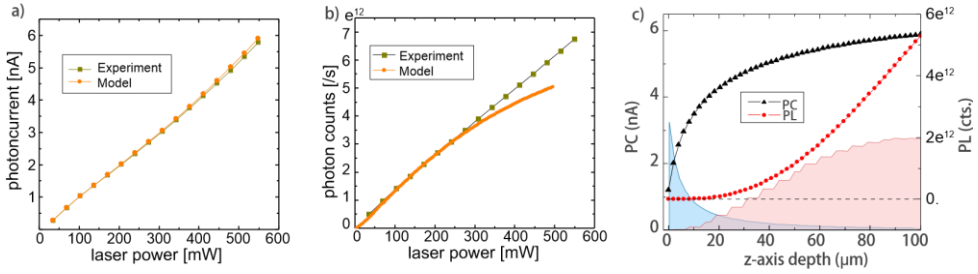

FIG. 3. (a). Calculated (orange) and Experimental (green) PC signal vs laser power. (b). Calculated (Orange) and Experimental (Green) PL signal vs laser power. (c) Calculated accumulated PC (black) and PL (red) signal as function of penetrating depth into diamond chip. Blue (red) shaded area indicates local contribution to the PC (PL) signal in arbitrary units.

For noise measurements, the LIA output is recorded for 1s. The data are passed through a fast Fourier transform as displayed in Fig.4(b), from which we can establish the noise-floor and the sensitivity spectrum. For comparison, similar data are collected for both PC (blue) and PL (red) detection, at a magnetic field of the GSLAC and also around 80mT (black for PC and green for PL). The on-resonance noise floor is flat at around 350nT/√Hz and 90nT/ Hz, respectively. At a field that is away from the GSLAC, the setup is insensitive to magnetic field variations and the data can be used to understand the technical noise level of the magnetometer. The off-resonance noise floor is flat at around 350nT/√Hz and 30nT/√Hz, respectively. In the case of PC detection, the collection rate for electrons is significantly lower than the photon collection rate in the PL detection due to the mismatch of the interrogation volume, which decreases the signal to noise ratio. As mentioned, in the present geometry, the effective interrogation volume for PC detection is smaller than that for PL by a factor of 20, thus the electric-readout magnetometer would outperform a PL-based magnetometer in magnetic sensitivity per detection volume. According to the simulation, most of the incoming light penetrates to the diamond bulk and does not contribute to photocurrent generation, e.g. the large part of the photons (90%) is not effectively used. This can be improved by optimizing the focusing geometry and the diamond material.

Another factor that negatively affects the PCmagnetometer sensitivity is the background signal produced by other defects, such as P1 centers[5], which in our case reduces the contrast by a factor of 10 (see Fig.2). Incorporating a red-laser probe and two-color protocol would reduce this background and improve the magnetic sensitivity[13]. Note that the NV-diamond sample used here had been used previously for the first demonstration of a microwave-free magnetometer [20] that achieved√6nT / Hz noise level. As compared to [20] a portion of the laser light is blocked by the electrodes. Improving the efficiently used photons and the spin contrast would increase the sensitivity. The main focus of this work is to demonstrate an electrical-readout NV-based magnetometer and to discuss the underlying physics and potential routes for improvement, the sensitivity will be optimized in future work.

Summary and outlook.

The experimental results presented in this paper demonstrate electrical detection of cross relaxation processes involving NV centers in bulk diamond. We also report calculated results based on a model[13] that quantitatively describe and explain the experimental data. We anticipate this method, with careful and more sophisticated modelling[13], can be employed for quantitative measurement of photogenerated carriers, which offers a tool to determine of the concen-trations of various defects, including optically inactive P1 centers, paving the way for characterizing local environment information inside diamond lattice.

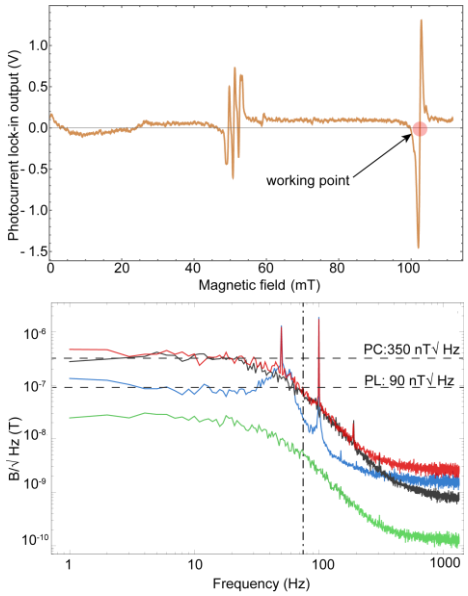

FIG. 4. (a) Demodulated PC signal as a function of axial field along the *z*-axis while modulating the magnetic field. (b) Magnetic field noise spectrum. The red (blue) line indicates the noise in the magnetically sensitive configuration at a magnetic field of 102.4mT for PC(PL) detection, the black (green) line indicates a PC(PL) noise in the magnetically insensitive configuration (bias field ≈ 80mT). The vertical dot line indicates the bandwidth of the magnetometer.

We demonstrate a photoionization-based microwavefree magnetometer based on the GSLAC, which, to the best of our knowledge, is the first demonstration of electric-readout NV magnetometry that provides an alternative to conventional NV-based magnetometers and potentially overcomes some of their limitations. These results open the door to a number of intriguing future directions. First, the electrical readout is compatible with nanoscale electrode structures[10], enabling advances towards integrated large-scale diamond quantum devices. It can be utilized to build scalable sensor arrays[12] and microscopes potentially superior to existing diamond quantum microscopes[25, 26] in terms of resolution. Second, it can be used to build hybrid gradiometers taking advantage of the sensing volume mismatch of PC readout and PL detection. The small sensing volume of the PC detection allows for high spatial resolution while the large sensing volume of the PL detection provides a background measurement in close proximity. Third, while the present studies are focused on diamond, we anticipate comparable behavior in other wide-bandgap semiconductors of technological importance.

Although we observed the magnetic resonances using red laser light (see the supplementary) that excludes the dominant current signal associated with the ionization of P1 centers, we still find a smaller GSLAC contrast[13] for photocurrent measurements in comparison with optical detection. Further studies are necessary to reveal the sources of the remaining background photocurrent.

APPENDIX

A. Experimental setup

Figure1 shows a schematic of the experimental setup. The apparatus includes a custom-built electromagnet. The electromagnet can be moved with a computercontrolled 3-D translation stage (Thorlabs PT3-Z8) and a rotation stage (Thorlabs NR360S, x-axis). The NVdiamond sensor is placed in the center of both the magnetic bore and a pair of integrated Helmholtz coils along the z-axis. The diamond can be rotated also around the z-axis. This provides all degrees of freedom for placing the diamond in the center of the magnet and aligning the NV axis parallel to the magnetic field.

The light source is a solid-state laser emitting at a wavelength of 532nm (Laser Quantum Gem 532). The green laser light propagates through an acousto-optic modulator (AOM) and can be modulated by turning first-order diffraction on and off. The PL emitted by the diamond sample is collected with a 50-mm-focallength lens and detected with a photodetector (Thorlabs APD36A).

B. Diamond sample

The sensor is constructed with a single-crystal [111]cut ($2.1 \times 2.3 \times 0.65$) mm^3 diamond, synthesized using a high-temperature high-pressure (HPHT) method. The initial nitrogen concentration of the sample was specified as <200ppm. To produce NV centers, the sample was electron-irradiated at 14MeV (dose: 10^{18} cm^{-2}) and then annealed at 700 °C for three hours. The resulting NV centers are randomly oriented along all four {111} crystallographic axes of the diamond.

The electrodes for the photoelectric readout were fabricated by means of optical lithography. Prior electrode fabrication the diamond sample was cleaned in oxidizing mixture of H_2SO_4 and KNO_3 at ~250 °C for approximately 30 minutes, after which it was rinsed in deionized water. The electrode structure was placed on the top surface of the diamond. Shape of the electrodes are coplanar interdigitated contacts with a gap of 5μm. The metal stack composition is 20nm titanium covered by 100nm aluminum for wire bonding. The electrodes are bonded to the sample holder (carrier PCB) by a 25-μm-thick aluminum wire.

ACKNOWLEDGEMENTS

The authors acknowledge the assistance by M. Omar and J. Shaji Rebeirro at the early stages of the project. This work was supported by the EU FETOPEN Flagship Project ASTERIQS (action 820394), and the German Federal Ministry of Education and Research (BMBF) within the Quantumtechnologien program (FKZ 13N15064), and the Cluster of Excellence "Precision Physics, Fundamental Interactions, and Structure of Matter" (PRISMA+ EXC 2118/1) funded by the German Research Foundation (DFG) within the German Excellence Strategy (Project ID 39083149). J.H. is a PhD fellow of the Research Foundation - Flanders (FWO). P.S. acknowledges support by BadenWu¨rttemberg Stiftung via

Elite Program for Postdocs. M.N. acknowledges the SBO project DIAQUANT from Flemish fonds for Scientific Research No: S004018N. F.J. acknowledges the European Research Council via Synergy Grant HyperQ, the DFG via excellence cluster EXC 2154 POLiS and CRC1279, and the BMBF.

[1] J. F. Barry, J. M. Schloss, E. Bauch, M. J. Turner, C. A. Hart, L. M. Pham, and R. L. Walsworth, Sensitivity optimization for NV-diamond magnetometry, Rev. Mod. Phys. **92**, 015004 (2020).

[2] A. Reiserer, N. Kalb, M. S. Blok, K. J. van Bemmelen, T. H. Taminiau, R. Hanson, D. J. Twitchen, and M. Markham, Robust quantum-network memory using decoherence-protected subspaces of nuclear spins, Phys. Rev. X **6**, 021040 (2016).

[3] P. Siyushev, M. Nesladek, E. Bourgeois, M. Gulka, J. Hruby, T. Yamamoto, M. Trupke, T. Teraji, J. Isoya, and F. Jelezko, Photoelectrical imaging and coherent spin-state readout of single nitrogen-vacancy centers in diamond, Science **363**, 728 (2019).

[4] M. Doherty, C. A. Meriles, A. Alkauskas, H. Fedder, M. J. Sellars, and N. B. Manson, Towards a room-temperature spin quantum bus in diamond via electron photoionization, transport, and capture, Phys. Rev. X **6**, 041035 (2016).

[5] E. Bourgeois, A. Jarmola, P. Siyushev, M. Gulka, J. Hruby, F. Jelezko, D. Budker, and M. Nesladek, Photoelectric detection of electron spin resonance of nitrogenvacancy centres in diamond, Nat.commun. **6**, 1 (2015).

[6] F. M. Hrubesch, G. Braunbeck, M. Stutzmann, F. Reinhard, and M. S. Brandt, Efficient electrical spin readout of NV^- centers in diamond, Phys. Rev. Lett. **118**, 037601 (2017).

[7] H. Morishita, S. Kobayashi, M. Fujiwara, H. Kato, T. Makino, S. Yamasaki, and N. Mizuochi, Room temperature electrically detected nuclear spin coherence of NV centres in diamond, Sci. Rep. **10**, 1 (2020).

[8] M. Gulka, E. Bourgeois, J. Hruby, P. Siyushev, G. Wachter, F. Aumayr, P. R. Hemmer, A. Gali, F. Jelezko, M. Trupke, and M. Nesladek, Pulsed photoelectric coherent manipulation and detection of N-V center spins in diamond, Phys. Rev. Appl. **7**, 044032 (2017).

[9] V. R. Manfrinato, L. Zhang, D. Su, H. Duan, R. G. Hobbs, E. A. Stach, and K. K. Berggren, Resolution limits of electron-beam lithography toward the atomic scale, Nano letters **13**, 1555 (2013).

[10] M. Gulka, D. Wirtitsch, V. Iva´dy, J. Vodnik, J. Hruby, G. Magchiels, E. Bourgeois, A. Gali, M. Trupke, andM. Nesladek, Room-temperature control and electrical readout of individual nitrogen-vacancy nuclear spins, Nat. Commun. **12**, 4421 (2021).

[11] H. Zheng, Z. Sun, G. Chatzidrosos, C. Zhang, K. Nakamura, H. Sumiya, T. Ohshima, J. Isoya, J. Wrachtrup, A. Wickenbrock, and D. Budker, Microwave-free vector magnetometry with nitrogen-vacancy centers along a single axis in diamond, Phys. Rev. Appl. **13**, 044023 (2020).

[12] E. Bourgeois, M. Gulka, and M. Nesladek, Photoelectric detection and quantum readout of nitrogen-vacancy center spin states in diamond, Adv. Opt. Mater. **8**, 1902132 (2020).

[13] E. Bourgeois, M. Nesladek, *et al.*, work in press.

[14] L. Razinkovas, M. Maciaszek, F. Reinhard, M. W. Doherty, and A. Alkauskas, Photoionization of negatively charged nv centers in diamond: Theory and ab initio calculations, Phys. Rev. B **104**, 235301 (2021).

[15] N. Aslam, G. Waldherr, P. Neumann, F. Jelezko, and J. Wrachtrup, Photo-induced ionization dynamics of
the nitrogen vacancy defect in diamond investigated by single-shot charge state detection, New J. Phys **15**, 013064 (2013).

[16] P. Siyushev, H. Pinto, M. Vo¨ro¨s, A. Gali, F. Jelezko, and J. Wrachtrup, Optically controlled switching of the charge state of a single nitrogen-vacancy center in diamond at cryogenic temperatures, Phys. Rev. Lett. **110**, 167402 (2013).

[17] N. B. Manson, M. Hedges, M. S. Barson, R. Ahlefeldt, M. W. Doherty, H. Abe, T. Ohshima, and M. J. Sellars, NV—N+ pair centre in 1b diamond, New J. Phys **20**,
113037 (2018).

[18] V. Iva´dy, H. Zheng, A. Wickenbrock, L. Bougas, G. Chatzidrosos, K. Nakamura, H. Sumiya, T. Ohshima,J. Isoya, D. Budker, and A. Gali, Photoluminescence at the ground-state level anticrossing of the nitrogenvacancy center in diamond: A comprehensive study, Phys. Rev. B **103**, 035307 (2021).

[19] S. Pezzagna and J. Meijer, Quantum computer based on color centers in diamond, Appl. Phys. Rev. **8**, 011308
(2021).

[20] A. Wickenbrock, H. Zheng, L. Bougas, N. Leefer, S. Afach, A. Jarmola, V. M. Acosta, and D. Budker, Microwave-free magnetometry with nitrogen-vacancy centers in diamond, App. Phys. Lett. **109**, 053505 (2016).

[21] L. T. Hall, P. Kehayias, D. A. Simpson, A. Jarmola, A. Stacey, D. Budker, and L. C. L. Hollenberg, Detection of nanoscale electron spin resonance spectra demonstrated using nitrogen-vacancy centre probes in diamond, Nat. Commun. **7** (2016).

[22] J. D. A. Wood, D. A. Broadway, L. T. Hall, A. Stacey, D. A. Simpson, J.-P. Tetienne, and L. C. L. Hollenberg, Wide-band nanoscale magnetic resonance spectroscopy using quantum relaxation of a single spin in diamond, Phys. Rev. B **94**, 155402 (2016).

[23] M. Auzinsh, A. Berzins, D. Budker, L. Busaite, R. Ferber, F. Gahbauer, R. Lazda, A. Wickenbrock, and H. Zheng, Hyperfine level structure in nitrogen-vacancy centers near the ground-state level anticrossing, Phys. Rev. B **100**, 075204 (2019).

[24] R. Lazda, L. Busaite, A. Berzins, J. Smits, M. Auzinsh, D. Budker, R. Ferber, and F. Gahbauer, Cross-relaxation studies with optically detected magnetic resonances in nitrogen-vacancy centers in diamond in an external magnetic field, arXiv preprint arXiv:2007.00473 (2020).

[25] D. R. Glenn, R. R. Fu, P. Kehayias, D. Le Sage, E. A. Lima, B. P. Weiss, and R. L. Walsworth, Micrometerscale magnetic imaging of geological samples using a quantum diamond microscope, Geochemistry, Geophysics, Geosystems **18**, 3254 (2017).

7. Chapter 7 - OSCAR-QUBE: Integrated diamond-based quantum magnetic field sensor for space applications

Authors contribution: I was main author of this proceedings paper as well as team leader, system engineer and project manager of project OSCAR-QUBE. I contributed at each step of this paper and realization. This paper and the work done within the OSCAR project series represents the exploration of the application potential of this technology in the harsh space environmental conditions.

Proceedings - 2021, 72nd International Astronautical Congress, Dubai, UAE

IAC-21,E2,3-GTS.4,13,x66880

OSCAR-QUBE: Integrated Diamond-Based Quantum Magnetic Field Sensor for Space Applications

Jaroslav Hruby[ab]*, Siemen Achten[a], Musa Aydogan[a], Sam Bammens[a], Yarne Beerden[a], Boo Carmans[a], Dries Hendrikx[a], Jeffrey Gorissen[a], Teoman Köseoglu[a], Jens Mannaerts[a], Remy Vandebosch[ab], Siemen Vandervoort[a], Sebastiaan Vanspauwen[a], and Milos Nesladek[ab]

[a] Institute for Materials Research (IMO), Hasselt University, Wetenschapspark 1, B-3590 Diepenbeek, Belgium.

[b] IMOMEC Division, IMEC, Wetenschapspark 1, B-3590 Diepenbeek, Belgium.

Corresponding Author jaroslav.hruby@uhasselt.be

Abstract

The diverse application opportunities, high sensitivity, precision and the enabling of various measurement protocols have raised the attention of novel quantum sensing methods. One of the promising quantum sensing platforms nowadays is the nitrogen-vacancy (NV) centre, an opto-magnetic defect located in the diamond's crystalline lattice, that can be exploited as a solid-state qubit at room temperature. The combination of diamond and NV centres make it an ideal candidate for magnetic field sensing in harsh conditions as well as a steppingstone to bring quantum technology to everyday use, with numerous applications in the field of geophysics, healthcare, and aerospace. The OSCAR-QUBE team consists of 13 interdisciplinary students who developed a portable NV-diamond based quantum magnetometer for space applications. The project was selected for the 'Orbit Your Thesis!' programme organised by the European Space Agency in April 2020. With this the team had won the opportunity to send their device to the International Space Station (ISS). In September 2021 the device was successfully commissioned onboard the ISS. This work aims to describe the results of the OSCAR-QUBE mission, which is proving the viability of this novel technology in a space environment, by collecting magnetic field data in Low Earth Orbit in order to construct a magnetic field map of the Earth. The

sensor is installed inside of the ICE Cubes Facility, in the Columbus module in a form factor of 1U, weighing 420 grams, with a power consumption of 5W. The target sensitivity for this demonstration is 1nT with a dynamic range of up to 1mT, together with pulsed measurement protocols allowing for improvements in sensitivity and enabling novel sensing techniques. This mission is a steppingstone in moving the boundaries of current day sensing technology enabling further space exploration but also in the process of paving the way toward everyday quantum applications. Addressing the challenges of a wide range of applications in space and on Earth, such as the measurements of bio-potentials, space weather monitoring, navigation, mineral exploration, or onboard sample analysis. This student made magnetometer aims towards becoming a beacon of inspiration for the next generation of young science and engineering students.

Keywords: NV centre, diamond, magnetometry, ISS, 'Orbit Your Thesis!', quantum sensing

1. Introduction

The emerging field of quantum sensing has become a distinct and rapidly growing branch of quantum science and technology. While opening new horizons in terms of high sensitivity, wide dynamic range, and precision, it is enabling novel measurement protocols and bringing new possibilities to view the world around us. Nowadays, various physical quantities can be measured by means of quantum sensing, for example time and frequency, temperature, pressure, electric or magnetic fields. [1]

Historically the challenge of quantum systems often lied in the requirement of cryogenic temperatures for its operation, leading to their bulky size (i.e., SQUID)[2] limiting its portability and application potential. One of the intriguing quantum platforms addressing the portability issues is the nitrogen-vacancy (NV) centre, an opto-magnetic defect located in the diamond's crystalline lattice which can be used in next-generation magnetic field sensors. The NV centre-based magnetometers can operate in room temperature and the smallest sensing unit is a single NV centre enabling significant miniaturization potential. [3], [4]

Project OSCAR-QUBE (**O**ptical **S**ensors based on **CAR**bon materials: **QU**antum **BE**lgium) is a team of 13 interdisciplinary students of science and engineering that developed a portable diamond-based quantum magnetic field sensor. The project was selected in the framework of the 'Orbit Your Thesis!' educational programme [5] in April 2020 by the European Space Agency to develop an experiment that will map the magnetic field of the Earth onboard the International Space Station (ISS). The instrument was successfully launched and has been operational since September 2021. It will operate over the course of 10 months onboard the ISS. Magnetometers have a wide range of terrestrial applications, such as bio-signal measurements navigation, mineral exploration, or sample analysis. In the field of aerospace, magnetometry can be used to determine the attitude of the aircraft or spacecraft. They can also be used for spacecraft in-flight analysis, or for scientific applications such as space weather monitoring, planetary observation, or space exploration. [6]–[10]

The measured magnetic field in Low Earth Orbit (LEO) is a complex superposition of fields [11] produced by multiple phenomena. They can be internal (originating from Earth), such as planet core activity, the lithospheric movements affecting distribution of ferromagnetic rocks, and significant concentrations of iron ore in the soil; or they can be external, such as space weather and artificial fields from onboard spacecraft itself. All of the individual sources can be characterized by different temporal and spatial scales, which can be used to distinguish between them. [12], [13]

1.1 NV centres overview and fabrication

Diamond can contain a variety of defects in its crystalline lattice. One of them - the NV centre can be exploited as an opto-magnetic probe, enabling diamond-based magnetometry. It consists of a nitrogen atom (N) coupled to a vacancy (V) and have been described to this day in two configurations (see Fig. **34**a) - a neutral state NV centre (NV^0) and a negatively charged state NV centre (NV^-). The properties of these two variants differ from each other significantly, and only negatively charged NV centres can be used in magnetometry as the principles of operation are based on the spin dependent dynamics of the single electron. [3] The NV centres are a solid-state quantum magnetic probe with high spin coherence, facilitating magnetic field sensitivities theoretically down to ~50 $fTHz^{-1/2}$. [3], [14]

The NV centres can occur in the diamond naturally, but for purposes of quantum sensing they are specifically engineered. One of the possible ways to fabricate samples with a high density of NV centres, requires type 1b diamonds. [15] These diamonds contain nitrogen impurities in concentration levels reaching up to 0.3%. [16] The NV centres are fabricated by irradiating the 1b diamond with electrons, after which annealing step is performed. The sample is heated to the annealing temperature which stimulates migration of vacancies towards substitutional nitrogen leading to formation of the NV centres. [17] This is typically done at temperatures ranging from 800°C to 2000°C, while pressures range from vacuum to 8 GPa. [16], [18]

1.2 Optically Detected Magnetic Resonance

The electron of an NV centre exists in a spin-triplet ground state (see Fig. 34b). It features three magnetic spin states, ±1 and 0. An electron residing in the ground state ($^3A_2$) can be excited to an excitation state (^3E) by a green (532 nm) photon. When the electron degrades back to the ground state, this coincides with the release of a red (637 nm) photon. Under stable conditions, this emission of red photons is constant and resistant to photobleaching. By applying a microwave (MW) field of resonance frequency (f_0) to the NV centres, the electron with positive-negative ($m_s=\pm1$) spin can perform a transition via the metastable state (^1A). This transition is non-luminescent and is enabled by the MW providing sufficient energy to the electron for transition through the metastable state, resulting in a decrease in the red luminescence (see Fig. 34c). The resonant frequency f_0 in standard conditions is 2.87 GHz.[3], [14], [19]

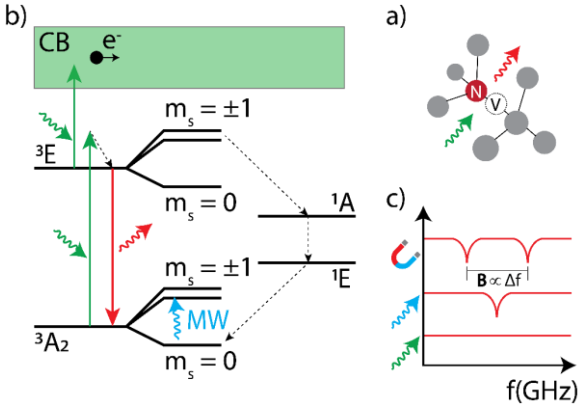

Fig. 34. a) NV centre atomic structure in diamond lattice b) Energy level diagram of the negatively charged NV centre, showing transitions responsible for ODMR and PDMR contrast. c) Schematic representation of detected signal upon green light excitation, after application of microwave field, and splitting caused by an external magnetic field

The optical readout technique for NV spin utilizes the red photoluminescence light being released from the NV^- during their excitation. A green laser is typically used to drive the excitation process. The intensity of the red photon release provides details on the spin states of the electron triplet ground state within the NV^-. [20] This method is called Optical Detection of Magnetic Resonance (ODMR). [3], [14], [21]

1.3 Photoelectrically Detected Magnetic Resonance

A recently published alternative method for addressing NV centres is called Photoelectric Detection of Magnetic Resonance (PDMR). [22] It relies on the photoelectric readout principle, where a two-step photoionization process excites electrons of the NV centre to the conduction band, where they can be detected as a photocurrent. This working principle can be seen in Fig. 34b.

The main advantage of the PDMR technique is a higher collection efficiency and the absence of the optical detection path. This is leading to improvement in sensitivity and further miniaturization of this technology. To enable the photocurrent readout, electrodes are fabricated on top of the diamond surface by means of optical lithography. Relative to ODMR, the photon-collection process has limited efficiency due to photons being emitted in all directions, allowing only a small portion to be effectively collected by the photodetector. On the other hand, the PDMR saturation is defined by the time needed for recombination to occur in the charge carrier. This leads to enhancements in the detection rates for PDMR based measurement techniques. The improvement of the detection rates adds up to $\approx 2.5 \times 10^2$ times that of ODMR. [23] For the linewidth, PDMR is dependent on the spin coherence properties of the diamond sample itself. [22]–[24]

1.4 NV based magnetometry

When an external magnetic field is applied to the diamond with NV centres, Zeeman splitting effect occurs. Besides the magnitude of the spin (0; 1), the direction (0; -1,0,1) also becomes relevant. Microwaves can now be used to bring the spin-zero system either to a spin |+1> or |-1>. The two resonances can now be observed in the spectrum (see Fig. 34c). The observed splitting corresponding to Δf is linearly proportional to the magnetic field applied. The magnitude of the magnetic field along the NV axis can be determined by the equation below:

$$\Delta f = 2\gamma \vec{B} \cdot \hat{V}(nv) \qquad \text{[25] (5)}$$

Where γ is the gyromagnetic ratio, B is the applied magnetic field and V$\hat{}$ stands for the unit vector of each one of the NV-axes.

NV centres can occur in four different directions, defined by the tetrahedral structure of the diamond lattice. The four directions form an overcomplete basis, wherein the direction of each crystallographic unit vector is purely determined by geometry and can be precisely specified. This means that diamond-based magnetometers are intrinsically vectoral in nature and can be used to determine the 3D magnetic field. The NV centres are situated along not just one, but four directions, which means that a properly split resonance spectrum will contain eight resonances. The magnetic field sensitivity of the continuous wave (CW) measuring method can be determined by the equation below:

$$\eta_{CW} = \frac{4}{3\sqrt{3}} \frac{h}{g_e \mu_B} \frac{\Delta v}{C_{CW}\sqrt{R}} \qquad \text{[3] (6)}$$

where g_e = 2.003 is the electronic g-factor of the NV centre, v the linewidth, C_{CW} the contrast, and R the photon (or electron) detection rate.

Fundamental limitations are placed on the sensitivity by the quantum noise linked to spin projection. This characteristic is shared by all spin-based magnetometers and is caused by the statistical nature of quantum measurements. PDMR provides some advantages in this case, since photon shot noise adds to spin projection noise when the readout is performed optically. The CW sensitivity has not yet reached the fundamental spin projection limit and higher sensitivities are conventionally acquired using pulsed approaches.

1.5 Pulsed magnetometry

Pulsed magnetometry can enable more advanced quantum operation modes [26]. There exist a variety of possible pulse sequences, enabling nearly T2*-limited measurements by avoiding the power broadening of the spin resonance spectrum recorded. Separation of the laser spin polarisation pulse and the MW spin driving pulse allows achieving a high spin contrast and using various spin manipulation and readout protocols enabling an increase of the detection sensitivity by measuring phase changes in the spin precession.

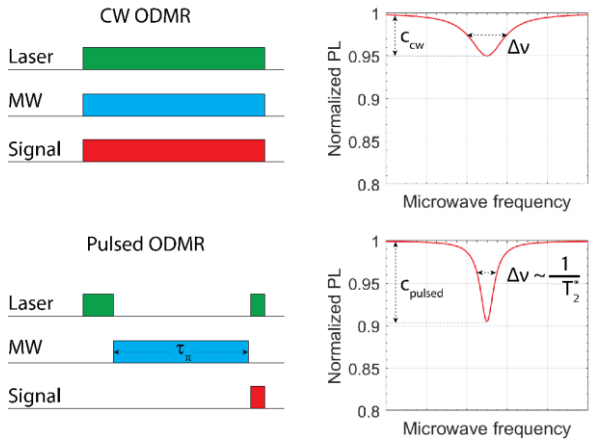

Fig. 35. Comparison of continuous wave (CW) and pulsed ODMR. The advantage of the pulsed method is higher contrast and narrow line width due to the power broadening mechanism.

A simple pulse sequence is called *Pulsed ODMR* and is shown in Fig. 35. As the laser and microwaves are no longer used in parallel, higher optical intensities can be used without significant reduction of the contrast. Together with a reduction in linewidth, this increases the sensitivity as compared to CW ODMR.

Two other elementary pulse sequences are the Ramsey and Hahn echo schemes, both are aimed at different applications. They are both based on the measurement of the phase accumulation of the electron spin with respect to its initial spin-zero state, which is proportional to the ambient magnetic field. The Ramsey scheme is typically used to measure DC fields; simultaneously present AC fields are not picked up, as the positive and negative contributions of these fields approximately cancel each other out. The Hahn echo sequence features an extra pulse as compared to the Ramsey scheme, which allows for phase-sensitive lock-in-type measurements of AC fields. This frequency-locking technique can help in the differentiation and decoupling of two or more signals. To further improve equivalent noise bandwidth and to decouple two signals of similar frequency more advanced methods such as CPMG or xy8 can be implemented.

2. Material and methods

For its ten months mission, our instrument is located onboard of the ISS since September 2021. More specifically, installed inside the ICE Cubes Facility (ICF), which is in the EPM rack of Columbus module (see Fig. 36b). The ICF provides the OSCAR-QUBE device with housing, electrical power to operate and Ethernet connectivity for the transfer of acquired Earth's magnetic field to the ground station. The device has form factor of 1U cube (10x 10 x 10 cm).

2.1 System overview

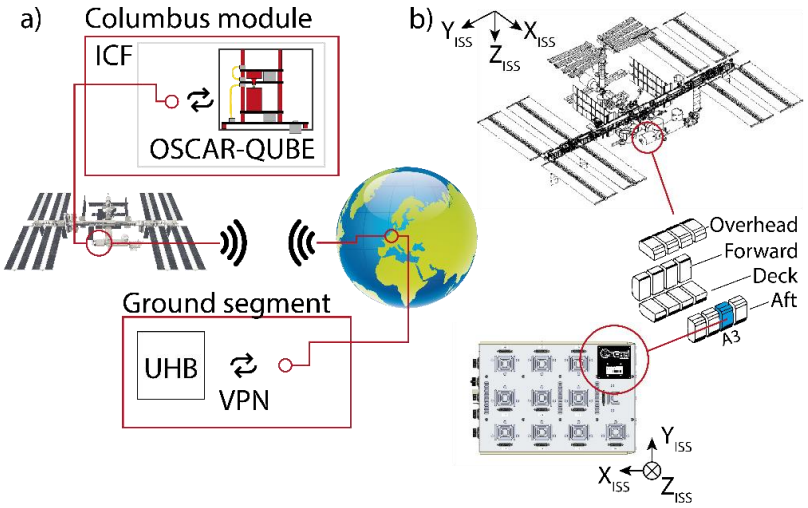

Fig. 36. a) Global system overview b) Reference frames of the OSCAR-QUBEs respective location onboard the ISS

The cube is mounted to the ICF via the DB13WB3 connector, providing our magnetometer with +5 V, +12 V and an Ethernet interface. After the data packets are transmitted, it is routed through the Ice Cubes Mission Control Centre (ICMCC) in Zaventem, Belgium towards the User Home Base (UHB), located on the premises of research institute IMO-IMOMEC (UHasselt). The connection to the ICMCC network is through a secure VPN tunnel. Once connected, the ICMCC will act as a relay station between the OSCAR-QUBE onboard the ISS and the UHB

2.2 System layout

The experiment can be viewed as a set of interconnected subsystems (shown in Fig. 37), designed for diamond quantum magnetometry are laser, microwave, and readout subsystems, accompanied with power distribution, and control subsystems required for the autonomous operation onboard the station. And reference subsystem for status monitoring and further data analysis.

The power subsystem handles the power conversion and power management within the system and provides galvanic isolation from the ICF. It transforms the voltages provided by ICF to suit the needs of the rest of the system.

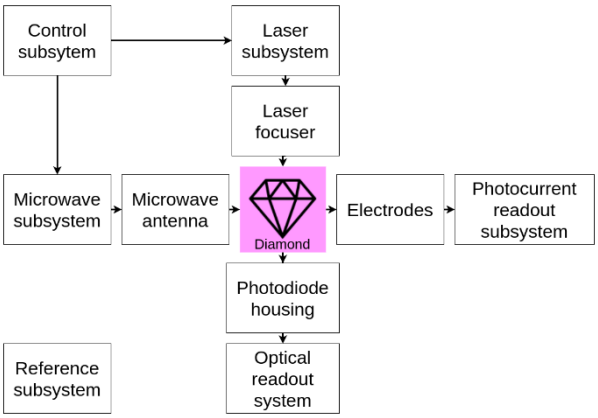

Fig. 37. System layout with an overview of the individual subsystems

The control subsystem's task is to manage the low-level communication between subsystems, facilitate the data acquisition, data storage and packetization, system operation and communication with the UHB. The control subsystem consists of a microcontroller unit (STM32F7, STMicroelectronics) and FPGA (Artix A7, Xilinx) which is used for advanced pulsed measurements. Another important part of the control subsystem is the SD-card which is used for temporary data storage to prevent the data loss during a Loss of Signal (LOS) period.

The reference subsystem consists of a series of sensors to measure parameters related to the environment and system monitoring, such as the temperature of the MCU and of the laser. To monitor the environment, an accelerometer and gyroscope (LSM6DS33TR, STMicroelectronics) are used to detect possible shocks or vibrations in the vicinity of the instrument. Lastly, the reference magnetometer (LSM303AGRTR, STMicroelectronics) is also part of the reference subsystem to have a baseline comparison for the data measured with the developed system.

For excitation of the NV centres in the diamond sample the laser subsystem is used. The laser is a 532 nm laser diode (L520P50, Thorlabs) that is controlled by a laser driver (IC Haus, IC-NZN QFN24-4X4). To adjust the laser output power, a programmable resistor is interfaced with the laser driver providing the possibility to control this system remotely, allowing adjustment of the parameters onboard the ISS. To enable the advanced quantum operations the laser subsystem can be modulated by TTL signal from the control subsystem.

After excitation the NV centre transition is driven by microwave fields of sweeping frequency synthesized by the microwave subsystem. The frequency range of the microwave signal generated by a programmable PLL (ADF4351, Analog Devices) is between 2.6 and 3.2 GHz, with power output ranging from -31.5 to +25 dBm, adjustable by attenuator (HMC624, Analog Devices). This subsystem is equipped with a microwave switch (M3SWA-50_DRB+, Minicircuits) opening the possibility of pulsed operation.

The readout subsystem was designed to enable both readout methods – ODMR and PDMR at the same time. The optical readout subsystem collects the red photons emitted from the diamond by a photodiode. The red-light signal is then amplified and acquired by Analog-Digital-Converter (ADC, ADS8691, Analog Devices). The photoelectric part of the readout subsystem collects the photocurrent originating directly from the NV centres via electrodes fabricated on the diamond surface. The photoelectrons are collected, and analogically to the optical readout, amplified and digitized. The optical path allowing the readout is described in the chapter below.

2.3 Laser focuser and photodiode housing

For optimal focusing of the laser beam at the diamond sample, and collection of the signal coming from the NV centres an optical path composed of a laser focusing unit and photodiode housing was designed (see Fig. 38a). This system allows accurate micrometric adjustments of the beam positioning, which is essential for focusing the green excitation light between a pair of line electrodes with a gap of 5 µm (see Fig. 38b). All the mechanical parts of the optical path were designed by the team to maintain the small footprint of 30 x 18 mm. The laser focuser part consists of two lenses - collimation lens (CAY046, Thorlabs) and focusing lens (APL0303, Thorlabs). The first is to collimate the laser beam and the second to focus the beam onto the diamond between the electrodes. The collimation lens is adjustable in Z direction. The focusing lens is adjustable in X, Y and Z direction.

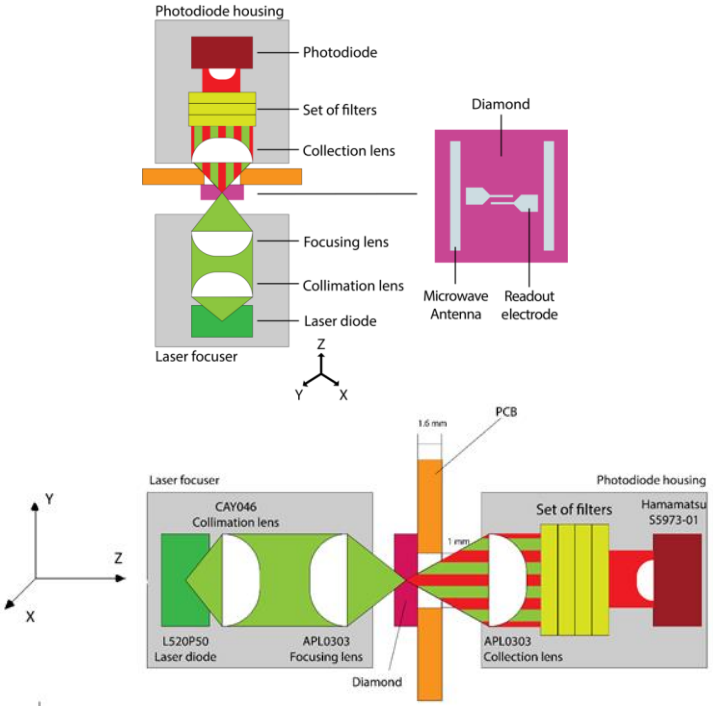

Fig. 38. Schematic representation of the diamond magnetometer (up) optical path and (bottom) sample with antenna and electrodes fabricated on the surface

The red emission light from diamond is collected by the photodiode with an integrated lens (S5973-01, Hamamatsu) mounted in the housing. This part is built out of a collection lens (APL0303, Thorlabs) and a cut-off filter (FELH0650, Thorlabs) to filter out the unwanted wavelengths out of the signal which is collected by the photodiode.

2.4 Diamond sample

The core of the quantum magnetometry system is a diamond sample. The quality and characteristics of the diamond directly determines the performance of the system. In this work a CVD grown, electron irradiated single crystal diamond with [100] orientation (Element Six) is used. The substrate dimensions are 2.6 x 2.6 x 0.4 mm and high NV concentration (2 ppm). The sample is equipped with electrodes and a microwave antenna fabricated on top of the diamond surface by optical lithography. The electrode pair used for photoelectric readout consists of two parallel lines separated by a gap of 5 µm (see Fig. 38b). The microwave antenna enables direct application of the microwave field to the sample, which minimizes the losses in field strength and improves the signal contrast.

2.5 Magnetic field calculation from NV centre signal

The direction of the magnetic field vector is important information in determining the magnetic field source(s). The incoming magnetic field in the NV reference frame has to be expressed in respect to the reference frame of the ISS. Since the location of the OSCAR-QUBE device within the ISS reference frame is known (see Fig. 36b), using linear algebra, the NV-axes can be expressed in the ISS reference frame. To get the components of the magnetic field measured by our device, a system of equations needs to be solved in which formula X is generalized to include all four NV-axes. This matrix equation is shown below.

$$2\gamma \begin{bmatrix} X_{NV1} & Y_{NV1} & Z_{NV1} \\ X_{NV2} & Y_{NV2} & Z_{NV2} \\ X_{NV3} & Y_{NV3} & Z_{NV3} \\ X_{NV4} & Y_{NV4} & Z_{NV4} \end{bmatrix} \cdot \begin{bmatrix} B_x \\ B_y \\ B_z \end{bmatrix} = \begin{bmatrix} \Delta f_1 \\ \Delta f_2 \\ \Delta f_3 \\ \Delta f_4 \end{bmatrix} \tag{7}$$

By solving this matrix equation, the components Bx, By, and Bz can be calculated. With this information, a magnetic field around the earth can be reconstructed. [25] The result can afterwards be matched with positioning and attitude data of the ISS to express the magnetic field vector in a local coordinate system. This method allows the exact determination of the vector magnetic field orientation.

2.6 Testing and environmental requirements
To develop an instrument capable to withstand space conditions (such as launch, or microgravity) while being safe for the operation onboard the ISS, various requirements must be met. The mechanical and structural stability, compliance with EMC/EMI standards, surface temperature limits, and compatibility with existing interfaces were the main subjects of testing. The testing was done in multiple locations and test centres. The thermal and vacuum testing was done at the Hasselt University (Belgium), EMC/EMI tests at KU Leuven (Campus Brugge, Belgium), vibration test campaign was conducted at ESA ESEC Galaxia (Redu, Belgium) and the interface tests at Space Application Services (Zaventem, Belgium)

3. Experimental part

The development of the instrument was done in two stages –test bench development phase and protoflight model (PFM) development phase. The test bench model approach was chosen to develop and test all the subsystems before the integration to one system, to reduce the complexity during the development. Each subsystem developed for testbench had its own MCU for individual software and dedicated libraries development. This approach proved to be efficient in terms of failure analysis and parameter optimization, as well as reducing the time of software development.

All the PCBs were designed using the Altium software suite and assembled by the team. The aluminium structures of the enclosure and the laser focuser with photodiode housing were both designed in Autodesk Fusion 360 and manufactured at the university workshop. After subsystem optimization and re-iteration period on the testbench, protoflight development phase was initiated. In this phase all the subsystems were combined into a single closely integrated system that could be controlled over Ethernet. There were two identical PFM models (PFM#1 and PFM#2) developed with the aim to benchmark two different diamond samples in the integrated device. The PFM#2 showed to contain sample with higher sensitivity. While the PFM#1 became a ground model and subject of long-term software stability testing. After the deployment of the final version of the software, the PFM#1 was tested for functionality in the period of 4 months without interruption to verify the system stability of the minimum mission requirement. The PFM#2 was selected to undergo the environmental testing and was chosen as the flight model to be sent to the ISS.

3.1 Operations and automation

The QUBE is operated from the User Home Base (UHB). This is a desktop computer which connected to the system onboard the ISS using a secure VPN tunnel, provided by Space Application Services. The data communication protocol is UDP due to its smaller header size, reducing the bandwidth use. The UHB contains two main parts composing mission control software (MCS). The first part is the MCS called 'Yamcs'. The MCS functions as the backbone of the UHB and is designed to receive telemetry (TM) and send telecommands (TC), while storing the raw incoming packets and formatting them into 'human friendly' values. The processed data is then visualized by the second segment of the UHB – Graphical User Interface (GUI). The GUI was created as a Python script with pyQt5 and is the main access point for the operator to interact with the system.

The UHB provides operators with all the commanding and monitoring options necessary to control the QUBE. The emphasis was put on the user experience and fail-safe operation, allowing all the team members to operate the system when needed. The GUI visualizes the incoming TM in a comprehensible format which enables the operator to swiftly interpret the data and respond accordingly to the events. The operator can issue pre-set TC using buttons of the GUI. Additionally, the GUI also contains automated features, such as LOS recognition ensuring no data is lost in this period, or during unexpected situations. The LOS detection thread is responsible for periodic sending of low volume TC to the QUBE. When the connection is not available and no TC will arrive at the QUBE for a period of 10s, it will evaluate the situation as LOS and will initiate the temporary storage of packets to the SD card. When the device is reachable again (AOS, Acquisition of Signal) it will start transmitting the stored packets to the UHB. This system ensures no data is lost in case of LOS or other events in which the connection with the UHB is lost. In post processing a timestamp parameter of the TM data is used to chronologically order the packets.

3.1 Device testing
To prove the compliance of the device with the environment and to verify its functionality, it underwent a series of tests listed below.

3.1.1 Magnetic field sensitivity testing
The magnetic field sensitivity is defined with two parameters, angle of precision and the magnetic field strength sensitivity. Both parameters were measured to determine the sensitivity of the cube. but first the device had to be calibrated.

To calibrate the device, ODMR spectra were recorded as a function of various magnetic field vectors. The first step in the calibration process was to apply well defined magnetic field vectors by 3-axial Helmholtz coil. This fully symmetric Helmholtz coil consisted of three parallel coil pairs and was able to produce magnetic fields of intensity up to 38μT in each axis. Using the Helmholtz coil setup, the NV-axes of the sample were determined by applying different magnetic field vectors. This allowed us to verify the 3D magnetometry measurements procedure and by varying the current it was possible to describe the response of the system to both the AC and DC magnetic field.

With the device calibrated, the angle of precision and the magnetic field sensitivity could be determined. For the magnetic field sensitivity, a Power Spectrum Density (PSD) of the measured magnetic field noise is plotted to determine the noise floor and thereby the sensitivity. The angle of precision on the other hand is determined from the angle deviation that is observed when the NV-axis is aligned perpendicular with the magnetic field vector generated by the Helmholtz coil.

3.1.2 Structural (vibration) testing

During the launch of the experiment, it was exposed to vibrations and forces coming from the rocket. To analyse that the experiment would not be compromised due to these forces a set of simulations was performed verify that the experiment structure design is well suited for the mission. Among these simulations are modal analyses (lowest modal frequency at 244.3 Hz) to give insight into how the experiment reacts to vibrations, static stress analyses from which margins of safety were calculated (lowest margin of safety 3.62), which gave confidence in the structural integrity of the experiment and a stress-life fatigue analysis (minimum lifetime of 1 billion cycles) which ensures the experiment will not fail due to stress cycling.

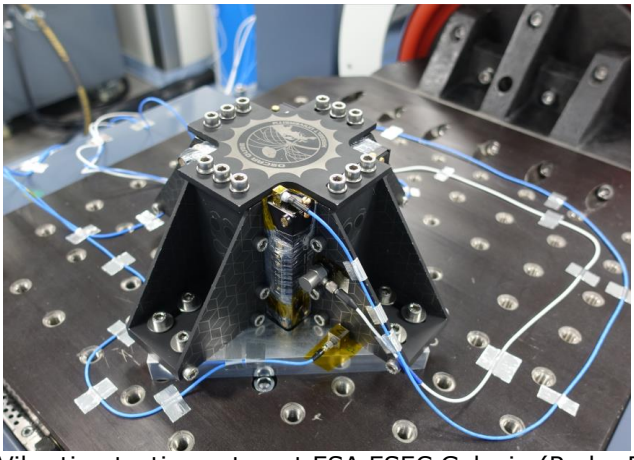

Fig. 39. Vibration testing setup at ESA ESEC Galaxia (Redu, Belgium)

After these simulations had all proven to be positive the experiment was built and taken to ESA ESEC which has a facility specifically made for the testing of CubeSats. Among the many possibilities there it was possible to do real life vibration testing on the experiment. The setup is shown in Fig. 39. During this testing the experiment was subjected to the vibration on the shaker test bench, which is equivalent to forces on board of the rocket during the launch event. With this testing it was proven that the vibrations have no significant impact on the safety or functionality of the experiment. The combined results of the real-life testing and the simulations that were performed show that the experiment is very well designed to satisfy the mission requirements.

3.1.3 EMC/EMI testing

The EMI/EMC tests were conducted in a semi-anechoic chamber. Which functions as a faraday cage covered with ferrite tiles, RF absorbers and is equipped with waveguides for cabling to provide isolation from external influences on the measurements. The test setups were built according to the requirements on E-field and B-field radiated emissions.

Fig. 40. EMC/EMI testing

The E-field Radiated Emission were measured in ranges between 10kHz and 900 MHz (< 60 dBµV/m), between 1GHz and 10GHz (< 80 dBµV/m) and for the frequency notch from 2.2 to 2.4 GHz (< 55 dBµV/m). The test method used for verification of this requirement is RE102 from the US Military EMC standard, MIL-STD-462. [27]

The B-Field emissions were tested during all operation modes, AC magnetic field emissions measured at 7cm from the Experiment Cube (on all six sides) did not exceed the limits in the frequency range 30 Hz to 250 kHz. The emission limit was studied at 30 Hz, and measured values did not exceed 140 dBpT, between 3.5 kHz and 250 kHz the value did not exceed the limit of 85 dBpT. The test method used for verification of abovementioned requirements is RE101, from the standard MIL-STD-462. [27]

The E-field measurements were performed in the full compliance with the frequency range as specified in the requirements, the B-field measurements were only performed between 9kHz and 250 kHz. This limitation was still acceptable as the experiment cube does not contain any large inductive loads and a requirement deviation was issued. The loop antenna was used to measure the B-field emission on all 6 sides.

3.1.4 Thermal testing

The OSCAR-QUBE device has to meet all safety requirements when exposed to temperatures ranging from +5 to +46.1°C. Furthermore, under all modes of operation, the OSCAR-QUBE cannot have external surfaces exceeding a temperature of 45.8°C.

During operation in microgravity, the OSCAR-QUBE is exposed to an environment where heat transfer from the device to the air by convection and conduction is reduced. The thermal behaviour in a vacuum, where there is no convection due to the lack of a medium, was appropriate to simulate thermal behaviour of the instrument in microgravity.

The lack of convection limits the cooling efficiency and can lead to an increase of temperature. However, while the OSCAR-QUBE instrument is installed in the ICF it is cooled by the forced airflow. To verify that the OSCAR-QUBE can function in the simulated 'worst case scenario' conditions without exceeding its safety limits, it was tested in a vacuum of 0.68 millibar at an initial temperature of 22°C.

Before operating in a vacuum, a reference measurement was performed in ambient pressure at full optical laser output power (~50 mW output laser power). The highest temperature on the laser, according to the readout, reached 40°C. According to the FLIR camera used, the hottest point was 42.7°C. This difference can be accounted for by the placement of the temperature sensor and by the laser housing acting as a heat sink. The outside of the OSCAR-QUBE reached maximum of 28°C.

Fig. 41 shows a regular image on top with a FLIR image on the bottom with a similar perspective. The OSCAR-QUBE was tested in a (medium) vacuum of 68 Pa.)

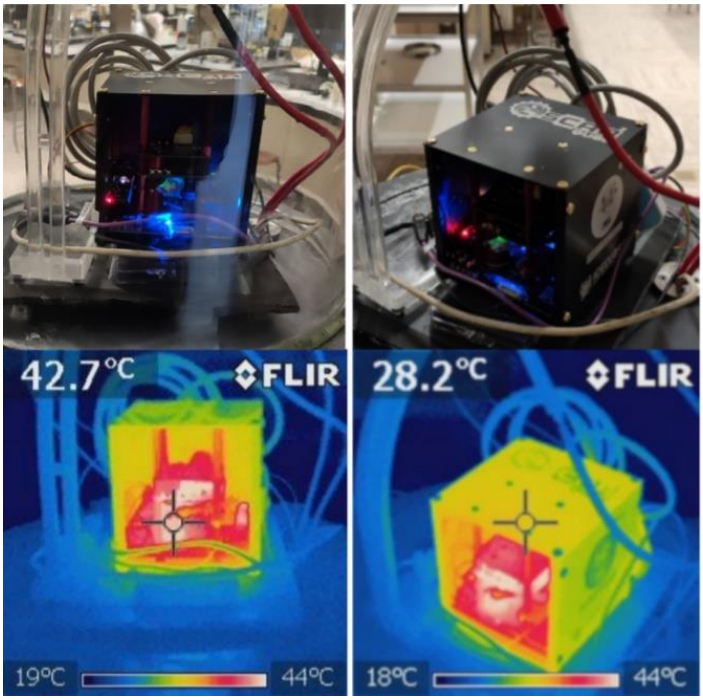

Fig. 41. Vacuum test setup for thermal behaviour. Left) a frontal perspective is shown to measure the inside temperature. Right) an angled perspective is shown to measure the outside temperature.

After the vacuum tests were concluded, the QUBE was re-pressurized to measure the thermal behaviour with the FLIR camera.

In Fig. 41, the highest recorded temperature was 64.4°C on the laser housing and 60°C on the control board. The highest touch temperature immediately after re-pressurization was 38°C.

3.1.5 Interface testing

Before launching the instrument to the International Space Station, an interface test was done inside the ground model of the ICE Cubes Facility (ICF), an exact replica of the device that is installed inside the Columbus module of the ISS. All hardware and software functionalities were tested to demonstrate proper operation. After a visual inspection, physical inspection, and electrical tests, the experiment cube was plugged into the ICF and was powered. The ICF recognized the QUBE and was followed by the communications test via the UHB.

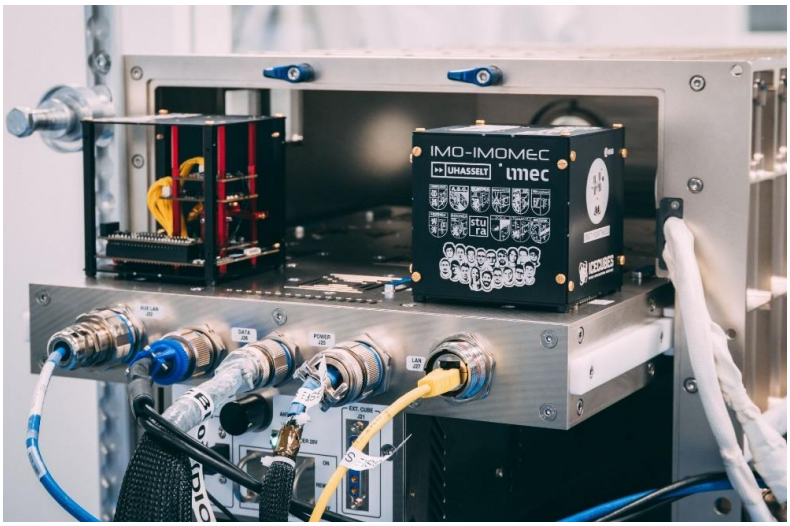

Fig. 42. Interface tests on a ground model of ICE Cubes Facility (Zaventem, Belgium), left device is a ground model and right device is a flight model of OSCAR-QUBE instrument

Results and Discussion

The QUBE was launched on the 29th of August and installed on the 2nd of September. Upon its commissioning, it started sending real-time data to the UHB through the ICMCC relay. After 10 seconds of operation, the QUBE was sending the data to the UHB as expected. This behaviour confirmed the autonomous (ping) routine of the UHB was executing properly, and the sent telecommands could reach the QUBE. The TCs were further validated by reconfiguring the settings of the QUBE and confirming the changes using the TM data visualised in the GUI. These actions were performed without a noticeable delay between issuing the TC and seeing the reaction in the TM data. The ping response times were around 800 ms.

LOS handling is working as expected. The QUBE automatically detects the loss of the pings and initiates the data storage procedure to buffer the TM temporarily on the SD-card. Once the AOS is re-established, the device begins to autonomously dump the saved data to the UHB.

4.1 Mechanical results – optical stability

The system was carefully assembled using the subsystems described before. The resulting device is shown in Fig. 43. The system has experienced less than 3% of optical signal degradation since the shipping of the QUBE. This can also be seen in Fig. 44, the splitting onboard the ISS.

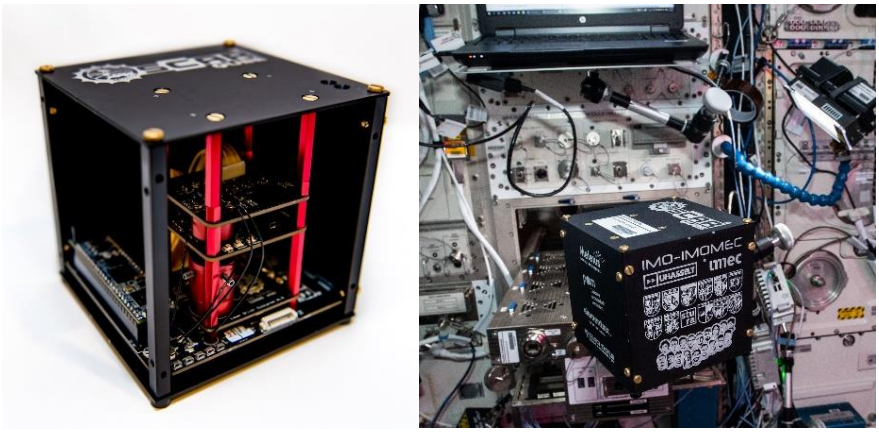

Fig. 43. Left) The completely assembled device without the side panels. Right) The OSCAR-QUBE is shown in microgravity onboard the ISS during installation by Thomas Pesquet (ESA).

4.2 Thermal results

From the first days of data that came in it is possible to conclude that we have remarkable thermal stability. The temperature of the laser stays between 49.6°C and 49.7°C throughout the day. The control board temperature remains between 42.2°C and 42.3°C. These temperatures are comparable with the temperatures on ground where we have convection to cool the QUBE. This is mainly because the ICF has forced airflow which mimics this effect. The results are considerably better than the worst-case scenario we tested in the lab.

4.3 The QUBE ODMR and sensitivity

To show that the device is capable of performing NV magnetometry onboard the ISS, the data of the on-ground testing and the data taken in orbit were compared. A single peak from the ODMR spectrum for both the ground data and the onboard data can be seen in Fig. 45b. The photoluminescence signal was normalised to 1, to compare the difference of each resonance amplitude and line width of the experiment before and after the launch event. The resonance measured on ground (in the laboratory) has a linewidth of 13.6 MHz and a contrast of 1.55 %, leading to sensitivity of a 7.94 nT/sqrt(Hz).

The same analysis was done for the resonance onboard the ISS, which gave a linewidth of 9.45 MHz, a contrast of 1.81 % and a resulting sensitivity of 3.33 nT/sqrt(Hz). This comparison shows that the sensitivity onboard the ISS has slightly increased compared to its performance on ground. This way we demonstrated the performance of the experiment was not affected by the mechanical stresses of the launch.

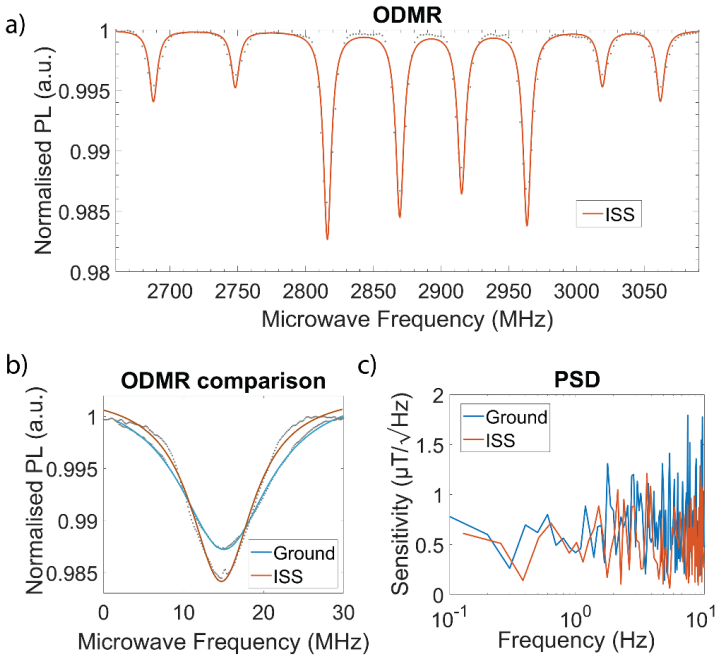

Fig. 44. a) ODMR peaks corresponding to 4 different NV axes measured with QUBE onboard the ISS b) Comparison of single peak on ground and onboard the ISS c) Power Spectral Density comparison

Besides the ODMR spectra, it is useful to compare the ground and onboard PSD data hinting the system sensitivity. This is shown in Fig. 44c where the sensitivity has insignificantly improved while in orbit. This could be due to the mechanical aspects of microgravity when the mechanical structure settles and is no longer subject to gravity or change in temperature can have a slight effect on the optical alignment, and lastly the mechanical stresses during the rocket launch.

4.4 Magnetic field mapping preliminary results

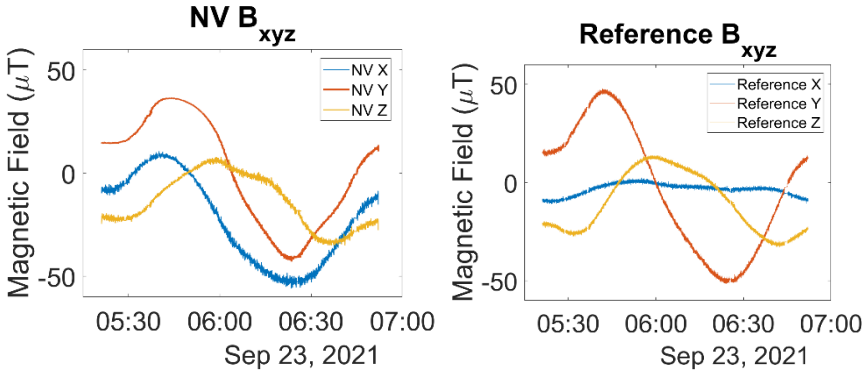

Fig. 45. Preliminary comparison of magnetic field measurements of 90 minutes. On the left measured with NV sensor, on the right measured with reference sensor

A comparison of the NV-magnetometer data and the reference magnetometer can be seen in Fig. 45. The NV-magnetometer shows more noise in comparison to the reference magnetometer, the detected amplitude of the signal is also slightly lower. Both magnetometer data follow the same profile, indicating that the change is indeed the magnetic field and not a result of other factors. The data is still preliminary and needs further investigation and processing. The X axis do not seem to match and the reason will be further studied.

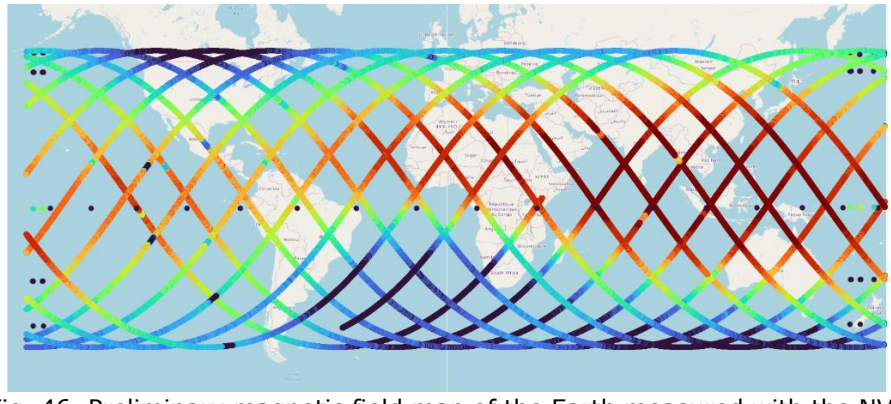

Fig. 46. Preliminary magnetic field map of the Earth measured with the NV sensor – vertical field. The map shows 24 hours of measurements.

The map shown in Fig**.** 46 is a preliminary visualization of magnetic field map of the Earth that is obtained using the ODMR magnetometry from our QUBE. The data was obtained over the course of 24 hours, which are typically up to 16 orbits around the Earth. This data is very preliminary and will be further improved by appending data collected over a longer period. This period will extend up to ten months. The distinction between the north and south is visible.

4.5 Preliminary results of advanced operation protocols

One of the novel ways to perform the diamond magnetometry is by using the PDMR technique. As this technique is relatively recent there are still challenges to overcome before its practical usability. However, we demonstrated in Fig. 47 the PDMR spectrum on the QUBE using sample #353, and thereby proven the device allows the usage of this readout technique. The results were severely limited in terms of sensitivity therefore in the flight model we opted for a sample optimized for optical (ODMR) performance.

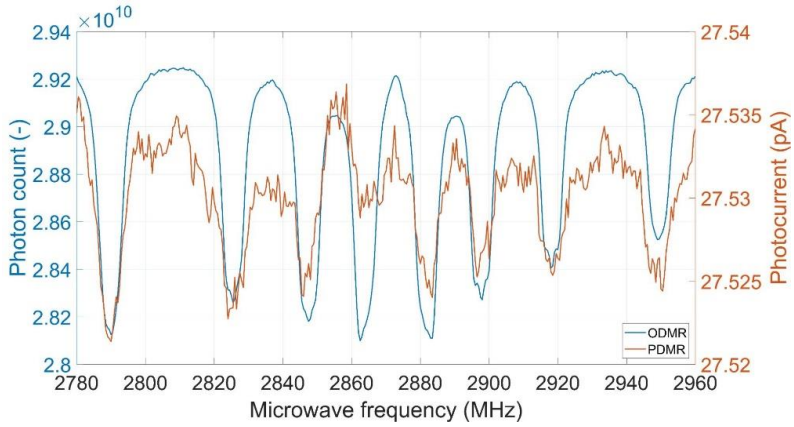

Fig. 47. PDMR spectrum at best conditions on the QUBE with sample #353.

Another novel technique the device is capable of is pulsed ODMR magnetometry. The FPGA pulse generator was successfully verified to generate suitable pulses with a minimal pulse width of 10ns and also the specialized readout circuitry for pulsed readout was verified to be working. However, this system needs further development and testing, as it was observed during on-ground performance tests, the detected signal suffers from capacitive effects that not only distort the shape but also prolong the detected pulse duration. This behaviour can be seen in Fig. 48.

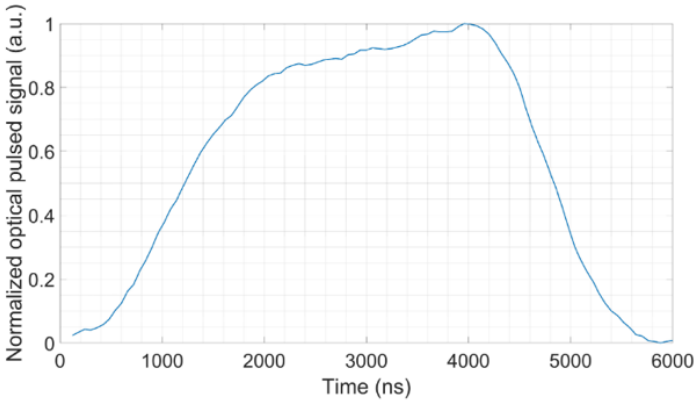

Fig. 48. The laser pulse of 5 µs observed by the pulsed readout system to benchmark the readout method.

Conclusions and Outlook

The OSCAR-QUBE is the first student-made diamond-based quantum magnetometer to be tested onboard the ISS. The device was designed, assembled, and tested within a year by the OSCAR-QUBE team within the framework of the 'Orbit Your Thesis!' programme. The device is operating autonomously onboard the ISS with manual control over the parameters and functional data acquisition using the UHB. The results have shown that after reaching the ISS the system is stable and no significant decrease in sensitivity or performance was observed. It is possible to measure magnetic fields with a dynamic range up to 1.86 mT. The device shot noise limited sensitivity is less than 5 nT/sqrt(Hz). The data from the device onboard the ISS that is continuously being sent to the UHB, is currently being processed.

The acquired data is then linked to the GPS coordinates enabling reconstruction of a magnetic field map of the Earth. The device can measure the magnetic field with a sampling frequency up to 1.3kHz.

After more than a year of designing, testing, building and good teamwork, our experiment cube has finally reached orbit. But the project does not stop here. The QUBE will remain onboard the ISS for ten months, continuously sending data to our UHB. We will be further mapping the Earth's magnetic field. When the mission is over, the instrument will return to our lab for further investigation after almost a year in microgravity. The development of the photo-electric readout and pulsed measurements to unlock the true quantum power will be pursued. Miniaturization of the system and a further optimization can lead to on-chip integration and widespread adoption of this technology. The OSCAR-QUBE team has taken a big step forward in the development of quantum-based magnetometers and will continue to push forward. So, let us work together and change the way magnetometry is done in space today!

Acknowledgements

We, as team OSCAR-QUBE, would like to thank European Space Agency and Space Application Services for giving us the opportunity to send our device into orbit aboard the ISS. We also want to thank the 'Orbit Your Thesis!' (OYT) programme organisers namely the project coordinator Nigel Savage for his guidance and support. And our ELGRA mentors Marco Braibanti and Sven Herrmann for their expertise. We would like to also thank to the research group of our endorsing professor Milos Nesladek, namely Emilie Bourgeois and Michal Gulka for their insights. Also, to Prof. Ronald Thoelen for his support. Furthermore, we would like to thank ESEC Galaxia for allowing us to conduct vibration testing of the device. Lastly, we thank Hasselt University and IMO-IMOMEC for their endless support and facilities they have provided us throughout our journey.

References

[1] C. L. Degen, F. Reinhard, and P. Cappellaro, 'Quantum sensing', Rev. Mod. Phys., vol. 89, no. 3, p. 035002, Jul. 2017, doi: 10.1103/RevModPhys.89.035002.

[2] T. Schönau et al., 'A three-axis SQUID-based absolute vector magnetometer', Review of Scientific Instruments, vol. 86, no. 10, p. 105002, Oct. 2015, doi: 10.1063/1.4933386.

[3] L. Rondin, J.-P. Tetienne, T. Hingant, J.-F. Roch, P. Maletinsky, and V. Jacques, 'Magnetometry with nitrogen-vacancy defects in diamond', Rep. Prog. Phys., vol. 77, no. 5, p. 056503, May 2014, doi: 10.1088/0034-4885/77/5/056503.

[4] J. F. Barry et al., 'Sensitivity optimization for NV-diamond magnetometry', Rev. Mod. Phys., vol. 92, no. 1, p. 015004, Mar. 2020, doi: 10.1103/RevModPhys.92.015004.

[5] 'Orbit Your Thesis'. https://www.esa.int/Education/Orbit_Your_Thesis (accessed Sep. 29, 2021).

[6] R. C. Snare, 'A history of vector magnetometry. Measurement Techniques in Space Plasmas.', American Geophysical Union, vol. 1998, pp. 101–114.

[7] H. Heidari and V. Nabaei, Magnetic Sensors for Biomedical Applications. John Wiley & Sons, 2019.

[8] W. Li and J. Wang, 'Magnetic Sensors for Navigation Applications: An Overview', The Journal of Navigation, vol. 67, no. 2, pp. 263–275, Mar. 2014, doi: 10.1017/S0373463313000544.

[9] P. V. Sharma, 'Magnetic method applied to mineral exploration', Ore Geology Reviews, vol. 2, no. 4, pp. 323–357, Aug. 1987, doi: 10.1016/0169-1368(87)90010-2.

[10] S. Foner, 'Versatile and Sensitive Vibrating-Sample Magnetometer', Review of Scientific Instruments, vol. 30, no. 7, pp. 548–557, Jul. 1959, doi: 10.1063/1.1716679.

[11] N. Olsen, G. Hulot, and T. J. Sabaka, 'Measuring the Earth's Magnetic Field from Space: Concepts of Past, Present and Future Missions', Space Sci Rev, vol. 155, no. 1, pp. 65–93, Aug. 2010, doi: 10.1007/s11214-010-9676-5.

[12] X. Jiang, G.-B. Bian, and Z. Tian, 'Removal of Artifacts from EEG Signals: A Review', Sensors, vol. 19, no. 5, Art. no. 5, Jan. 2019, doi: 10.3390/s19050987.

[13] Z. Chen, B. Liu, X. Yan, and H. Yang, 'An Improved Signal Processing Approach Based on Analysis Mode Decomposition and Empirical Mode Decomposition', Energies, vol. 12, no. 16, Art. no. 16, Jan. 2019, doi: 10.3390/en12163077.

[14] T. Wolf et al., 'Subpicotesla Diamond Magnetometry', Phys. Rev. X, vol. 5, no. 4, p. 041001, Oct. 2015, doi: 10.1103/PhysRevX.5.041001.

[15] P. R. W. Hudson and P. P. Phakey, 'Defects in natural type IB diamond', Nature, vol. 269, no. 5625, pp. 227–229, Sep. 1977, doi: 10.1038/269227a0.

[16] J. O. Orwa et al., 'Engineering of nitrogen-vacancy color centres in high purity diamond by ion implantation and annealing', Journal of Applied Physics, vol. 109, no. 8, p. 083530, Apr. 2011, doi: 10.1063/1.3573768.

[17] A. Haque and S. Sumaiya, 'An Overview on the Formation and Processing of Nitrogen-Vacancy Photonic Centres in Diamond by Ion Implantation', Journal of Manufacturing and Materials Processing, vol. 1, no. 1, Art. no. 1, Sep. 2017, doi: 10.3390/jmmp1010006.

[18] G. Davies, M. F. Hamer, and W. C. Price, 'Optical studies of the 1.945 eV vibronic band in diamond', Proceedings of the Royal Society of London. A. Mathematical and Physical Sciences, vol. 348, no. 1653, pp. 285–298, Feb. 1976, doi: 10.1098/rspa.1976.0039.

[19] E. V. Levine et al., 'Principles and techniques of the quantum diamond microscope', Nanophotonics, vol. 8, no. 11, pp. 1945–1973, Nov. 2019, doi: 10.1515/nanoph-2019-0209.

[20] M. W. Doherty, N. B. Manson, P. Delaney, F. Jelezko, J. Wrachtrup, and L. C. L. Hollenberg, 'The nitrogen-vacancy colour centre in diamond', Physics Reports, vol. 528, no. 1, pp. 1–45, Jul. 2013, doi: 10.1016/j.physrep.2013.02.001.

[21] M. Chipaux et al., 'Nitrogen vacancies (NV) centres in diamond for magnetic sensors and quantum sensing', in Quantum Sensing and Nanophotonic Devices XII, Feb. 2015, vol. 9370, pp. 400–405. doi: 10.1117/12.2084082.

[22] E. Bourgeois et al., 'Photoelectric detection of electron spin resonance of nitrogen-vacancy centres in diamond', Nat Commun, vol. 6, no. 1, p. 8577, Oct. 2015, doi: 10.1038/ncomms9577.

[23] E. Bourgeois, M. Gulka, and M. Nesladek, 'Photoelectric Detection and Quantum Readout of Nitrogen-Vacancy Centre Spin States in Diamond', Advanced Optical Materials, vol. 8, no. 12, p. 1902132, 2020, doi: 10.1002/adom.201902132.

[24] K. Jensen, V. M. Acosta, A. Jarmola, and D. Budker, 'Light narrowing of magnetic resonances in ensembles of nitrogen-vacancy centres in diamond',

Phys. Rev. B, vol. 87, no. 1, p. 014115, Jan. 2013, doi: 10.1103/PhysRevB.87.014115.

[25] D. J. Griffiths and D. F. Schroeter, Introduction to Quantum Mechanics. Cambridge University Press, 2018.

[26] S. Hong et al., 'Nanoscale magnetometry with NV centres in diamond', MRS Bulletin, vol. 38, no. 2, pp. 155–161, Feb. 2013, doi: 10.1557/mrs.2013.23.

[27] USDOD, 'Military Standard Measurement of Electromagnetic Interference'.

8. Chapter 8 – Conclusion and outlook

8.1. Conclusion

The following chapter summarizes the main results of the PhD work. The first and second chapter cover the theoretical background necessary for understanding of the underlying physics principles presented in this thesis. It focuses mainly on the NV centre structure and principles as well as its energy level structure and description of the measurement methods such as ODMR and PDMR, with focus on magnetometry. This chapter also introduces more advanced measurement protocols such as pulsed measurements schemes and GSLAC based microwave-free magnetometry. Description of optical and e-beam lithography process used in sample fabrication within this thesis can be also found in this section.

The third chapter outlines the experimental methods used within this work. It describes in detail the practical steps needed for successful lithography on small diamond samples. It also describes the measurement setup concept, layout, and high-level overview of its key components. It also highlights differences of all four different setups developed in the course of this thesis. The chapter also describes the main software components needed for the setup automation. The following chapters discuss published experimental results.

Chapter four is based on a paper about Pulsed Photoelectric Coherent Manipulation and Detection of N-V Centre Spins in Diamond, which is demonstrated on small ensembles of (down to 5) NV centres. In this paper Rabi and Ramsey coherent spin manipulation and photoelectric readout protocols are discussed using encoding high-frequency MW and laser-pulse sequences into a low-frequency envelope. By using the PDMR technique for readout of NV spins and employing the lock-in readout technique, we reach a signal detection contrast close to 100%. A significant reduction of the noise compared to the CW technique makes possible an order of magnitude enhancement of the SNR and thus sensitivity of magnetic field sensing. The work is built upon the patent US20170328965A1 on lock-in use for microwave triggered operations.

Fifth Chapter covers the PDMR based magnetic field measurements and discusses the detection sensitivity as a function of the laser excitation wavelengths. It was demonstrated that the laser light excitation colour influences the magnetic field sensitivity of the PDMR method, while keeping the key parameters (i.e., laser power, microwave power) in a low power range. The PDMR performances obtained using a yellow-green (561 nm) laser surpass the performances of the green laser (532 nm) PDMR. The conclusion is that the lower photon energy illumination enables to achieve better signal to background ratio by suppressing the photoionization of defects other than NV centres (i.e., P1 centres). In this work the photoelectric readout leads to ten times improved sensitivity to magnetic fields in the selected conditions, in comparison to the optical detection method.

Sixth Chapter covers a novel microwave-free detection based upon the photoelectric readout technique and cross relaxation processes of NV centre spins in bulk diamond. In this paper a microwave-free magnetometry based on the Ground Spin Level Anti-Crossing (GSLAC) is demonstrated and provides an alternative to conventional NV-MW based magnetometers for situation where it is difficult to apply MW fields.

In the last chapter - chapter seven, all the acquired fundamental knowledge on diamond-based magnetometry was used to construct an integrated magnetometer device. The device has been built by a team of students within the project OSCAR-QUBE (Optical Sensors based on CARbon materials: Quantum Belgium) in framework of the 'Orbit Your Thesis!' programme of the European Space Agency (ESA). The OSCAR-QUBE represents a first ever diamond-based quantum magnetometer that was tested in space. The device is operating autonomously aboard the International Space Station (ISS) and allows a remote control over the detection parameters as well as data acquisition using a User Home Base. The measured results have shown that after reaching the ISS the system is stable and no significant decrease in sensitivity or performance is observed. Furthermore, the device was able to map the magnetic field of the Earth on the Low Earth Orbit which, after analysis, is matching the International Geomagnetic Reference Frame (IGRF) model. The shot-noise limited sensitivity of the integrated device is < 5 nT/sqrt(Hz), however measured sensitivity is <200 nT/sqrt(Hz), with dynamic range up to 1.8 mT, which allows to map the Earth's magnetic field in 3d within range of approximately +-50 μT.

The application potential of the NV based magnetic field sensing technology is enormous as the magnetic field sensing has been one of the most important pillars of modern-day science. It has significance in research, near Earth geometrics (Earth shape), geology and archaeology, also in oil, gas, and minerals exploration. The consumer electronics devices have transformed the human life to a greater extent, and space exploration. Over the past years, the magnetometers market has a growing trend due to the increasing number of applications in the future.

8.2. Outlook

During my PhD research, in addition to published works, on basis of the measurements that I carried out I could pinpoint main design adaptations that would lead to higher sensitivity, reliability, and a further level of integration. Moreover, by improving the magnetometer performances we can compare our device to classical magnetometers on the market in terms of cost/performance benefits and bring to radar new applications for which the system can be in future commercialized, for example for a follow up project or directly via a start-up. To this end we identified several improvements to be made:

1. Engineering level as concerns of controls, driving, detectors as well as mechanical design
2. Replacing the discrete components with custom-build ICs.
3. Sensing protocol levels that will allow us to boost the sensitivity from the current device from > 100 nT/sqrt Hz to pT/sqrt Hz (pulsed protocols, hyperfine driving, radiometry combining and correlating two and more sensors, using double electron-electron resonance protocols)
4. Diamond material level to increase the spin contrast and the spin coherence time, optimizing the number of NVs

All these tasks that we will execute will lead to higher sensitivity but also higher integration level and the prospect for wider applications. To my gratification I have received 'Frank De Winne postdoc mandate' - an innovation mandate aimed specifically at innovative applications in the space sector - entitled " Diamond based quantum magnetic field sensors for space applications". During this 2 years period I will be able to address some of these topics.

As already mentioned previously, this mandate is closely linked to the space sector thanks to the recent developments achieved with diamond-based magnetometry technology during student project series OSCAR. As a team leader of this project, it is my personal vision to inspire and motivate students towards research and space sector. So far, we were able to pursue those goals rather successfully [60] and we will continue to do so also in the future. As a follow-up on the OSCAR-QUBE project, we are currently developing next iteration of our magnetic field sensing device that will fly onboard the Ariane 6 ‘maiden flight’ as part of the YPSAT experiment developed by ESA Young Graduate Trainees (YGTs). [61] We are pursuing this opportunity together as students from Hasselt University in collaboration with ESA YGTs with vision to inspire next generations of students and young professionals to dream big and to work together towards strengthening the European space sector.

9. Appendix

9.1. Setup component description

9.1.1. Setup 2 (Magnetometry setup)

The Setup 2 is most often used for magnetometry measurements and is equipped with magnet holder for the purpose of Zeeman splitting. The S2 also has automated control of laser intensity by robotic polarizing wheel and servo-controlled detector.

Table 7 List of equipment currently present on setup 2 (by 02/02/2021)

Function	Part/device	Model	Company	Description
Optical excitation	Green laser	Gem	Laser Quantum	CW solid-state laser, 532 nm emission wavelength, 500 mW maximal power, power stability < 1 % RMS, M^2 < 1.2, beam diameter 1 mm, horizontal polarization
	Red laser	IBEAM-SMART-PT-660	Toptica	Pigtailed Diode Laser, ·Wavelength: 660 ± 3 nm, Output power: 75 mW (exit fiber), RMS noise: < 0.25 % (10 Hz - 10 MHz), M^2 < 1.1,

				Modulation bandwidth up to 250MHz, Rise and fall times < 1.5 ns
Pulsing of green laser	Acousto-optic modulator (AOM)	AOMO 3200-146	Crystal Technology	20 ns rise time, 31 MHz modulation bandwidth, 1000:1 contrast ratio, 80 % diffraction efficiency
	RF source	AODR 1200AF-DIF0-1.0	Crystal Technology	Digital modulation, 200 MHz frequency, 1 W output power
Combination of green and red laser beams	Dichroic mirror (Better quality dichroic has been ordered from Semrock)	#69-890	Edmund Optics	600nm, 25mm Diameter, Dichroic Longpass Filter
Separation of PL light from laser excitation	Dichroic mirror (Better quality dichroic has been ordered from Semrock)	FF677-Di01-25x36	Semrock	677 nm edge BrightLine® single-edge standard epi-fluorescence dichroic beamsplitter
Focusing of laser light on sample (objectives shared	Oil objective	PlanApo N	Olympus	60X, NA = 1.42, W.D = 170 µm

with other confocal set-ups)	Water objective	UplanSApo	Olympus	60X, NA = 1.2, W.D = 130 to 210 µm
	Air short-distance objective	UPlanSApo	Olympus	40X, N.A. = 0.95, W.D = 110 to 230 µm
	Air long-distance objective	M Plan Semi-Apochromat	Olympus	100X, N.A. = 0.8, WD = 3.4 mm
Sample x-y-z movement	Manual xyz translation stage	MT3/M	Thorlabs	12.7 mm XYZ Translation Stage with Standard Micrometers
Objective movement	Piezoelectric xyz stage	LT3.200	PIEZOCONCEPT	Range of motion : 200 x 200 x 100µm Resolution : 0,2nm
	Piezo state controller	Controller3a	PIEZOCONCEPT	analogue controller for 3 axis stage
	Analog voltage generation for control of piezo state movement	USB-6008	NI	8 AI (12-Bit, 10 kS/s), 2 AO (150 Hz), 12 DIO USB Multifunction I/O Device
Photoluminescence detection	Pinhole	P30S	Thorlabs	Ø1" Mounted Precision Pinhole, 30 ± 2 µm Pinhole Diameter
	Spectral filter to block laser	ET665lp	Chroma	OD = 6

	light			
	Spectral filter to select NV-PL	FELH0650	Thorlabs	OD > 5
	Spectral filter for measurements with red excitation	FELH0700	Thorlabs	OD > 5
	Single photon counter	SPCM-AQRH-14	Excelitas Technologies	Dark counts < 100 cts/s, dead time: 20 ns, Output count rate before saturation: 40 MCts/s
Photoelectric detection	Voltage source and Picoammeter	487	Keithley	± 500V source, 10fA sensitivity
	Current-to-voltage preamplifier	SR570	Standford Research Systems	5 fA/√Hz input noise, 1 MHz maximum bandwidth (at low amplification), 1 pA/V maximum gain, configurable signal filters
	Lock-in amplifier	7270 DSP lock-in amplifier	Signal recovery	1 mHz - 250 kHz frequency range 2 nV/2 fA - 1 V/1 µA FS sensitivity Main ADC and analog

				outputs update rate of 1 MSa/s
MW signal generation, amplification and pulsing	MW source	SG384	SRS	DC to 4 GHz, 1 µHz resolution AM, FM, ØM, PM and sweeps (N-type output). -116 dBc/Hz phase noise (20 kHz offset, f=1 GHz).
	MW amplifier	ZHL-16W-43-S+	Mini-Circuits	16 Watt max. ouput power, 45 dB gain, 800 to 4200 MHz range, gain flatness ±1.5 dB
	MW switch	ZASWA-2-50DR+	Mini-Circuits	DC to 5 GHz, Rise/fall time ~ 5 ns
Pulse sequences generation	TTL signal generator	BNC Model 588	Fast Comtec	8 Channel Model, 250 ps Resolution, 50 pS RMS Jitter
	Sequences generation	Labview software	Home-built (J. Hruby)	
External magnetic field	Permanent magnet on magnet holder		Home-built	3-axes translation movement, 2 goniometers

9.1.2. Setup 3 (NMR setup)

The Setup 3 is equipped with the Time-tagger (time event to digital converter, Swabian Instruments) and the Pulse streamer (8-channel TTL pulse generator, Swabian Instruments) devices and was designed mainly to perform NMR on single NV. The system is equipped with series of microwave switches enabling the complex MW + RF sequences necessary for NMR operation.

Table 8 List of equipment currently present on setup 3 (by 02/02/2021)

Function	Part/device	Model	Company	Description
Optical excitation	Yellow laser	Gem 561	Laser Quantum	CW solid-state laser, 561 nm emission wavelength, 75 mW maximal power, power stability < 1 % RMS, M^2 < 1.2, beam diameter 1 mm, horizontal polarization
	Green laser	IBEAM-SMART-PT-515	Toptica	Pigtailed Diode Laser, 512 nm emission wavelength, 50 mW maximal power, RMS noise: < 0.25 % (10 Hz - 10 MHz), M^2 < 1.1, Modulation bandwidth up to 250MHz,

				Rise and fall times < 1.5 ns
Pulsing of yellow laser	Acousto-optic modulator (AOM)	AOMO 3200-146	Crystal Technology	20 ns rise time, 31 MHz modulation bandwidth, 1000:1 contrast ratio, 80 % diffraction efficiency
	RF source	AODR 1200AF-DIF0-1.0	Crystal Technology	Digital modulation, 200 MHz frequency, 1 W output power
Combination of green and yellow laser beams	Dichroic mirror	FF538-FDi01-25x36	Semrock	538 nm edge BrightLine® single-edge image-splitting dichroic beamsplitter for standard microscopy. Nominal Radium of Curvature ~ 100 m, Maximum Reflected Beam Diameter = 10 mm, Reflected Wavefront Error < 2λ
Separation of PL light from laser excitation	Dichroic mirror	FF580-FDi01-25x36	Semrock	580 nm edge BrightLine® single-edge

				image-splitting dichroic beamsplitter for standard microscopy. Nominal Radium of Curvature ~ 100 m, Maximum Reflected Beam Diameter = 10 mm, Reflected Wavefront Error < 2λ
Focusing of laser light on sample (objectives shared with other confocal set-ups)	Oil objective	PlanApo N	Olympus	60X, NA = 1.42, W.D = 170 µm
	Water objective	UplanSApo	Olympus	60X, NA = 1.2, W.D = 130 to 210 µm
	Air short-distance objective	UPlanSApo	Olympus	40X, N.A. = 0.95, W.D = 110 to 230 µm
	Air long-distance objective	M Plan Semi-Apochromat	Olympus	100X, N.A. = 0.8, WD = 3.4 mm
Objective vertical movement	Manual z-translation stage	MVS010/M	Thorlabs	25mm Vertical Translation Stage
Sample movement	Manual xy stage	M-545	PI	Manual XY Microscope Stage
	Piezoelectric	P-545.3C8S	PI	XYZ Piezo

	xyz stage			System, Clear Aperture for Microscope Slides, 200 µm × 200 µm × 200 µm, Capacitive Sensors
	Piezo state controller	E-727.3CDA	PI	Digital Multi-Channel Piezo Controller, 3 Channels, -30 to 130 V, Sub-D Connector(s), Capacitive Sensors, Analog Inputs
Photoluminescence detection	Pinhole	P30S	Thorlabs	Ø1" Mounted Precision Pinhole, 30 ± 2 µm Pinhole Diameter
	Spectral filter to block laser light	ET570lp	Chroma	OD = 6
	Spectral filter to select NV-PL (other filters can be mounted if required)	FELH0650	Thorlabs	OD > 5
	Single photon counter	SPCM-AQRH-14	Excelitas Technologies	Dark counts < 100 cts/s, dead time: 20 ns, Output count rate before saturation: 40 MCts/s

	PL detection gating for time-resolved measurements	Time Tagger 20	Swabian Instruments	34 ps RMS Jitter, 8.5 M tags/s transfer rate, 8 input channels
Photoelectric detection	Voltage source and Picoammeter	487	Keithley	± 500V source, 10fA sensitivity
	Current-to-voltage preamplifier	SR570	Standford Research Systems	5 fA/√Hz input noise, 1 MHz maximum bandwidth (at low amplification), 1 pA/V maximum gain, configurable signal filters
	Lock-in amplifier	SR850	Standford Research Systems	1 mHz to 102.4 kHz range, >100 dB dynamic reserve, 0.01 degree phase resolution, Time constants from 10 µs to 3 ks
MW signal generation, amplification and pulsing	MW source	SynthNV Signal Generator	Windfreak	34.4MHz – 4.4GHz RF Signal Generator plus RF Power Detector, +19

				dBm output power, ½ dB amplitude output power step size
	MW amplifier	ZHL-42+	Mini-Circuits	600 to 4200 MHz, gain: 38 dB, gain flatness: ±0.8 dB
	MW switch	ZASWA-2-50DR+	Mini-Circuits	DC to 5 GHz, Rise/fall time ~ 5 ns
RF signal generation, amplification and pulsing	RF source	STEMLAB 125-10	Red Pitaya	
	RF amplifier	ZX60-100VH+	Mini-Circuits	0.3 to 100 MHz, gain: 30 dB
	RF switch	ZASWA-2-50DR+	Mini-Circuits	DC to 5 GHz, Rise/fall time ~ 5 ns
MW and RF signal multiplexing	Diplexer	Diplexer	Home-built (University of Vienna)	
Pulse sequences generation	TTL signal generator	Pulse Streamer 8/2	Swabian Instruments	8 digital and 2 analog output channels, 1 GSa/s digital sampling rate, 125 MSa/s analog sampling rate, 1 M pulses pattern memory
	Sequences generation	Labview software	Home-built (J. Hruby, J. Vodnik)	

9.1.3. Setup 4 (OSCAR-QUBE test bench setup)

The Setup 4 is a specialized setup designed as test bench model for the project OSCAR-QUBE. The system is designed as "low-budget" simplification of measurement system. Compared to the rest, this system is not a confocal system and does not have piezo controlled stage, instead has XYZ stepper motor stage.

Table 9 List of equipment currently present on setup 4 (by 02/02/2021)

Function	Part/device	Model	Company	Description
Optical excitation	Green laser	L520P50	OSCAR-QUBE	CW Laser diode, 520 nm emission wavelength, 50 mW maximal power
Pulsing	none	none	none	none
Separation of PL light from laser excitation	Dichroic mirror	DMLP550L	Thorlabs	Ø2" Longpass Dichroic Mirror, 550 nm Cut-On
Focusing of laser light on sample	Focusing lens	APL0303	Thorlabs	NA = 0.59, W.D = 1 mm
Sample movement	Electric xy stage for coarse movement	M-126.DG1 with C-663.12	PI	Electric XY Microscope Stage and controller
Photoluminescence detection	Long-pass Spectral filter to block laser light	FELH0550	Thorlabs	OD > 5
	Long-pass Spectral filter to select NV-PL	FELH0650	Thorlabs	OD > 5
	Photodiode detector with integrated lens	S5973-1	OSCAR-QUBE	Photodiode and DAC board
Photoelectric detection	Voltage source		OSCAR-QUBE	0-30V

	Current-to-voltage preamplifier		OSCAR-QUBE	Preamplifier with DAC on PCB
	Current-to-voltage preamplifier	DLPCA-200	Femto	440 fA/√Hz input noise at 400kHz and 100 nA/V
MW signal generation, amplification and pulsing	MW source		OSCAR-QUBE	1800MHz – 4000MHz, +26 dBm output power with 32dB programable attenuator
	MW amplifier	ZHL-16W-43-S+	Mini-Circuits	1800 to 4000 MHz, gain: 45 dB, gain flatness: ±2.0 dB